Development of Active and Stable Nanostructured Ceria-based Catalysts for Soot Oxidation

by

Boyu Li

A thesis
presented to the University of Waterloo
in fulfillment of the
thesis requirement for the degree of
Doctor of Philosophy
in
Chemical Engineering

Waterloo, Ontario, Canada, 2019

Examining Committee Membership

The following served on the Examining Committee for this thesis. The decision of the Examining Committee is by majority vote.

External Examiner	Dr. Hui Wang Professor
Supervisor(s)	Dr. John Z. Wen Associate Professor
Supervisor(s)	Dr. Eric Croiset Professor
Internal Member	Dr. William A. Anderson Professor
Internal Member	Dr. Zhongchao Tan Professor
Internal Member	Dr. Michael Pope Assistant Professor

Author's Declaration

This thesis consists of material all of which I authored or co-authored: see Statement of Contributions included in the thesis. This is a true copy of the thesis, including any required final revisions, as accepted by my examiners.

I understand that my thesis may be made electronically available to the public.

Statement of Contributions

One chapter in this thesis is based on published work co-authored by myself. This includes the following publication.

Chapter 4 of this thesis consists of a paper that was co-authored by myself, my supervisors, Anton D. Sediako, Dr. Pei Zhao, Dr. Jingde Li, Dr. Murray J. Thomson. I carried out most of the experiments, collected and analyzed the data, as well as written most parts of the manuscript.

Li, B., Sediako, A. D., Zhao, P., Li, J., Croiset, E., Thomson, M. J., & Wen, J. Z. (2019). Real-time observation of Carbon oxidation by Driven Motion of Catalytic Ceria Nanoparticles within Low pressure oxygen. Scientific reports, 9(1), 8082.

Abstract

The focus of this thesis is to improve catalytic activity and stability of ceria-based catalysts for soot oxidation. The main objective was to develop an inexpensive, active and stable catalyst through iron and samarium doping. The role of iron and samarium doping towards improving catalytic activity and stability was elucidated through nano (in-situ Environmental Transmission Electron Microscope - ETEM) and bulk (Thermogravimetric Analysis - TGA) scales investigations, along with a suite of characterization techniques.

Fe-doped ceria catalytic soot oxidation was investigated by observing in-situ catalytic oxidation using ETEM. Both catalyst and carbon particles can be mobile. The relative mobility of these particles appears to be correlated to the size of particles. A semi-quantitative analysis was carried out to quantify the mobility of the particles and relate it to the catalyst activity. It was found out that reaction rates were calculated and found to be positively correlated to the contact length between carbon and catalyst particles, thus indicating that the catalytic carbon oxidation occurs at the carbon/catalyst interface. Larger normalized reaction rates lead to higher movement velocity, suggesting that the mobility is caused by carbon oxidation on the catalyst's surface.

In order to improve the activity of the ceria-based catalysts for soot oxidation, different amounts of Fe doping were incorporated into CeO_2. The catalysts were prepared using two different methods, co-precipitation (CP) and solution combustion synthesis (SCS), leading to different morphologies. It was confirmed by X-ray Diffraction (XRD) that iron was incorporated in the cerium oxide lattice, which formed a solid solution. For both fabrication methods, there is an optimum Fe content that gives the highest activity. For SCS catalyst, the optimum Fe content is 5%, and for CP catalyst, it is 10%. Irrespective of the fabrication method, the most important

parameter that dictates the reaction activity (e.g. T50) is the Ce^{3+} content, which is closely related to the content of oxygen vacancies. The activity increases notably when Ce^{3+} content increases up to 20%. Above 20% Ce^{3+} content, the activity increases moderately.

It is well known that pure ceria possesses poor stability performance (deactivation) and thus, inspired by the work on solid oxide fuel cell (SOFC), samarium (Sm) doped ceria was considered as a promising candidate for stable ceria-based catalysts for soot oxidation, because Sm can help form stable fluorite crystal structure. It was found that samarium doping indeed improves the stability of ceria-based catalyst for soot oxidation. In particular, at higher Sm content (10% and 20%), the reactivity (represented by T50 - temperature at 50% conversion of soot) nearly plateaus after 5 cycles. However, increasing Sm content decreases activity for soot oxidation. The 10% Sm-doped catalyst showed the best compromise between stability and activity. It was found that Ce^{3+} and O_α (surface oxygen species) played the most important role in controlling catalytic soot oxidation activity, because they are directly related to oxygen vacancies and oxygen storage capacity of the catalyst. Sm-doping catalysts, especially at 10% and 20% Sm, show minimum decrease in Ce^{3+} content and O_α percentage between fresh and spent catalysts after 5 cycles. Crystal size growth over several cycles was not found as the most important parameter for catalyst deactivation, unlike in most studies that looked at catalyst activity from accelerated thermal aging point of view. Finally, although addition of Fe on 20% Sm doped ceria catalyst did improve the activity in early cycles, but showed poor stability, which was unexpected.

In summary, a series of active and stable catalysts were synthesized and analyzed in this thesis. The in-situ ETEM observation shows that catalysts and carbon particles are mobile during soot oxidation and this mobility is initialized by the oxidation happened at catalyst-carbon surface.

There is an optimum Fe content that gives the highest activity for CP (10%) and SCS (5%) catalysts towards soot oxidation. The most important parameter that dictates the reaction activity is the Ce^{3+} content. Sm-doped ceria catalysts improved stability of ceria-based catalyst for soot oxidation and the activity of higher Sm doped catalyst (10% and 20%) nearly plateaus after 5 cycles, with minimum decrease of Ce^{3+} and O_{α} content between fresh and spent catalysts. The 10% Sm-doped catalyst shows the best compromise between stability and activity.

Acknowledgements

First, I would like to sincerely thank my supervisors Dr. John Z. Wen and Dr. Eric Croiset for their motivation and support. I am grateful for their encouragement to help me overcome the difficulties in my graduate study and their guidance to help me grow into a capable researcher.

Next, I would like to appreciate my committee members Dr. Hui Wang from University of Saskatchewan, Dr. William Anderson, Dr. Zhongchao Tan, Dr. Michael Pope and Dr. David Simakov from University of Waterloo for their perceptive suggestions and comments.

I would like to acknowledge all my group members who always share their thoughts and research experience with me. We work together as a great cooperative team. And I would like to express my gratitude to the staff in our department for all the help and technical support.

I would also like to express my gratitude and love to my family. Your love, trust and support have always encouraged me and helped me throughout the PhD life.

Finally, I acknowledge the finical support from the Natural Science and Engineering Research Council of Canada (NSERC) and University of Waterloo.

Table of Contents

List of Figures

List of Tables

List of Abbreviations

BE – Binding energy

BET – Brunauer-Emmett-Teller

BF – Bright field

CAEM – Atmosphere electron microscope

CP – Co-precipitation

DFT – Density Functional Theory

DPF – Diesel particulate filter

DPF-CC – DPF enhanced with a catalyst coating

DPF_FBC – Fuel borne catalysts

E_{coh} – The cohesive energies

EDS – Energy dispersive X-ray spectroscopy

ETEM – Environmental Transmission electron microscopy

FE-SEM – Field-emission scanning electron microscope

GDC – Gadolinium doped ceria

H_2-TPR – H_2-Temprature programmed reduction

I – Intensity

MEMS – Microelectrical mechanical system

NO_x – Nitrogen oxides

OSC – Oxygen storage capability

O_α – Surface oxygen species

O_β – Lattice oxygen

O_2^{2-} – Peroxide

O_2^- – Superoxide

PM – Particulate matters

PM10 – Particulate matter smaller than 10 μm

SCS – Solution combustion synthesis

SDC – Samarium doped ceria

SEM – Scanning electron microscopy

SOFC – Solid oxide fuel cell

SOEC – Solid oxide electrolysis

STEM – Scanning transmission electron microscopy

TEM – Transmission electron microscopy

TGA – Thermogravimetric Analysis

TPO – Temperature programmed oxidation

T10 – Ignition temperature

T50 – Combustion temperature

UV-VIS – Ultraviolet–visible spectroscopy

XPS – X-ray photoelectron spectroscopy

XRD – X-ray diffraction

3DOM – Three dimensionally ordered macroporous

Chapter 1: Introduction

Particulate matters (PM) are undesirable aerosol pollutants formed in industrial and automotive engines run on liquid fuels [1, 2]. Soot (a mass of impure carbon particles), as one type of PM, is formed in fossil fuel power plants, refineries, and internal combustion engines [3]. These fine carbonaceous particles, when released into the atmosphere, have been shown to be carcinogenic and directly linked to an increase in mortality rates [4, 5]. Therefore, there is an urgent need to develop novel materials for capturing and reducing particulate emissions from a wide range of combustion sources. These emissions can be controlled through processing exhaust gases by oxidizing the soot (carbon particles) to CO_2, as shown in Equation (1-1).

$$C + O_2 \rightarrow CO_2 \qquad \Delta H = -393.5 \text{ kJ} \quad [6] \qquad (1\text{-}1)$$

For many sources, the most common and effective method of mitigating carbon PM emission is the capture and then burning of particulates using a filter. Advanced materials have been sought for developing high-efficiency filters, especially for these particulates with size below 10 nm. For internal combustion engines, a diesel particulate filter (DPF) is usually installed in the exhaust system of a diesel engine, to deposit and oxidize fine carbon particles [7-14]. When the DPF is saturated with the deposited particulates, it must be regenerated or replaced, to avoid increasing the back-pressure of the engine which affects the vehicle operation [15, 16]. The temperature of unaided soot combustion is above 600°C [17], but the temperature of exhaust gas is only around 200-500°C [9, 10, 13]. In order to reduce the cost of adding extra fuel to burn out the deposited particulates, a catalyst can effectively reduce the oxidation temperatures of carbon PM to 200-400°C which is close to the temperature of engine exhaust gases [18]. It becomes important to find

catalysts, which are effective but less expensive than noble metals, to more effectively oxidize soot particles and extend the required regeneration time.

Significant efforts have been made to find a way to "regenerate" the DPF at lower temperatures using catalytic coatings. Among them, ceria (CeO_2) has shown high potential to lower DPF regeneration temperatures to 200-400°C – well within regular exhaust gas temperatures [19-21]. Ceria also presents some advantages compared to other DPF catalysts such as Pt, as it is naturally abundant, relatively inexpensive, less sensitive to sulfur impurities which poison other catalysts, and less environmentally toxic during recycling [22-25]. Ceria is frequently combined with a metal doping in an attempt to further increase its activity and durability [23, 26-28]. Transition metal doping has been reported to promote ceria assisted catalytic soot oxidation and produce more active sites over the surface [29-32]. Iron, in particular, is prominent because it can enhance the activity of CeO_2 due to its good redox ability - the oxygen species can alternate between Fe^{3+} and Fe^{2+} [5, 22, 33-35]. The mechanism of iron doped ceria catalysts has been investigated by Zhang et al. [29], highlighting the important role played by the redox cycle of iron in this reaction. Fe^{3+}, bonded with active oxygen, can be generated during doping and oxidize soot through its reduction to Fe^{2+}. This can also be reversed by oxidation of Fe^{2+} to Fe^{3+} with the interaction of Ce [22, 29]. The number of active Fe-O-Ce sites is reduced with less iron doping, while with more iron doping, the fluorite lattice can be distorted, which leads to a decrease in the number of oxygen vacancies, leading to lowered catalytic activity. Thus, the ratio of iron doping in ceria affects its catalytic activity and should be optimized under the reaction conditions.

Figure 1.1 describes the schematic of soot oxidation through ceria-based catalyst. The absorbed gaseous oxygen in catalysts is temporarily stored as lattice oxygen, which is, thereafter, delivered as a reactive species to oxidize soot at the soot-catalyst contact interface.

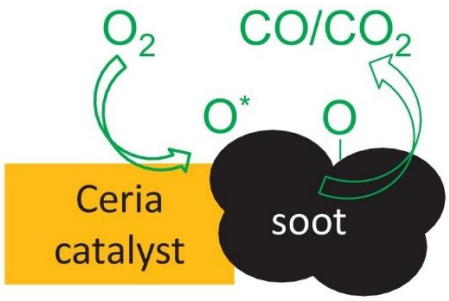

Figure 1.1. Schematic of soot oxidation through ceria based catalyst [8]

As a matter of fact, apart from the availability of active sites at the catalyst surface, the number of soot-catalyst contact points also contributes to the overall soot oxidation rate [36]. It is well-known that when soot is mixed with a catalyst in tight contact condition, the oxidation rate is much higher than when soot and the same catalyst are mixed in loose contact condition [13, 22, 37]. The increased number of contact points in tight conditions is responsible for this higher activity. However, under practical conditions occurring in a catalytic DPF, loose contact rather than tight contact is encountered [38]. In fact, good contact conditions are very difficult to be reached due to the different orders of magnitude in the soot particle and the catalyst cluster sizes, which clearly hinders the overall activity of the catalyst. It is, therefore, necessary to improve the soot-catalyst interactions, which can be achieved by tailoring the morphology of catalyst to maximize the number of contact points.

In order to directly observe the catalytic soot oxidation, in-situ microscopy studies can be carried out, with the use of environmental transmission electron microscopy (ETEM). In-situ ETEM

allows the observation of particle morphology, shape changes, motions and contact condition in a controlled temperature and oxygen partial pressure, and thus reveal the interactions between carbon and catalysts particles.

In addition, ceria-based catalyst has poor stability, as it is easy to sinter at high temperature, which is a major issue for their wide applications on DPF. For transition metals doped ceria catalysts, they generally exhibit low thermal stability due to the phase separation and dramatic reduction of surface area at high temperature [39-42]. In order to increase the durability of ceria based catalysts, researchers have attempted to modify CeO_2 based catalysts with metals such as Sm, Ba and Al etc., which can help the formation of thermally stable ceria-based solid solutions and inhibits crystal growth [43-46]. As a consequence, the stability of ceria-based catalyst for soot oxidation can be increased by incorporation of metals mentioned above.

1.1. Research gap

It is clear that the ceria based catalysts are promising catalysts for catalytic soot oxidation and application of DPF. However, challenges need to be addressed towards the synthesis of multicomponent catalysts based, on the one hand, on a combination of metal oxide, and, on the other hand, the modification of the structural parameters via the design of advanced nanoshape-catalyst. In addition, the poor stability of ceria-based catalyst remains the major obstacle for its application on DPF. When facing these challenges, this thesis has been devoted to develop effective and stable nanostructured multicomponent catalysts.

1.2.Research objectives

The research objective of this thesis is to develop a ceria-based catalyst for soot oxidation in DPF with the following characteristics:

1) Inexpensive and with good activity: thus, addition of iron for increased activity

2) Stable over many regeneration cycles: thus, use of more stable form of cerium oxide, such as samarium doped ceria

3) Fundamental study on interactions between catalyst and soot particles within catalytic soot oxidation

1.3. Research contribution

This research developed new effective and stable nanostructured ceria-based catalysts with tailored morphology for soot oxidation. Their activities at both nano- and bulk-scales, along with the effect of key parameters, such as temperature and gas composition, were investigated. The stability of Fe and Sm doped catalysts were studied. The fundamental study on roles of Fe and Sm doping on CeO_2 catalyst were analyzed. All these studies will ultimately assist in improved understanding of ceria-based catalyst for soot oxidation and facilitating the design of DPF.

1.4.Outline of the thesis

This thesis is organized as follows:

- Chapter 1 provides the introduction of the thesis, including research gap, research

objectives, research contribution, and outline of the thesis.

- The literature related to catalytic soot oxidation is reviewed in Chapter 2.

- Chapter 3 summarizes the detailed experimental methods and characterization techniques used in the thesis.

- In Chapter 4, an in situ ETEM study was carried out to do real-time observation of carbon oxidation by driven motion of catalytic ceria nanoparticles within low pressure oxygen (<1 Pa). The main goal of this chapter is to analyze the individual particles behavior during the reaction.

- Chapter 5 evaluates the activity of Fe doped ceria catalysts for soot oxidation, by investigating the nature of the reactive Fe-O-Ce sites. This chapter performed activity and kinetic studies of Fe doped ceria catalyst towards soot oxidation based on bulk particles.

- In order to improve the catalyst stability, samarium doped ceria catalysts were designed and investigated in Chapter 6.

- Chapter 7 gives the conclusions of the obtained results and recommendations for future work.

Chapter 2: Literature Review

This chapter provides the relevant background and literature review used to fulfil this thesis. For diesel engines, the most common method of mitigating soot emissions is using a catalytic diesel particulate filter (DPF) [18, 47], where carbon particles are deposited and then oxidized [48-52]. Ceria (CeO_2) has been shown to be a good candidate for DPF catalyst, as it is naturally abundant, less sensitive to sulfur impurities which poison the catalytic oxidation of carbon PM, and less environmentally toxic during end-of-life recycling [19, 23, 53]. Recently, in order to further improve the activity and stability of ceria catalyst, different metal cations have been used as dopant into the ceria lattice. These dopants effectively inhibit catalyst sintering and increase active sites, both improving the catalyst durability and activity [23, 26-28, 54]. As the catalytic soot oxidation is a surface sensitive reaction, the contact points between soot and catalysts is critical for good catalyst activity [22]. Various morphologies of catalysts produced by different preparation methods also provide different contact points and show diverse activities [55]. Therefore, the appropriate metal doping and morphology of catalysts become essential and important for catalytic soot oxidation, especially in terms of activity and stability.

2.1.Diesel engine emissions

Diesel engine (including biodiesel ones) is a key source of unavoidable air hazardous pollutants such as particulate matter, nitrogen oxides (NO_x) and other organic compounds, due to incomplete hydrocarbon combustion. Soot (a mass of impure carbon particles resulting from incomplete combustion of hydrocarbons) is the second largest contributor to climate change after carbon dioxide; as it absorbs solar radiation, warming the atmosphere, and leading to faster climate change

[1, 2]. This contribution has been estimated at two-thirds the impact of CO_2. Particulate matter has also been shown to be carcinogenic, penetrating deep into the respiratory system, causing a wide variety of health issues. Particulate matter smaller than 10 μm (PM10) can settle within lung tissue and PM2.5 can penetrate deep into the alveolus of the lungs, thus causing lung cancer [2]. These "fine" particles, when released into the atmosphere, have been shown to be carcinogenic, and have been directly linked to increasing long-term risks of mortality [5]. It is therefore necessary to reduce or eliminate diesel engine emissions.

2.2.Diesel particulate filter

For diesel engines, the most common method of mitigating soot emissions is using a diesel particulate filter (DPF) which is installed in the exhaust system of a diesel engine, to capture and burn out soot particles [7, 9, 11, 12, 14, 22]. A schematic of DPF is shown in Figure 1.1. . These filters are in line with the engine exhaust stream, and oxidize soot particles as they pass through the porous monolithic geometry of the DPF [9]. As shown in Figure 1.1. , the exhaust gas enters the filter from the left. Because the cells of the filter are capped at the downstream end, the exhaust gas cannot exit the cell directly. Instead, it passes through the porous walls of the filter cells. In this process, particulate matter is deposited on the upstream side of the cell wall and the cleaned exhaust gas exits the filter to the right.

An excellent DPF is characterized by a high filtration efficiency and a good regeneration process. The filtration efficiency of DPF, which describes the ability of a DPF to deposit particles from engine, is a crucial parameter to evaluate the performance of a typical DPF. An ideal DPF filtration efficiency ranges is from 80% to 90% to sufficiently reduce the exhaust particulates from the diesel engine. However, as the increasing of filter efficiency, it also rises another issue which is the

increase of backpressure, and this can result in undesired higher fuel consumption [56].

As the filter gets saturated once the soot level reaches a certain percentage blocked, the backpressure increases, pushing exhaust gases back into the cylinder and lowering cycle efficiency [57]. In order to avoid blocking the filter, the deposited soot needs to be burned off periodically and this leads to the concept of regeneration. Regeneration is a process to consume the soot accumulated in the filter and thus reduce backpressure. To realize this process, certain temperature is required to oxidize soot, and the exhaust temperatures need to be higher than 600°C in the absence of catalyst. In the absence of catalyst, the exhaust temperatures need to be higher than 600°C to oxidize soot. However, the temperature of the exhaust gas is only around 200-500°C [7, 9, 11]. In order to reduce the cost of adding extra fuel to burn out the deposited particulates, the utilization of a catalyst can effectively reduce the required oxidation temperatures of carbon PM to 200-400°C which is close to the temperature of engine exhaust gases [48].

DPFs utilizing catalysts can be categorized into two modes: DPF enhanced with a catalyst coating directly on its wall (DPF-CC) and DPF collaborated with fuel borne catalysts (DPF_FBC) [50, 51, 58]. For DPF-CC, only a small amount of catalysts is needed as an immobilized thin coating (20 μm [49]) on the DPF's wall, which can reduce the cost. However, replacement of the disabled catalyst coating after aging is tricky. In a DPF-FBC, the catalyst is added directly to the fuel and reaches the DPF together with soot after fuel combustion [51]. For effective operation of DPF_FBC, the catalysts/soot ratio is not too low, which increases the cost, while the maintenance is relatively easy through replenishment with new catalysts [50, 51]. For both modes, the proximity of soot and catalysts is an important factor for efficiency [52]. In DPF_CC, the structure of the catalyst coating and the soot deposition on it affect the contact [58]. A porous coating leads to

higher soot mobility and thereby a more intimate contact during exhaust emission than a dense coating [49]. In DPF_FBC, a homogeneous dispersion as well as tight contact of soot and catalysts are achieved during exhaust emission [50, 51].

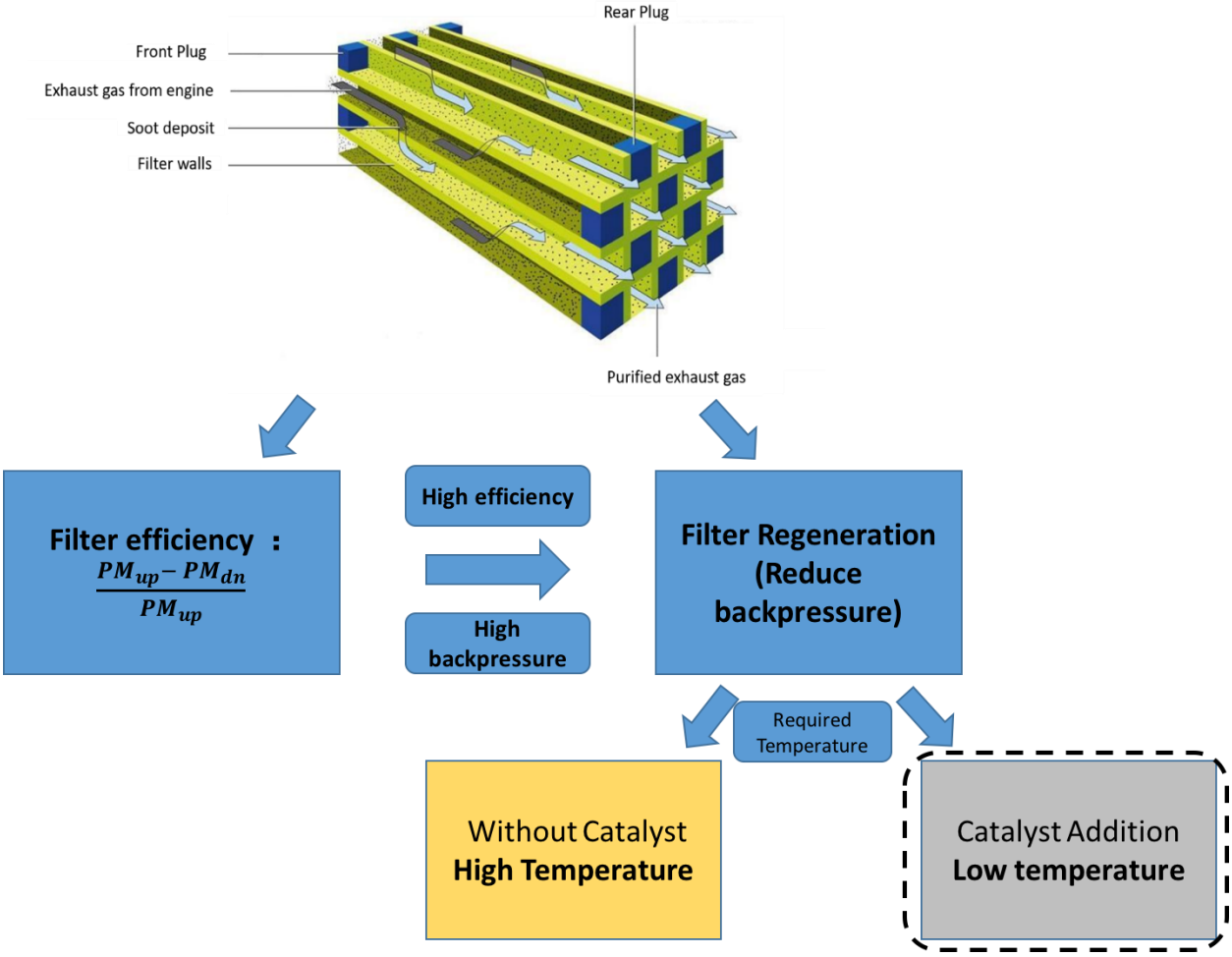

Figure 1.1. Diesel particulate filter (modified with use of [59])

2.3. Catalytic soot oxidation

2.3.1. Catalysts used for soot oxidation

Noble metal based catalysts have been widely used as catalysts for soot oxidation in recent years,

thanks to their high activity and durability [60, 61]. However, their high cost, sensitivity to sulfur poisoning and limited availability have motivated researchers to develop alternative low-cost catalysts [62]. Three kinds of non-noble catalysts have been found effective in soot oxidation [63]: 1) Ceria based catalysts have drawn attention because of their good redox behavior and oxygen storage ability [11, 12, 47, 57, 64-66]; 2) Perovskite/spinel/hydrotalcite/delafossite catalysts have attracted significant interests due to their high stability and their capability for NO_x decomposition [67-70]; 3) Other metal oxide catalysts, such as LaO_x, alkaline and alkaline-earth metal oxides, which have been also applied as catalysts for soot oxidation because they are rather stable and easier to synthesize [9, 71-74].

The desired catalyst for soot oxidation should have high activity, suitable stability, and low cost, which makes ceria-based catalysts particularly attractive [22]. Ceria-based catalysts have been found to be the most promising because of their excellent redox abilities, outstanding oxygen storage capacity and affordable price [22]. This is the reason that ceria-based catalyst has been chosen for this thesis, and only ceria-based catalyst will be discussed in the following parts of the thesis.

2.3.2. Metal-doped ceria catalysts

The activity and durability of ceria-based catalysts can be further improved through doping or incorporating other metal additives into the cerium oxide lattice in order to enhance oxygen storage capability (OSC) and oxygen mobility [22, 63]. As indicated by Bueno-López et al. [8], the crystal size of CeO_2 grows rapidly at temperatures above 500°C, while the size of the doped ceria grows much milder or remains even constant in a wider temperature range. Consequently, the modified ceria exhibits higher soot oxidation activity than CeO_2.

Noble metals such as Pt, Au, and Ru doped CeO_2 catalysts have shown superior activity for soot oxidation [75, 76]. Transition metals doping such as Fe, Mn and Cu have been reported to promote ceria assisted catalytic soot oxidation as they produce more active sites over the surface [29-32]. Iron, in particular, is prominent because it can enhance the activity of CeO_2 due to its good redox ability - the oxygen species can alternate between Fe^{3+} and Fe^{2+} [5, 22, 33]. Rare-earth metal such as Sm, Zr and Hf have been studied as additives into CeO_2 for soot oxidation. These catalysts have shown to increase catalyst stability, but at the cost of lower activity [43]. Although alkali and alkali-earth metals such as K, Cs and Ba incorporated into ceria can barely improve the redox properties of the catalysts, they can increase the contact points between soot and catalyst due to the high mobility of alkali metals [33, 77-79].

2.3.3. Morphologies of catalysts

The process of catalytic soot oxidation is strongly limited by two factors: 1) poor soot/catalyst contact and 2) restricted active site activity [43]. In order to overcome these limitations, morphology control based on material synthesis and preparation processes has already been devoted to develop novel ceria-based catalysts for soot oxidation. So far, there have been mainly five different types of ceria-based soot oxidation catalysts with tailored morphologies, as shown in Figure 2.2 and Table 2.1 [22, 43].

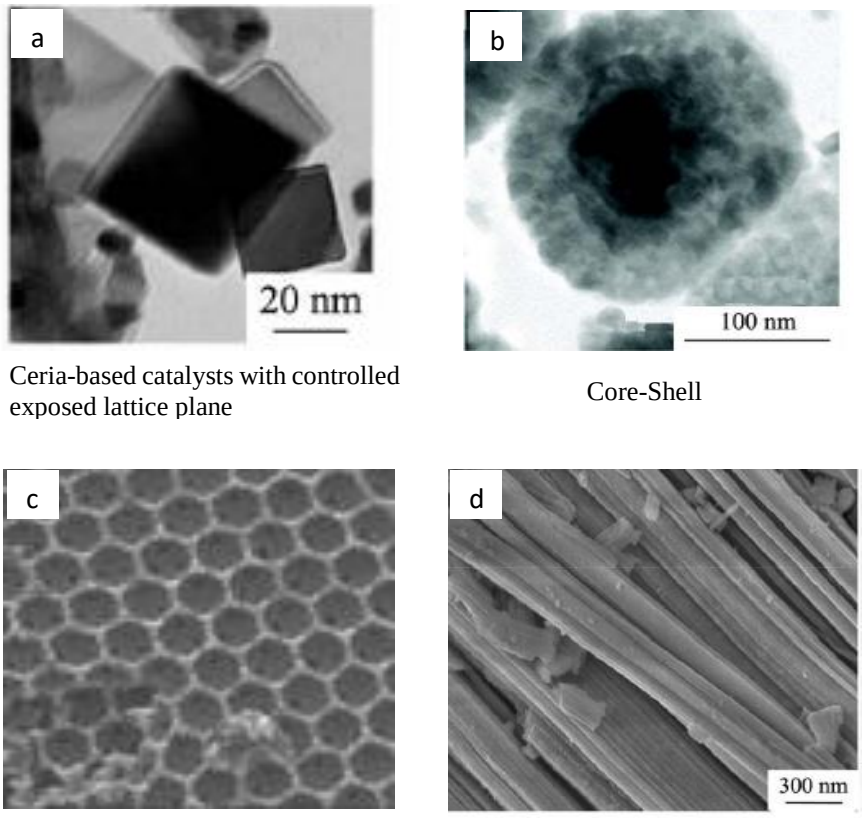

Ceria-based catalysts with controlled exposed lattice plane

Core-Shell

3DOM

Nano fibers

Figure 2.2. Different catalysts morphologies [80-83]

Table 2.1. Summary of catalysts morphologies

Morphology	**Advantages**
Ceria-based catalysts with controlled exposed lattice plane [80, 84, 85]	Ceria with more exposed planes belonging to the (100) and (110) families exhibits better activity than those with more (111) faces
Core-Shell [24, 81, 86-88]	Facilitate the interaction between different components in the catalysts, and improve the reactivity of the active sites

Three dimensionally Ordered macroporous (3DOM) [82, 89-92]	The pore sizes are enlarged enough to permit diesel soot to enter their inner pores, thus increase number of contact points
Nanostructured catalyst [23, 28, 85, 93-95]	Their surface atoms have high surface energy and mobility, which may improve the catalyst-soot contact especially under a loose contact mode
Fiber [63, 96-99]	A promising way to maximize the number of catalyst-soot contact points

Researchers have studied the influence of various morphologies on catalytic soot oxidation under different contact conditions [22, 63, 96]. They found that different morphologies exhibit various catalytic activities, which are strongly dependent on the particle size along with their own physical and chemical surface properties.

As the catalytic soot oxidation is a surface sensitive reaction, the contact points between soot and catalyst particles have a great impact on activity [4]. Nanostructured catalysts have been widely investigated recently for many catalytic applications because of their notable nanometer sizes, which result in a high surface-to-volume ratio and render their chemical and physical properties more size and shape dependent [100, 101]. More specifically, the higher surface areas make these nanostructured catalysts possess more contact points between the soot and catalyst particles, while the meso-scale pores (with diameters between 2 and 50 nm) within these nanostructured catalysts

promote the oxygen diffusion through catalysts [100]. Among these preparation methods, co-precipitation (CP) method has been widely used for catalyst preparation due to the formation of higher surface area and smaller crystal size [29]. Alternatively, solution combustion synthesis (SCS) is a time effective and energy saving method to produce nano-sized porous catalysts [102]. Herein, these two preparation methods have been chosen in this study to investigate the morphologies influence on catalyst activity.

2.3.4. Mechanism of ceria-based catalytic soot oxidation

The catalytic performance of ceria based materials is related to their oxygen storage/release capacity [34] and their ability to produce peroxide (O_2^{2-}) or superoxide (O_2^-) species [53, 62]. Ceria acts as an active oxygen producer to promote the formation of reactive oxygen species and transfer them to the soot catalyst interface to oxidize soot, which is described in the so-called active oxygen-assisted oxidation mechanism [22, 25]. The oxidation mechanisms of carbon particles using a pure CeO_2 catalyst are illustrated in Figure 2.3 a) [22, 29]. During the reaction, ceria provides lattice oxygen for soot oxidation and creates oxygen vacancies through Ce^{4+} to Ce^{3+} reduction, followed by refilling of environmental oxygen into its crystal accompanied by absorbing gaseous oxygen via Ce^{3+} to Ce^{4+} [4, 5, 29, 62, 63], which produces active superoxide O_2^- [53, 62, 103] as well as O_2^{2-} [62, 103].

The mechanism of iron doped ceria catalysts has been investigated by Zhang et al. [29], as shown in Figure 2.3 b, highlighting the important role played by the redox cycle of iron in this reaction. Fe^{3+} can provide its bonded active oxygen to oxidize soot through its reduction to Fe^{2+}. Fe^{2+} can then be re-oxidized to Fe^{3+} with the interaction of Ce [22, 29]. The number of active Fe-O-Ce sites can vary due to different ratios of iron doping, as iron doping can distort the fluorite lattice and

create oxygen vacancies to varying degrees. Thus, the ratio of iron doping in ceria affects the catalyst activity and needs to be optimized with reaction conditions.

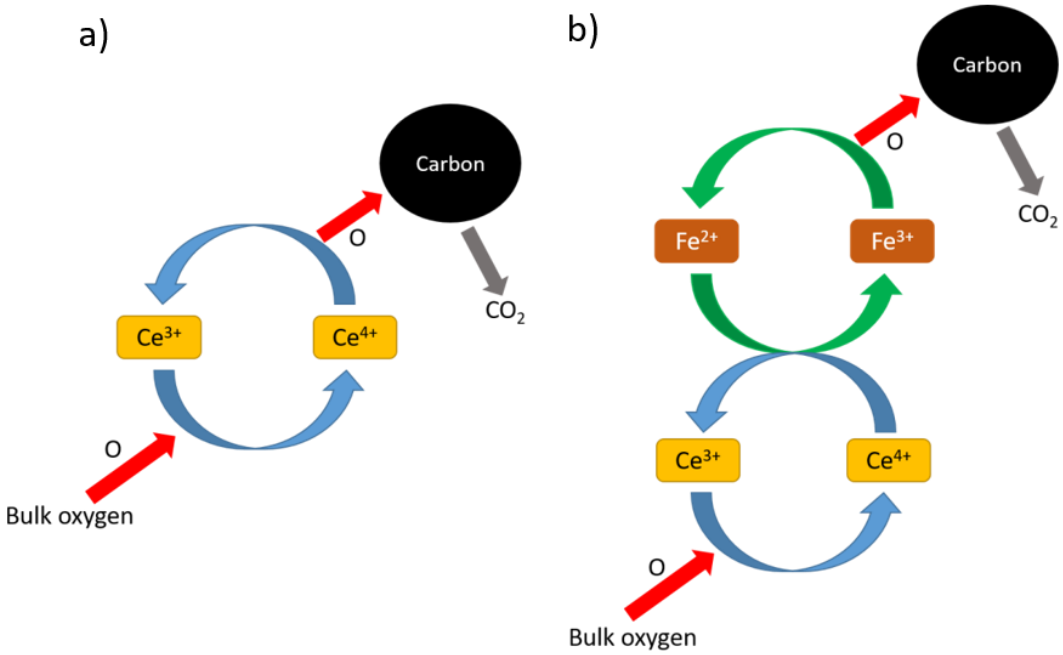

Figure 2.3. Mechanisms of carbon oxidation with a) CeO_2 and b) Fe-CeO_2 catalyst. Red arrows represent oxygen transfer, blue arrows represent the ceria state change cycle, and green arrows represent the iron state change cycle. (reproduced based on references [22, 29])

2.3.5. Oxygen vacancies in catalyst

Different iron doping ratio and morphologies would vary the surface properties and oxygen vacancies of catalysts, which has been found to be important for catalyst activity [104]. Kattal et al. [27] found that increasing oxygen vacancies induced more active oxygen of CeO_2–La_2O_3 catalyst for soot oxidation. Pr, La, Tb doped CeO_2 catalysts were studied for methane steam reforming, revealing that increased oxygen vacancies contributes to higher activity [105]. Oxygen vacancy of Ag-doped perovskite catalysts was found to be the primary intermediates for the NO

oxidation reaction [106]. Zr doped CeO_2 catalyst showed positive relation between oxygen vacancy concentration and catalyst activity for dimethyl carbonate synthesis [107]. All the above research showed a positive relation between oxygen vacancy and catalyst activity. However, the effect of oxygen vacancy on soot oxidation by altering the catalyst morphologies along with different metal doping ratios is still poorly understood.

2.3.6. Contact conditions between soot and catalyst

The contact points between the carbon and catalysts is a critical factor for determining the process efficiency and the cost of the device, as catalytic carbon PM oxidation is a surface sensitive reaction.

A “Loose” contact condition is obtained by gently shaking the catalyst and soot mixture with a spatula. This procedure is sufficient to homogenize the mixture, but still allows the two solid phases to be put in contact loosely. Although the procedure is very short (1–2 min), the established contact leads to reproducible catalytic performances. Neeft et al. [38] observed that the contact between the catalyst and soot in a DPF is as loose as that of materials mixed roughly with a spatula. Therefore, loose contact conditions would be representative of the conditions in an actual DPF.

A “Tight” contact condition is usually prepared through in a mortar or ball milling to obtain close contact between the catalyst and soot. This method maximizes the number of contact points, but it is less representative of the real contact conditions that occur in a catalytic trap [13]. The tight contact condition is used to investigate the intrinsic activity of catalysts and to determine the kinetics of catalytic soot oxidation.

2.3.7. Techniques of investigation on catalytic soot oxidation

Thermogravimetric Analysis (TGA) and Temperature programmed oxidation (TPO) have been widely used to investigate the activity of catalysts for soot oxidization [13, 22, 27, 43, 108]. Different characterization techniques including X-ray diffraction (XRD), Brunauer-Emmett-Teller (BET), X-ray photoelectron spectroscopy (XPS), H_2-Temprature programmed reduction (H_2-TPR), Raman, and Scanning electron microscopy (SEM) have enabled researchers to find out the mechanism for high activity of catalysts for soot oxidization [12, 27, 43, 108]. Furthermore, some advanced in-situ techniques such as Environmental transmission electron microscopy (ETEM), in-situ Ultraviolet–visible spectroscopy (UV-VIS) offer an opportunity to monitor the real time change of catalysts during the reaction [109]. Numerical models have also been constructed to study the effect of catalyst activity on soot oxidization and soot distribution in DPF [110-113].

Among these techniques, ETEM is a promising technology for situ observation of a reaction. The image captured from ETEM video could be used to reveal the interaction between nano-sized carbon and catalyst particles during reaction, by allowing the observation of particle shape changes and motions in a controlled temperature and gas pressure atmosphere [21, 114-116]. Sediako et al. [115] used ETEM to observe the oxidation mode of mature and less mature soot particles in real time. It was found that mature soot was oxidized through its surface, while the less mature soot (collected at lower flame) showed surface oxidation, as well as internal oxidation with penetration of oxygen into the core of soot particles. Kamatani et al. [116] utilized in situ Transmission electron microscopy (TEM) to visualize catalytic soot oxidation using Ag/SiO_2 and Cs_2CO_3 at 300°C under 0.5 Pa O_2. They observed the catalytic reaction happened at the soot-catalyst interface with mobile Ag species and immobile Cs based catalyst. The mobility of Ag/SiO_2 catalyst is considered as a

result of heat released from carbon oxidation and partial liquefaction of Ag surface, while the fixed Cs_2CO_3 was due to strong interaction with the substrate. Gao et al. [117] applied ETEM to investigate Ag catalyst on alumina and sulphated alumina supports for soot oxidation. Sulphated alumina was able to anchor the Ag catalyst thus making carbon particles move towards Ag species. Baker et al. [118, 119] used a controlled atmosphere electron microscope (CAEM) to investigate the catalyst (2-5 nm) behavior during the gasification of carbon and graphite particles (original in 1μm, 2-20 nm after treatment). They proposed the concept of channeling catalysis, during which the reaction begins at the catalyst/graphite interface and proceeds through channels generated within the graphite crystal. Simonsen et al. [21] studied the oxidation of carbon black (30 nm) using CeO_2 catalyst agglomerate (50-100 nm) and observed that these carbon particles moved to reach CeO_2, followed by the catalytic combustion at the carbon/catalyst interface. Another study by Mori et al. [17] reported a similar motion of carbon black particles (around 10-20 nm) towards an aggregated catalyst cluster made of Ag/CeO_2 and $Cu/BaO/La_2O_3$ cluster (around 200-300 nm). Others reported the motion of carbon particles of around 20 nm that were approaching an agglomerate of yttria-stabilized zirconia catalysts during catalytic oxidation [120]. Interestingly, there has been no report in the literature on observing nano-sized ceria based catalyst moving towards the carbon particles, which could provide insight on particle-particle interaction and subsequently the reaction mechanism of catalyzed oxidation of particulate matters.

2.3.8. Stability of ceria-based catalysts

It was reported that active sites, crystal structures and surface properties of ceria-based catalysts could change during the reactions, resulting poor stability (loss of catalytic activity) of ceria-based catalysts [121]. All studies agreed that pure CeO_2 shows poor stability for soot oxidation, which

has become a major obstacle for widely applications of ceria-based catalysts [34, 121-123]. Liang et al. [121] have studied the thermal stability of CeO_2 for soot oxidation by aging the catalyst at 800°C for 20 hours in air. They found that the temperature corresponding to the maximum rate for CO_2 production with aged catalyst increased by about 60°C compared to fresh catalyst, because of the highly reduced surface area and sintering. Aneggi et al. [34] observed that aging CeO_2 catalyst at 750°C for 12 hours in air decreased its activity for soot oxidation as it lost oxygen storage capacity. Liu et al. [122] investigated the deactivation of CeO_2 for soot oxidation through isothermal conditions at 300 and 350°C; they found that deactivation occurred at isothermal conditions and became more severe at higher temperature. The essential reason for deactivation is inefficient O_2^- formation. Corro et al. [123] tested the stability of CeO_2 towards soot oxidation during 6 cycles and found a slow and continuous deactivation of CeO_2.

Therefore, the stability of CeO_2 based catalysts for soot oxidation needs to be improved. Many studies have looked at the incorporation of metal dopants into CeO_2 lattice to improve stability, as described next. Wu et al. [8, 41, 44, 102] added BaO or Al_2O_3 into transition metal (Mn, Cu) doped CeO_2 to improve its thermal stability. They found that these metals could improve the thermal stability after aging at 800°C for 24 hours in air because they hinder crystal growth. Aneggi [34] and Liang et al. [121] incorporated ZrO_2 into Fe-Ce and Cu-Ce mixed oxides and found enhanced thermal stability due to the formation of stable solid solutions. Gao et al. [124] have aged Nd-Ag/CeO_2 catalyst at 700°C for 48 hours under 1%O_2/10%H_2O/N_2, revealing Nd could prevent crystal growth, thus improving thermal stability of Ag/CeO_2. Xiong et al. [125] have added Y and La into Zr/CeO_2 catalyst and aged it from 700 to 1000°C. The catalyst activity remained stable below 800°C and decreased significantly above 900°C. Zhang et al. [126, 127] investigated the

influence of thermal stability by adding Y into MnO_x-CeO_2 and introducing Al, La, Y, or Zr into Pt/MnO_x-CeO_2 after aging at 800°C for 12 hours in air. They observed that incorporation of dopants could prevent the sintering and slow down crystal growth. Peralta et al. [79, 128] introduced Ba into alkali metals-modified ceria such as K/CeO_2 and obtained good thermal stability as no deactivation was observed after aging at 800°C. Noble metals, such as Ru, have also been investigated as dopant to successfully improve ceria-based catalyst stability after aging at 800°C in O_2 [129]. Doing several cycles of metal-doped ceria catalyst also becomes very important. Although all the studies described previously investigated stability through accelerated thermal aging, a few studies investigated stability through more realistic, albeit more cumbersome, soot oxidation cycles [92, 130-132]. La loaded on CeO_2-ZnO (5 cycles) [132], K added into CeO_2 (3 cycles) [130], co-doping of Ag and Mn into CeO_2 (3 cycles) [131] and Au doped $Ce_{0.8}Zr_{0.2}O_2$ (3 cycles) [92] all showed enhanced stability of ceria-based catalysts for soot oxidation. These studies identified that resistance of sintering and crystal growth, ability of CO_2 desorption, and oxygen species replenishment are important roles for catalyst stability on soot oxidation.

Ceria-based catalysts have been investigated, in particular stability, for applications other than soot oxidations [133, 134]. One family of applications relates to catalytic combustion of different gases. Dai et al. [135] investigated the stability and deactivation of CeO_2 catalyst and found that T50 increased from 165°C to 325°C after nine cycles of trichloroethylene combustion. Zhang et al. [136] studied Al, Zr, La, or Y doped Pt/MnO_x-CeO_2 stability toward NO oxidation after aging, observed that modified ceria catalyst showed better activity. Han et al. [134] investigated the stability of ZrO_2-doped CeO_2-based catalyst for toluene combustion, revealing that ZrO_2 can stabilize the surface active structure, thus improving stability. Polychronopoulou et al. [137] investigated Sm_2O_3/CeO_2 catalysts for CO oxidation, finding that adding Sm can significantly

improve the thermal stability of conventional CeO_2 catalyst. Mandal et al. [138] have demonstrated enhanced stability of Gd-Sm-CeO_2 for benzyl alcohol oxidation. Another important family of applications using ceria-based catalysts is solid oxide fuel cell (SOFC) (and its reverse operation solid oxide electrolysis, SOEC) for intermediate temperature (650-750°C). The main ceria-based material investigated for SOFC and SOEC are samarium doped ceria (SDC) [139, 140] and Gadolinium doped ceria (GDC) [133, 141]. Sm and Gd were added essentially to stabilize ceria during operation at high temperature, which can inhibit crystal growth and prevent sintering [147].

From the above literature review on stability of ceria-based catalyst, it is somewhat surprising to see almost no studies on samarium doped ceria despite proven long-term stability at high temperatures (750-850°C) in SOFC/SOEC. Granted, SDC in SOFC/SOEC has a different purpose (electrolyte to transport oxygen ion) than it would have in soot oxidations. Yet, SDC should be a promising stable catalyst for soot oxidation because of its thermal stability at high temperatures. Very few papers studied Sm as dopant to ceria for soot oxidation. Liu et al. [93], using loose contact condition, studied activity and thermal stability (calcination at 800°C for 20 hours) of a 20% Sm-doped ceria catalyst prepared through microwave assisted heating decomposition. Sudarsanam et al. [142] carried out a similar study, except under tight contact condition and with co-precipitation catalyst preparation method. Both reported increase in combustion temperatures after aging, but were not conclusive regarding actual catalyst stability. Anantharaman et al. [143] did not investigate catalyst stability, but studied the effect of Sm content on soot oxidation reactivity for Sm-doped ceria catalyst prepared by ethylene-diamine-tetraacetic acid (EDTA) - citrate method; they found that 10% Sm doping performed best on a fresh catalyst calcined at 600°C for 5 hours.

Chapter 3: Experimental Methods and Characterization Techniques

3.1. Catalyst preparation methods

3.1.1. Co-precipitation method

Fe_xCe_{100-x}-CP (x = 0, 5; 10; 20; and 30, molar ratio) catalysts were synthesized by a co-precipitation (CP) method. A stoichiometric solution (depending their relative ratio) of iron nitrate nonahydrate $Fe(NO_3)_3 \cdot 9H_2O$ (Sigma-Aldrich, CAS: 7782-61-8, 99.95% trace metals basis) and cerium nitrate hexahydrate $Ce(NO_3)_3 \cdot 6H_2O$ (Sigma-Aldrich, CAS: 10294-41-4, 99.999% trace metals basis) was dissolved separately in deionized water and then mixed together with vigorous agitation. Aqueous ammonia (Sigma-Aldrich, CAS:1336-21-6, 28%-30% NH_3 basis) was then gradually dropped into the as-mentioned solution under stirring conditions until pH reached 8.5, after which the solution was aged in air for one day at room temperature with constant stirring. The resultant precipitates were separated by vacuum filtration and several times washed with deionized water to eliminate impurities such as unreacted chemicals. The obtained precipitates were dried at 100°C in a crucible for 12 h and then calcined at 500°C for 5 h in air. Pure cerium oxide - CeO_2 and Samarium doped Ceria (SDC) were also prepared by a similar procedure with using Samarium nitrate hexahydrate $Sm(NO_3)_3 \cdot 6H_2O$ (Sigma-Aldrich, CAS: 13759-83-6, 99.999% trace metals basis).

3.1.2. Solution combustion synthesis method

Fe_xCe_{100-x}-SCS (x = 0, 5; 10; 20; and 30, molar ratio) catalysts were obtained by a solution combustion synthesis (SCS) method. The preparation procedure of SCS method is shown in Figure

3.1. An aqueous solution of iron nitrate nonahydrate $Fe(NO_3)_3 \cdot 9H_2O$ (Sigma-Aldrich, CAS: 7782-61-8, 99.95% trace metals basis), cerium nitrate hexahydrate $Ce(NO_3)_3 \cdot 6H_2O$ (Sigma-Aldrich, CAS: 10294-41-4, 99.999% trace metals basis) and glycine (Sigma-Aldrich, CAS: 56-40-6) in a stoichiometric ratio (depending on their relative ratio) were mixed under vigorous stirring at 90°C to form a gel. The gel was moved from a beaker to a crucible using a spatula which was placed on an electric heating plate (Salton Canada, Canada). The gel was then heated up until ignition occurs to start the combustion leading to the formation of nano to micro size particles. A long glass tube was put on the top of the crucible to contain the resulting particles and to allow for collecting the fine powder after combustion. After the reaction, the resultant sample was collected into the crucible and then calcined at 500°C for 5 h in air in a furnace. CeO_2-SCS and Sm doped ceria catalysts were synthesized by a similar procedure with using Samarium nitrate hexahydrate $Sm(NO_3)_3 \cdot 6H_2O$ (Sigma-Aldrich, CAS: 13759-83-6, 99.999% trace metals basis).

Figure 3.1. Experimental apparatus for solution combustion synthesis (SCS) catalyst preparation

3.2. Catalyst activity test

Thermogravimetric Analysis (TGA) for catalytic soot oxidation was conducted on a TA Instrument Q500 apparatus to investigate the catalytic activity. Printex-U carbon black with particle size of 25 nm and 100 m^2g^{-1} surface area was used as model of soot, which has been widely used as soot substitute in research studies [10, 13, 22, 29]. Tight contact condition mixture was obtained by grinding soot and catalyst with a weight ratio of 1:9 in an agate mortar for 10 minutes [13]. Loose contact condition was obtained by using a spatula gently mixing catalysts and soot for 3 min. For each TGA test, a weighted amount of 10 mg of the soot/catalyst mixture was put in a TGA pan, and then pre-treated at 150°C under 60 ml/min nitrogen for 30 min to remove water. Then, the sample was heated up to 800°C under 40 ml/min air with a heating rate of 10°C /min. The thermogravimetric curves were obtained by continuously recording the mass change, along with increased temperature. Each TGA test was repeated three times to determine the uncertainties with the results. The catalyst's activity was evaluated by T10 and T50. T10 is commonly used as the ignition temperature, which is the temperature at 10% conversion of soot [7, 9, 10, 13]. T50 is the combustion temperature, which is identified by the temperature when 50% of soot is oxidized [7, 11, 12, 14].

Temperature programmed oxidation (TPO) were also carried out using CATLAB (Hiden Analytical). CATLAB is a system that combines a microreactor and mass spectrometer for conducting catalysts characterization and studying catalytic reactions. The sample is put into the reactor on the top of quartz wool. After inert gas passing through for about 20 minutes, 10% O_2 in He is flowed into the reactor at rate of 40 ml/min. The temperature ramped from room temperature up to 800°C at 10°C/min. During the reaction, the mass spectrometer records different species that

are produced from the reaction, here specifically CO and CO_2 for soot oxidation. By analyzing these data, we can study the activity of catalyst and the ability of our catalyst to convert CO and CO_2.

3.3. Environmental transmission electron microscopy (ETEM) experimental set up

The ETEM is a TEM that enables the observation of specimen under a gas-controlled environment. A small volume around the specimen is filled with desired gases so that the pressure of that volume is kept higher than that of the TEM column. The ETEM experiments were designed to visualize the reaction and the mobility of soot and catalyst particles under various conditions of temperature (500 and 800°C) and oxygen partial pressure (1 Pa oxygen and 1 Pa air) by using ETEM. Printex-U commercial carbon black powders with an average particle size of 25 nm were used as a surrogate of soot. The catalyst used was Fe/CeO_2 (10 % iron doping) with a size around 20 nanometers made by combustion solution synthesis method. The soot and the catalyst were mixed in a weight ratio of 1/9, and the sample mixtures were then drop coated onto microelectrical mechanical system (MEMS) substrates (Norcada Inc. Model: HTN-010).

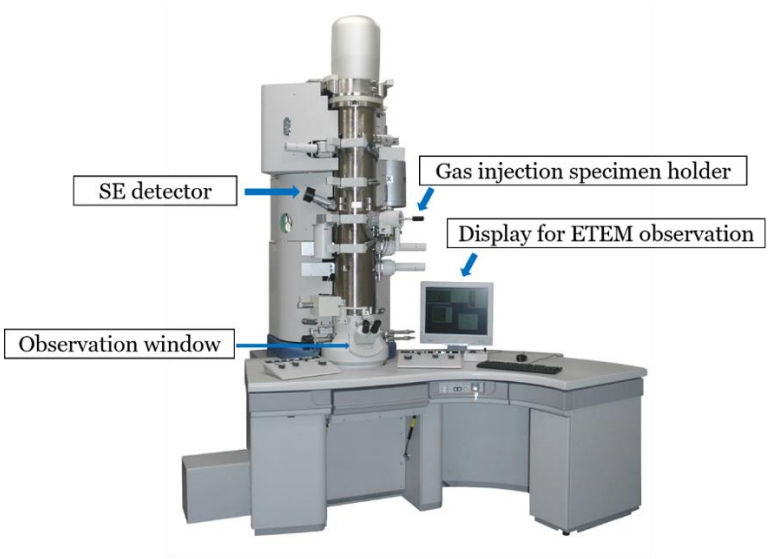

Figure 3.2. Arrangement of Hitachi HF3300 [144]

The experiments for catalytic soot oxidation were conducted with a Hitachi HF3300 ETEM, functionalized by a secondary electron detector, gas injection and sample heating. To enhance contrast and increase the resolution, all imaging was done at 300 kV [120]. Sensitivity tests were also carried out to ensure that the observed phenomenon was not influenced by the electron beam, the gas flow, or the sample/substrate interactions. All tests were conducted following the procedures established by a previous study as following [115]: 1) Beam flashed and adjusted with sample withdrawn and high vacuum; 2) Sample pre-heated to 400°C and then inserted into the beam; 3) Particles selected, focused and recorded; 4) Temperature raised to experiment temperature at 5°C/s; 5) Gas injection started; 6) Conditions maintained until the reaction completes; 7) Gas off / cool down.

3.4. Stability test

The stability of catalysts was tested with up to seven times cycle reaction using a TGA. Firstly, 40 mg mixture of catalyst (90 wt.%) and soot (10 wt.%) were put in a TGA, then following the normal TGA operation procedure as described in section 3.2. After the test, the spent catalyst was collected and then mixed with fresh soot particles again with the same weight ratio and under same contact condition. Then, this sample is analyzed through TGA again. This procedure is repeated up to seven times and the thermogravimetric results (in particular T10 and T50) are recorded for each cycle. These results are used to analyze the stability of the as-produced catalysts.

3.5. Characterization techniques

3.5.1. X-ray Diffraction (XRD)

XRD is a characterization technique used for the determination of crystal structure, chemical

composition and physical properties. X-ray diffraction peaks are produced by constructive interference of a monochromatic beam of X-rays diffracted at specific angles from each set of lattice planes in a sample. The peak intensities are determined by the distribution of atoms within the lattice. Consequently, the X-ray diffraction pattern is the fingerprint of the periodic atomic arrangements in a given material. A search of the International Centre for Diffraction Data (ICDD) database of X-ray diffraction patterns enables the phase identification of a large variety of crystalline samples. The crystal size can be estimated by using the Scherrer equation, as shown in Equation 3-1, and inter planar spacing (d) can be calculated by Bragg's law as shown in Equation 3-2.

$$D = \frac{k\lambda}{\beta cos\theta} \tag{3-1}$$

$$n\lambda = 2dsin\theta \tag{3-2}$$

where D is the mean size of the crystalline domains, k is a dimensionless shape factor (around 0.9, but varies with the actual shape of the crystallite), λ is the wavelength of the X-rays, β is the line broadening at the half the maximum intensity (FWHM), θ is the incident angle, and d is the inter planar spacing. n is the order, a positive integer, usually 1.

3.5.2. Brunauer–Emmett–Teller (BET) surface area

The surface area was measured by means of N_2 adsorption-desorption isotherms. BET theory is used to measure the specific surface area and porosity of the materials. BET surface area measurement is based on gas molecules adsorption on a solid surface. BET theory builds upon the foundational Langmuir adsorption theory, which provides a model for monolayer molecular adsorption, and extends this theory to multilayer adsorption. Nitrogen is the most commonly

employed gaseous adsorbate used for surface probing by BET methods. For this reason, standard BET analysis is most often conducted at the boiling temperature of N_2 (77 K). Specific surface area is a scale-dependent property, with no single true value of specific surface area definable, and thus quantities of specific surface area determined through BET theory may depend on the adsorbate molecule utilized and its adsorption cross section.

3.5.3. Scanning Electron Microscopy (SEM)

Scanning electron microscopy (SEM) is an equipment used to observe and analyse the morphology, microstructure and surface features of materials at micro and nanoscale. With the focused beam of electrons hitting the sample, the interactions between electrons and atoms will emit different kinds of signals such as secondary electrons and backscattered electrons. Then, by detecting various signals, mainly secondary electrons and converting them to electronic signals, a SEM image can be obtained. SEM will be used to investigate the distinct nanostructures of the synthesized and spent iron doped ceria oxide catalysts.

3.5.4. Energy-dispersive X-ray Spectroscopy (EDS)

Energy-dispersive X-ray Spectroscopy (EDS) is used to identify and quantify the chemical composition of the sample. Given that each element produces unique characteristic x-ray when bombarded with high energy electrons inside SEM or TEM, EDS employs detectors which sort incoming x-ray signals according to intensity. This is typically accomplished through a semiconductor detector such as silicon or germanium doped with lithium. Characteristic x-rays bombard the detector, creating a fixed number of electron-hole pairs, which are translated into voltage/energy to be processed electronically.

3.5.5. Transmission Electron Microscopy (TEM)

TEM is widely used in imaging nanostructures, atomic arrangements, and crystal orientation. TEM is the technique that allows direct visualization of samples' morphologies on the nanometer scale by a beam of electrons transmitted through an ultra-thin specimen to form an image. The image is then magnified and focused onto an imaging device. High-resolution TEM imaging can even show the atomic level morphology. Scanning transmission electron microscopy (STEM) imaging of a sample performs scanning of a finely focused electron beam in a faster pattern and collect the signal generated pixel by pixel.

3.5.6. X-ray Photoelectron Spectroscopy (XPS)

XPS is a surface sensitive technique used to investigate the surface chemistry of the sample, such as elemental composition, chemical state, and electronic state. In principle, the sample is irradiated by a beam of X-rays with a known energy. With the interaction between electrons and the sample, a number of electrons would escape from the top surface (0 to 10 nm). By detecting and analyzing the kinetic energy and number of escaped electrons, the binding energy spectrum versus the number of electrons can directly identify the elements on the surface of the sample and provide the relative amounts of each element. XPS spectra-fits can be performed with Gaussian-Lorentzian functions by using specific software (like CasaXPS here).

3.5.7. Raman Spectroscopy

Raman spectroscopy is a spectroscopic technique used to study the vibrational, rotational and other low frequency modes of the crystal lattice of a material. The inelastic scattering spectra with different frequencies of incident light is usually used to excite the visible light and to obtain

molecular vibration and rotation information of the sample. With the interaction between laser and the system phonon, the final photon energy would increase or decrease. By getting the information of these changes in energy, the phonon mode can be learnt and thus applied to the study of molecular structure. Raman spectroscopy is commonly used in chemistry to provide a structural fingerprint by which molecules can be identified.

3.5.8. H_2-Temprature programmed reduction (H_2-TPR)

H_2-TPR, which is often used in the field of heterogeneous catalysis, is a characterization technique used to study the reducibility of the catalysts and find the most efficient reduction conditions of the material. The oxidized material is placed inside a fixed bed reactor and a reducing gas (e.g. 10% H_2 in Ar) is flowed at a constant rate with temperature increasing. When the temperature reaches a certain point, the material would begin its reduction. The reduction of the material is directly related to H_2 consumption. Through TPR characterization, the chemical state change, the interaction within the material, the interaction between the material and the carrier, and the reduction activation energy of the oxidized material can be obtained.

Chapter 4: Real-Time Observation of Carbon Oxidation by Driven Motion of Catalytic Ceria Nanoparticles within Low Pressure Oxygen

4.1. Overview

Carbon particulate matter (PM) is an undesirable aerosol pollutant formed from combustors such as power plants, refineries, and engines. The most common and effective method of mitigating PM emission is the capture of particulates using a filter, before particles are released into the atmosphere. In order to develop and improve advanced filtering materials, a better understanding is required of their chemical and mechanical behavior. We report on a novel phenomenon on the mobility and oxidation behavior of catalytic iron doped ceria nanoparticles in contact with mobile carbon black nanoparticles. The process is recorded by real time imaging within an environmental transmission electron microscope. In contrast to observations in previous studies, the separated ceria nanoparticles are found to actively move on the substrate and consume the connecting carbon particles one-by-one. The velocity of particle motion is correlated to the reaction temperature and oxygen pressure, both determining the reaction rate. Modeling using the Density Functional Theory suggests that this motion is driven by the chemical bonding between the surface oxygen of the catalyst and the graphite layers of carbon black, initiated through the van der waals force between two types of nanoparticles.

4.2. Introduction

There is an urgent need to develop novel materials for capturing and reducing particulate emissions from a wide range of combustion sources. Soot, as one type of particulate matters (PM), is an undesirable aerosol pollutant which forms in fossil fuel power plants, refineries, and internal combustion engines [1, 2]. These fine carbonaceous particles, when released into the atmosphere, have been shown to be carcinogenic and directly linked to an increase in mortality rates [16]. For many sources, the most common and effective method of mitigating carbon PM emission is the capture of particulates using a filter, before they enter into the atmosphere. Advanced materials have been sought for developing high-efficiency filters, especially for these particulates with a size below 10 nm. For internal combustion engines, a diesel particulate filter (DPF) is usually install in line with the exhaust stream from the engine [18]. When the DPF is saturated with the deposited particulates, it must be cleaned or replaced, to avoid increasing the back-pressure of the engine which affects the vehicle operation [17]. In order to reduce the cost of adding extra fuel to burn out the deposited particulates, a catalyst can effectively reduce the oxidation temperatures of carbon PM to 200-400°C which is close to the temperature of engine exhaust gases [48]. DPFs utilizing catalysts can be categorized by the method through which the catalyst is introduced: DPF enhanced with a catalyst coating directly on its wall (DPF-CC) and DPF utilizing fuel borne catalysts (DPF-FBC). For DPF-CC, a small amount of catalysts is immobilized as a thin coating (20μm [49]) on the wall of DPF, which can reduce the oxidation temperature during regeneration. In a DPF-FBC, the catalyst is added directly to the fuel at a concentration of around 10ppm and reaches the DPF to oxidize carbon PM at a lower temperature [50, 51, 58]. For both type of enhanced DPF, the contact points between the carbon and catalysts is a critical factor for determining the process efficiency and the cost of the device, as catalytic carbon PM oxidation is

a surface sensitive reaction. In literature, the structures of the coated catalyst and carbon deposition were found to affect the capability of a DPF-CC [52]. It was suggested that a porous catalyst coating leads to more contact points between catalyst and carbon PM [49]. For DPF-FBC, a homogeneous dispersion as well as intimate contact between catalyst and carbon PM contributes to better DPF performance [50, 51].

Ceria (CeO_2) has been shown to be a good candidate for DPF-CC catalyst, as it is naturally abundant, less sensitive to sulfur impurities which poison the catalytic oxidation of carbon PM, and less environmentally toxic during end-of-life recycling [5, 19, 21, 24, 53, 55, 145]. Recently, in order to improve the activity and stability of ceria catalyst, metal cations such as Fe and Mn have been doped into the ceria lattice. These dopants effectively inhibit catalyst sintering and increase active sites, both improving the catalyst durability and activity [5, 26-28, 54]. The oxidation mechanisms of carbon particles using a pure CeO_2 and a Fe/CeO_2 catalyst have been investigated by Liu et.al [22, 29]. For the reaction with pure CeO_2, ceria provides oxygen for carbon oxidation, followed by refilling of environmental oxygen into its crystal accompanied by the redox cycle between Ce^{4+} and Ce^{3+}. As for carbon oxidation with the Fe/CeO_2 catalyst, the redox cycle between Fe^{2+} and Fe^{3+} provides oxygen to oxidize carbon, and the redox of Ce continuously provides oxygen to re-oxidize Fe^{2+}. Although many methods exist to dope metal ions into the ceria catalyst, recently it was found that 10% iron doping into a spongy ceria catalyst, prepared through combustion synthesis, produces the best results in terms of carbon oxidation rate and reduced oxidation temperature [146].

During the catalyzed oxidation of carbon particles by the ceria catalyst, the mobility of these particles were found to affect the reaction rate [21, 147]. Environmental transmission electron

microscopy (ETEM) is a promising technology for revealing the interaction between nano-sized carbon and catalyst particles during reaction, by allowing the observation of particle shape changes and motions in a controlled temperature and gas pressure atmosphere [115, 116, 148, 149]. Sediako et al. used ETEM to observe mature and less mature soot oxidation in real time. It was found that mature soot was oxidized on its surface, while the less mature soot showed internal oxidation [115]. Kamatani et al. utilized *in situ* Transmission Electron Microscopy (TEM) to visualize the catalytic soot oxidation using Ag/SiO_2 and Cs_2CO_3 under 300°C with 0.5Pa O_2 [116]. They observed the catalytic reaction happened at the soot-catalyst interface with mobile Ag species and immobile Cs based catalyst. The mobility of Ag/SiO_2 catalyst is considered as a result of heat released from carbon oxidation and partial liquefaction of Ag surface, while the fixed Cs_2CO_3 was due to strong interaction with the substrate. Gao et al. applied ETEM to investigate Ag catalyst on alumina and sulphated alumina supports for soot oxidation. Sulphated alumina was able to anchor the Ag catalyst thus making carbon particles move towards Ag species [117]. Baker et al. used a controlled atmosphere electron microscope (CAEM) to investigate the catalyst (2-5nm) behavior during the gasification of carbon and graphite particles (original in 1μm, 2-20nm after treatment) [118, 119]. They proposed the concept of channeling catalysis, during which the reaction begins at the catalyst/graphite interface and proceeds through channels generated within the graphite crystal. Simonsen et al. studied the oxidation of carbon black (30nm) using CeO_2 catalyst agglomerate (50-100nm) and observed that these carbon particles moved to reach CeO_2, followed by the catalytic combustion at the carbon/catalyst interface [21]. Another study by Mori et al. reported the similar motion of carbon black particles (around 10-20nm) towards an aggregated catalyst cluster made of Ag/CeO_2 and $Cu/BaO/La_2O_3$ cluster (around 200-300nm) [17]. Others reported the motion of carbon particles of around 20nm that were approaching an agglomerate of yttria-

stabilized zirconia catalysts during the catalytic oxidation [120]. Interestingly there has been no report in the literature on observing the nano-sized ceria based catalyst moving towards the carbon particles, which could provide insight on particle-particle interaction and subsequently the reaction mechanism of catalyzed oxidation of particulate matters.

In this work, the research focus is on the visualization and analysis of relative movement and interaction between carbon black nanoparticles and Fe/CeO_2 catalyst nanoparticles, using the commercial CeO_2 catalyst as a reference. This is the first report of the movement of Fe/CeO_2 catalyst nanoparticles towards carbon nanoparticles under the extremely low pressure of oxygen (< 1Pa) within an ETEM. The motion of the nanoparticles is analyzed using the catalyst activity and Density Functional Theory (DFT) modeling.

4.3. Experimental procedures

4.3.1. Catalyst manufacturing

The catalyst was an iron doped cerium oxide compound, prepared by solution combustion synthesis (SCS) method. A stoichiometric solution of iron nitrate nonahydrate (Sigma-Aldrich, CAS: 7782-61-8, 99.95% trace metals basis), cerium nitrate hexahydrate (Sigma-Aldrich, CAS: 10294-41-4, 99.999% trace metals basis) and glycine (Sigma-Aldrich, CAS: 56-40-6) was stirred for 1 day under vigorous agitation to form the precursor, which was then combusted and calcined at 500^0C for 5 h in air. This catalyst was labeled as $10\%Fe/CeO_2$ with a specific surface area of 22.5 m^2g^{-1}. After grinding, the catalyst was particles with around 20 nanometers. Commercial CeO_2 catalyst (Sigma-Aldrich, CAS: 1306-38-3, particle size < 50 nm) were also used as a comparison.

4.3.2. ETEM experiments

The ETEM experiments were conducted by using a Hitachi HF3300 ETEM equipped with Energy-dispersive X-ray spectroscopy (EDX), gas injection and sample heating. In-situ observation videos with spatial resolution of 0.2nm can be recorded under desired temperature and gas atmosphere, particularly 500°C or 800°C, and 1Pa or 0.2Pa O_2. Time-lapsed ETEM videos were obtained in situ of carbon nanoparticles in contact with catalyst as well as control experiments with only carbon nanoparticles.

Printex-U carbon black powder with an average particle size of 25nm was used as a model of carbon nanoparticles, which is common for research on carbon PM oxidation [29, 120, 150]. The catalyst used was a 10% iron doped ceria catalyst (10%Fe/CeO_2) with a size around 20 nanometers after grinding for 10 minutes, synthesized by means of the solution combustion method [151]. The crystal structure and morphology of the catalyst were investigated by German Bruker D4 (40kV, 30mA, CuKα radiation) X-ray Diffraction (XRD) and Scanning Electron Microscopy (SEM, Zeiss MERLIN with Gemini-II column). Carbon and catalyst were mixed by grinding in a weight ratio of 1:9 [38]. The mixtures were then drop coated onto microelectrical mechanical system (MEMS) substrates (Norcada Inc. Model: HTN-010). The distribution of the catalyst and carbon particles on the substrate before and after the reaction was measured by EDX elemental mapping.

To enhance the contrast and increase the resolution, all imaging was done at 300 kV. Sensitivity tests were also carried out to ensure that the observed particle movement were not induced by the electron beam, the gas flow, or the sample/substrate interactions ([115] and Appendix). All tests were conducted according to the procedures established by a previous study as follows [115]: 1) Adjusted beam with sample within high vacuum; 2) Sample pre-heated to 400°C and then inserted

into the beam path. 3) Particles selected, focused and recorded; 4) Temperature raised to experiment temperature at 5°C/s; 5) O_2 or dry air injection started; 6) Conditions maintained until the reaction completes; 7) Gas off / cool down.

For computational method, the DFT calculations (which is completed by Dr. Jingde Li) were carried out using the VASP package[152, 153]. The Perdew-Burke-Ernzerhof (PBE) functional was used for the exchange and correlation energy terms. The CeO_2 and carbon were modeled using a Ce_3FeO_8 cluster and a two-layer 6×6 graphene supercell, respectively. To be more specific, three graphene supercells with no carbon defects, six carbon defects (6-C) and eighteen carbon (18-C) defects were considered to model the realistic chemical states of the carbon materials during the reaction. The calculations performed on this study were spin-unrestricted, and all the atoms were set free to relax. The vacuum height is set to 15Å. The planewave cutoff was set to 400 eV. The k-space was sampled using a 2×2×1 Monkhorst–Pack grid. Structures are fully relaxed until the forces acting on the atoms are smaller than 0.03 eV/Å. Based on the fully relaxed structures, the cohesive energies (E_{coh}) of Ce_3FeO_8 cluster on the graphene (G) supercells were calculated by the following equation:

$$E_{coh} = E_{\mathrm{Ce3FeO8-}G} - E_{\mathrm{Ce3FeO8}} - E_G \qquad (4-1)$$

where $E_{\mathrm{Ce3FeO8-}G}$ represents the total energy of the Ce_3FeO_8 cluster to the graphene structure, E_{Ce3FeO8} is the energy of an isolated Ce_3FeO_8 cluster, E_G represents the energy of the optimized graphene model before bonding to Ce_3FeO_8. The more negative E_{coh} corresponds to a stronger bonding system.

4.4. Results and discussions

4.4.1 Characterization of catalyst and carbon nanoparticles

The XRD pattern of the 10%Fe/CeO_2 catalyst is depicted in Figure 4.1 (A). The diffraction lines match the pattern of pure CeO_2 with a cubic fluorite structure (Fm3m, JCPDS 34-0394), while no peak of any Fe_2O_3 crystal was found, suggesting that iron incorporation into the CeO_2 crystal lattice does not change the hosting crystalline structure. An SEM image of the catalyst is shown in Figure 4.1 (B). It shows the 10%Fe/CeO_2 catalyst has a spongy/porous structure, which may enhance the contact to carbon nanoparticles and can facilitate diffusion of oxygen species to the carbon/catalyst interface.

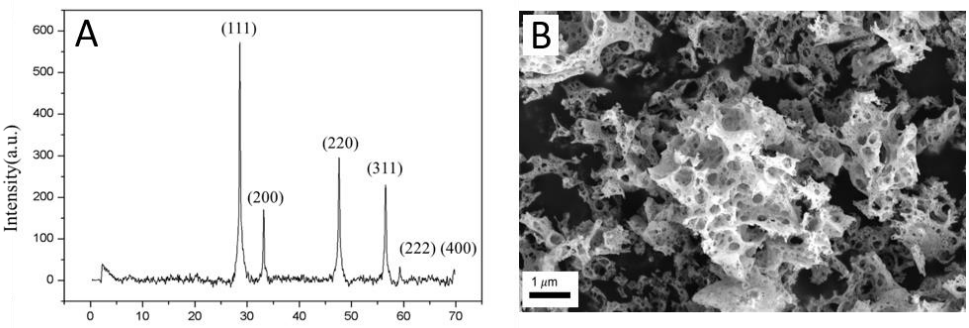

Figure 4.1 XRD pattern and SEM image of as-produced 10%Fe/CeO_2 catalyst

TEM and EDX elemental mapping results of three elements (C, Fe, Ce) on the as-produced carbon-catalyst mixture are displayed in Figure 4.2. Figure 4.2 (A) is a bright field (BF) TEM image. Figures 4.2 (B), (C) and (D) are higher resolution EDX elemental maps for C, Fe and Ce, respectively, around a catalyst particle. In Figure 4.2 (A), the black feature represents catalyst particles, while the light grey feature represents carbon particles. This figure shows catalyst particles of different sizes, from large ones of over several hundred nanometers, to some about 100

nm, to very small ones under 10 nm. Figures 4.2 (C) and (D) show a zoom around a 100 nm catalyst particle, indicating that Fe is well dispersed on the Ceria support. The observed individual small dots for both Fe and Ce are caused by unavoidable noise due to the high-resolution nature of the measurement.

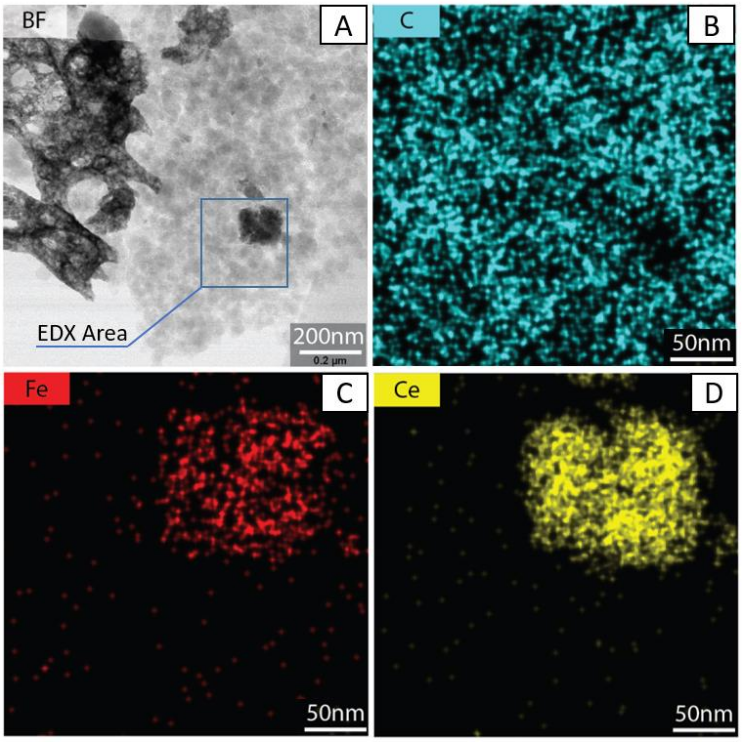

Figure 4.2. (A) TEM image of 10%Fe/CeO_2 catalyst and carbon mixture, (B) EDX image for carbon, (C) EDX image for iron, (D) EDX image for cerium

4.4.2 Mobility and catalytic oxidation in 1 Pa pure O_2 at 500°C

As shown in Figure 4.3, when the catalyst was aggregated into a relatively small size dispersed among carbon, both the catalyst and carbon showed obvious movement during the oxidation in 1 Pa O_2 at 500°C, especially the small clusters of catalysts. Previous studies [21] have shown the movement of carbon towards fixed ceria catalyst. However, this work provides the observation of

the movement and restructuring of the 10%Fe/CeO_2 catalyst. In Figure 4.3 (B) and (D), the processed image of Figure 4.3 (A) and (C), the movement of carbon was indicated by blue arrows and red arrows represented the catalyst movement. During the reaction, the catalysts oxidized the immediate surrounding carbon, and then began to actively travel and consume carbon along the trail of carbon. The interface and morphology of the catalyst cluster was always changing due to the varying configuration of the catalysts and their surrounding carbon, as shown in Figure 4.3 (E). In the meantime, several adjacent catalyst clusters numbered as '4, 5, and 6' in Figure 4.3 (B) tended to agglomerate into one cluster. As the carbon oxidation continued, the sizes/mass of carbon aggregates decreased to be relatively small compared with the catalysts. In this case, the catalyst cluster would stop moving and the surrounding carbon would keep moving towards it to maintain the reaction interface as shown in Figure 4.3 (F), which confirmed that the catalytic carbon oxidation occurred directly at the interface. One special observation was that the catalyst cluster labeled as number '3' in Figure 4.3 (B) moved left together with surrounding carbon aggregation. Catalyst '3' was pulled to left by connected mobile carbon, possibly driven by the cluster of catalyst circled in red in Figure 4.3 (D).

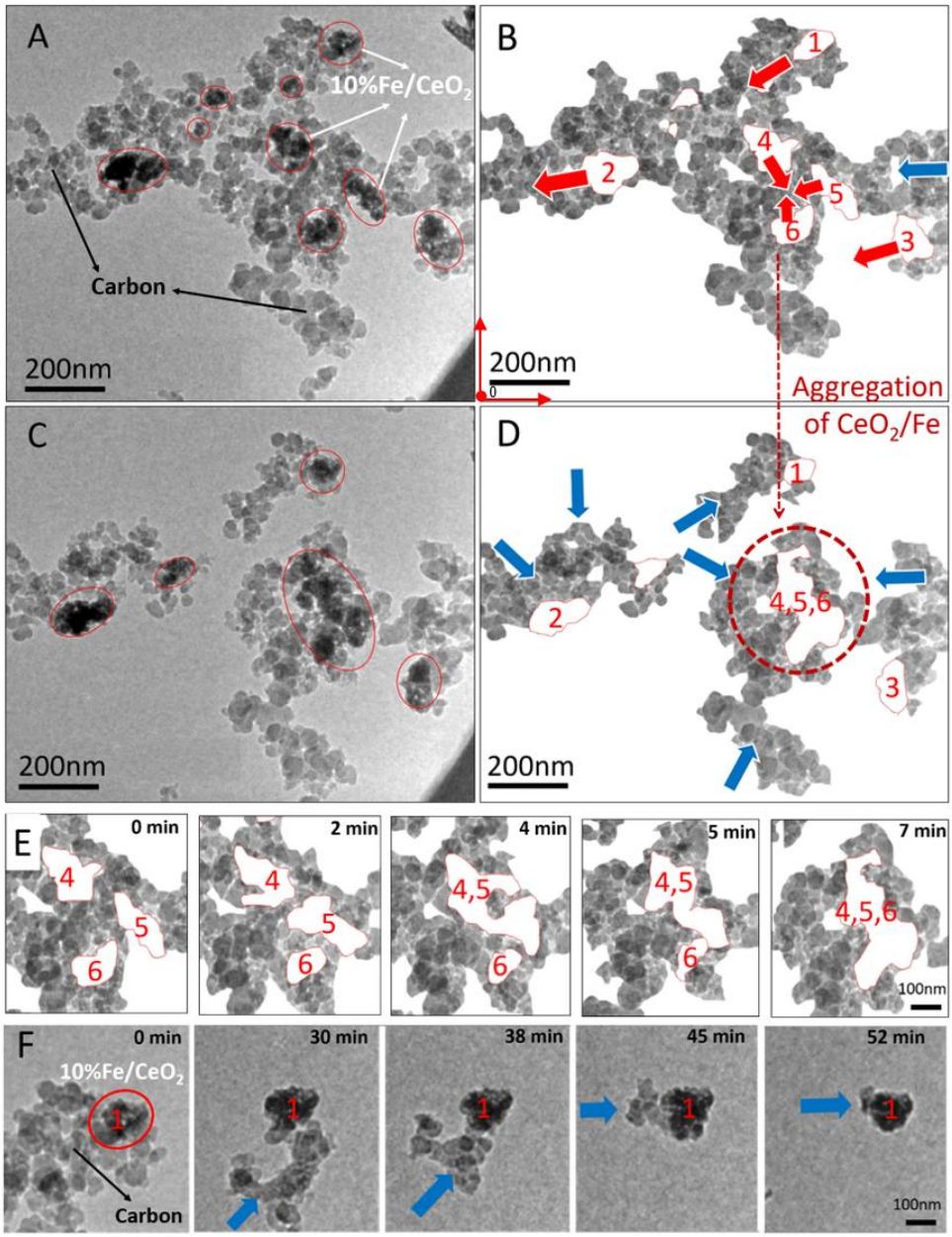

Figure 4.3. ETEM images of carbon and 10%Fe/CeO_2 recorded at 500°C in 1 Pa O_2; A and B – 0min; C and D – 7min; B and D are processed images of A and C, respectively, by cleaning the background, tracing 10%Fe/CeO_2 clusters with a red outline and erasing 10%Fe/CeO_2 to increase the contrast. The movement of carbon and 10%Fe/CeO_2 is marked by blue and red arrows, respectively. E: movement and morphology change of catalysts marked '4, 5, and 6' in B. F: carbon moved towards the fixed catalyst marked '1' in B.

The analysis of the movement of the catalyst and carbon particles was carried out as follows: first the video was divided into several images at different times; at 500°C images were analyzed every one minute, whereas at 800°C images were analyzed every 30 seconds due to faster reaction. Each image was pixelated using ImageJ software who could assign coordinates to all pixels using a common reference origin (red point) as shown in Figure 4.4 (B). For Figure 4.4, the pixel size is 0.83 nm by 0.83 nm. Once the boundary of the particles was determined (manually using Photoshop), the coordinate of its centroid was calculated using ImageJ. The movement velocity of the catalyst clusters labeled as number 1, 2 and 3 in Figure 4.3 (B) was tracked through the coordinate of its center, and the results are shown in Figure 4.4. The velocity was obtained via dividing the displacement distance by the time interval of 1min for a continuous period of 7min and the movement velocity ranged from 0.17 to 0.74 nm/s. From Figure 4.4, it was noticed that the mobility of catalyst was related to the configuration of the catalyst cluster and its surrounding carbon. The varying morphology of the catalyst cluster during carbon oxidation could change its center, and thereby the velocity, obtained by tracing the cluster center, involved not only the movement of the cluster towards carbon but also the shift of the cluster center. Apart from this, the velocity was also influenced by the mobile carbon. For example, the catalyst cluster '3' moved left against carbon, and its velocity was actually that of the surrounding carbon being pulled left by another larger catalyst cluster. Therefore, when the catalysts are dispersed in carbon in a complex configuration, it is reasonable to expect that their velocity will vary over a broad range.

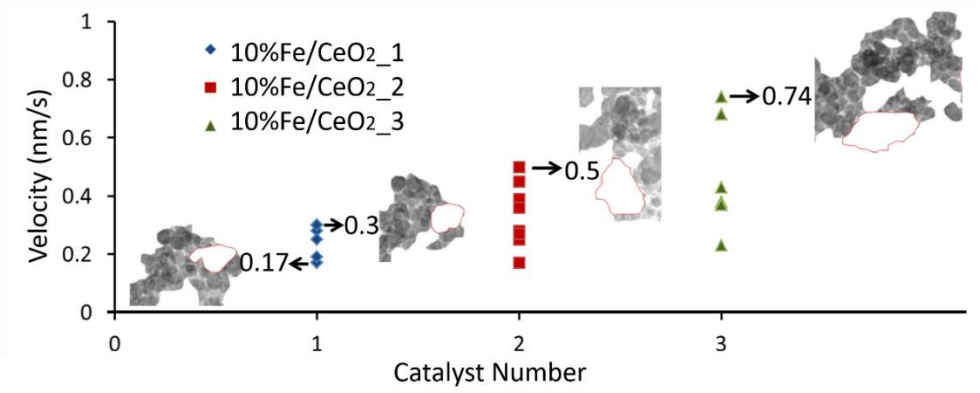

Figure 4.4. The velocity of 10%Fe/CeO_2 clusters labelled as number 1, 2 and 3 in Figure 4.3 (B) and (D). For four values, the configuration of carbon and 10%Fe/CeO_2 nanoparticles is given.

The carbon oxidation rate (r) was estimated by measuring the decrease of the area (A) representing carbon particles at a given time. The methodology to determine the area (A) is described next. As mentioned previously, the contour of the catalyst particles was drawn manually using Photoshop. In a ETEM micrograph (e.g. Figure 4.3), the black particles usually represent the catalyst, but not always, as several carbon particles existing on top of each other and would look dark grey or black. In order to avoid misrepresenting carbon particles as catalyst particles, those dark particles were monitored closely and carefully (if they shrunk or disappeared then it meant that they are carbon particles, otherwise they are considered as catalyst particles. Once all catalyst particles have been identified, they are artificially removed from the ETEM micrograph (e.g. see Figures 4.3 (B) and (D)). The area (A) considered for calculating the reaction rate was the entire surface area left on the ETEM micrograph (i.e. surface area representing carbon particles). The value of the area, A, was calculated using ImageJ. For each time interval, an oxidation rate along with a value of the catalyst velocity were obtained. As the catalytic reaction occurred at the interface and the reaction rate depended on the contact points between the carbon and catalyst, the reaction rates can be normalized (r′) by being divided by the contact length, as shown in equations (4-2) and (4-3).

Related to the movement of carbon and catalysts, the contact length varied from 1435 to 2530 nm and the reaction rate was in the range 115-331 nm^2/s. Figure 4.4 shows the relation between contact length and reaction rate 'r' at 500°C in 1Pa O_2. This figure indicates that the reaction rate increases as the contact length increases.

$$\text{Reaction rate (based on area decrease in a certain time interval)} = \text{r}\left[\frac{\text{nm}^2}{\text{s}}\right] = \frac{dA\ [nm^2]}{dt[s]} \qquad (4-2)$$

$$\text{Normalized reaction rate (per contact length)} = \text{r}'\left[\frac{\text{nm}}{\text{s}}\right] = \frac{r\left[\frac{nm^2}{s}\right]}{\text{contact length } [nm]} \qquad (4-3)$$

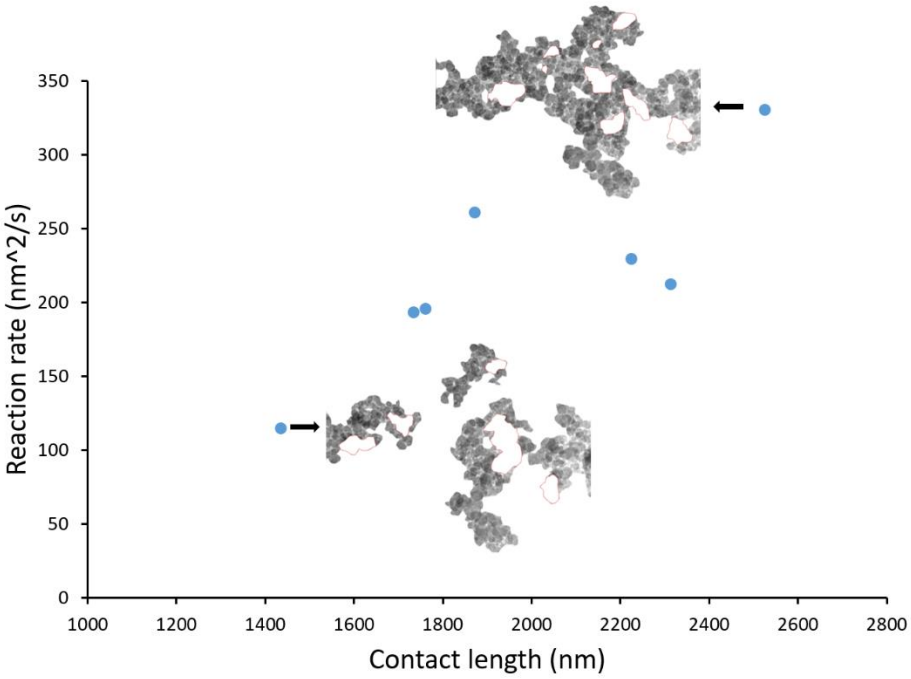

Figure 4.5. Correlation of contact length and reaction rate 'r' at 500°C in 1 Pa O_2

The data in Figure 4.5 were converted into normalized oxidation rate. Note that each of these data points were taken at different time intervals during the course of the reaction. Figure A2 in Appendix gives the normalized reaction rate as a function of time. For the reaction at 500°C (for both O_2 and air), normalized reaction rates are given for more or less the first 500 seconds. It can

be seen that the normalized oxidation rate does not vary much during this time period with an average value of 0.11 ± 0.02 nm/s (uncertainty given as one standard deviation). The catalyst movement velocity was of the same order as the normalized oxidation rate at the interface, which implied that the mobility or the speed is correlated with the normalized reaction rate.

4.4.3 Mobility of catalyst nanoparticles in 1Pa O_2 at 800°C

In order to justify the movement of the catalyst and better correlate the movement of the catalysts to the reaction rate, the same experimental procedure was conducted at 800°C in 1Pa oxygen, as shown in Figure 4.6. The increase in temperature caused the movement of catalyst, as shown by the red arrows, to become more rapid and active. Apart from the same observations in scenario of 1Pa O_2 at 500°C, such as the movement of the catalysts and carbon, one notable phenomenon is that the catalyst aggregated as seen in Figure 4.6 (C) then separated as in Figure 4.6 (D), which is probably because they were pulled by carbon located at their upper right and lower right. It suggests that the catalyst clusters tend to aggregate instead of sintering as the reaction processes, because the sintered catalysts would not split afterwards.

With the movement of the catalysts and carbon, the contact length varied from 116 to 367 nm and the reaction rate was from 64 to 275 nm^2/s. Figure 4.6 (E) also showed that reaction rate has a positive relation with contact length. As seen in Figure A2 in Appendix, the normalized reaction rate at 800°C is given for the first 250 seconds of the reactions; more fluctuations are observed than at 500°C because the reaction is faster. The average value of the normalized reaction rate at 800°C is found to be 0.51 ± 0.08 nm/s. The velocity of the catalysts movement varied from 1.05 to 1.62 nm/s, much higher than that at 500°C. Therefore, the increase of temperature enhanced

both the oxidation rate of carbon and the mobility of the catalysts, that is, the catalysts became more active and more mobile at a higher temperature.

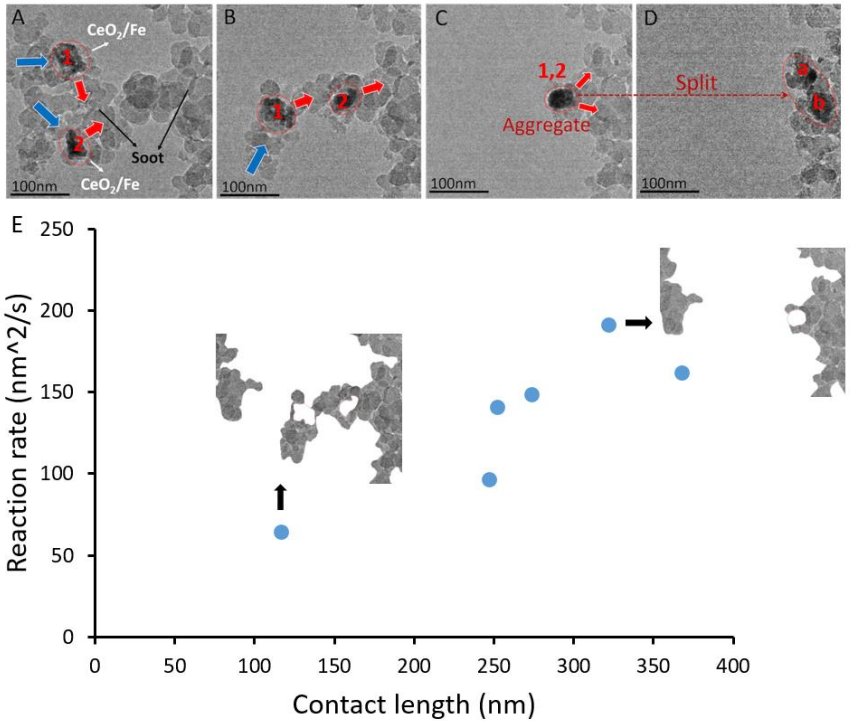

Figure 4.6. ETEM images of carbon and 10%Fe/CeO_2 during the reaction at 800°C in 1Pa O_2; A: 0min; B: 2min; C: 4min; D: 6min. The 10%Fe/CeO_2 catalyst clusters are circled in red lines. E: Correlation of contact length and reaction rate 'r'

4.4.4 Catalytic oxidation in 1Pa dry air at 500°C

To investigate the effects of the partial pressure of oxygen on catalyst mobility and reaction, an in-situ ETEM experiment with 1 Pa dry air (~0.2Pa O_2, compared with 1Pa pure O_2 in section 3.2) at 500°C was carried out. Two representative images are shown in Figure 4.7 (A) and (B). The observed phenomenon was similar as in previous two scenarios, involving the movement of the catalysts and carbon, and the split of the catalyst aggregate. During the reaction, the contact length between the carbon and catalyst varied from 452 to 525 nm and reaction rate ranged from 21.2 to

31.1 nm^2/s. Figure 4.7 (C) shows that with increase of contact length between catalyst and carbon, the corresponding reaction rate 'r' also shows an increasing trend. The measured velocity of catalysts movement was in a range of 0.02 - 0.18 nm/s and the normalized reaction rate was calculated as 0.05 ± 0.01 nm/s. Both the velocity and the activity of the catalysts were lower than those at a higher temperature (800°C) and in a higher O_2 partial pressure (1Pa), indicating that both temperature and oxygen partial pressure have influence on reaction rate and mobility.

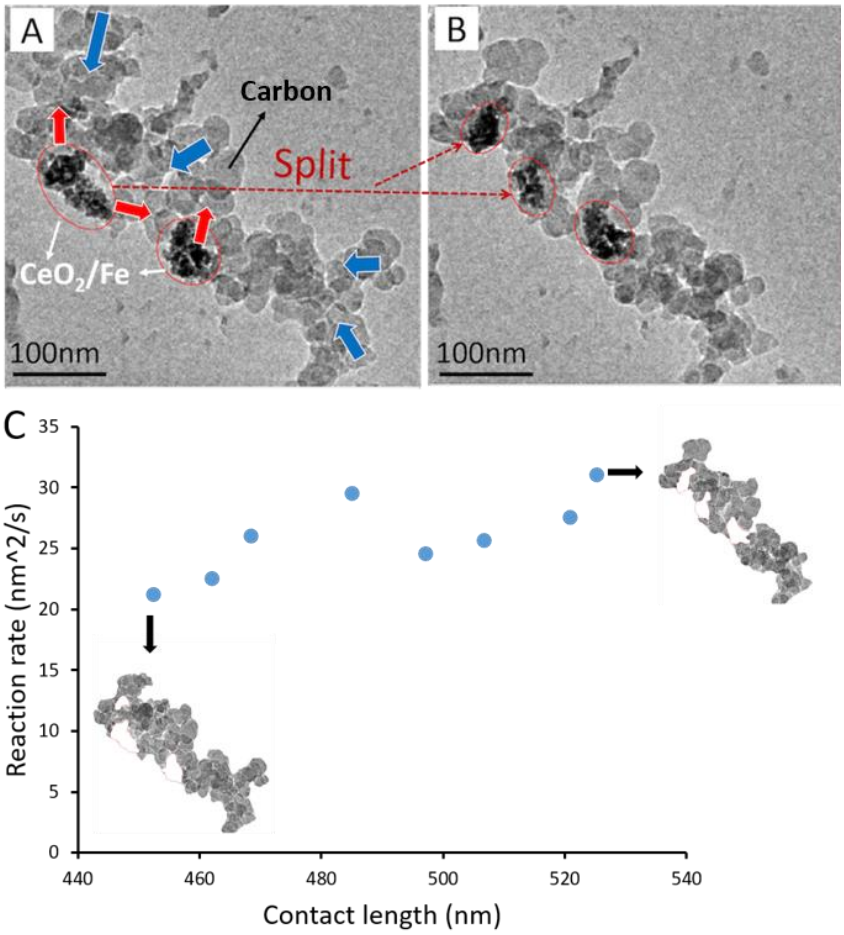

Figure 4.7. ETEM of carbon and 10%Fe/CeO_2 during the reaction at 500°C in 1Pa air (~0.2 Pa O_2); A: 0min; B: 7min. The 10%Fe/CeO_2 catalyst clusters are circled in red lines. The movement of carbon and 10%Fe/CeO_2 is marked by blue and red arrows, respectively. C: Correlation of contact length and reaction rate 'r'.

4.4.5 Mobility of catalyst nanoparticles and affecting factors

a) Dependence on the reaction rate

During the trials, the mobility of the 10%Fe/CeO_2 catalysts towards carbon was found during the catalytic oxidation. As shown in Figure 4.8 (E) and the Appendix, the carbon particles were only consumed and oxidized at the carbon-catalyst interface, rather than on the entire outer surface of the carbon. Kamatani et al. [116] have observed the reaction happened at the interface and found the mobile Ag species during carbon oxidation. The mobility of Ag is due to the liquefaction occurring at the Ag/SiO_2 interface. However, in this study, the reaction temperature is far below the melting temperature of Ce and no visible reaction or movement of nanoparticles was observed in vacuum (Appendix). This demonstrates that the catalyst nanoparticle movement is caused by the catalytic oxidation of carbon. In other words, the mobility of catalyst nanoparticles within this ETEM environment results from the oxidation of carbon, which subsequently re-constructs the carbon /catalyst interface to continue the reaction (possibly through minimizing the surface energy of the reactive interface).

The overview of the normalized reaction rate ‘r′’ and the catalyst movement velocity at different temperatures (500°C and 800°C) and for different O_2 partial pressures is presented in Figure 4.8 (with solid points representing the average value). Overall, it suggests a positive relation between the normalized reaction rate and the mobility of catalyst; with a higher normalized reaction rate, the catalyst mobility is promoted. The normalized reaction rate and corresponding average movement velocity are shown in Table 4.1. The normalized reaction rate and catalyst mobility are sensitive to temperature and to a lesser extend O_2 partial pressure. The comparison between reaction at 500°C in 1 Pa O_2 and air shows that a higher O_2 partial pressure can increase the

normalized reaction rate and hence the catalyst mobility. This is because the O_2 partial pressure can affect oxygen adsorption on the ceria catalyst and diffusion to the reactive sites and thereby affect the oxidation rate [154]. The effect of temperature on catalytic carbon oxidation can be revealed by comparing the reaction in 1 Pa O_2 at 500°C and 800°C. At a higher temperature, both the normalized reaction rate and catalyst mobility can be promoted. This is because an increase in temperature can facilitate the global oxidation process [147, 155]. Since the normalized reaction rate is larger at a higher temperature, it is difficult to accurately measure the catalyst velocity. Considering the influence of these factors such as surface properties of the substrate, the nature and shape of the nanoparticles and the availability of carbon particles along the movement pathway, a largely fluctuating curve was obtained at the high temperature. Nevertheless, both O_2 partial pressures and temperature were found to affect the reaction rate and catalyst mobility.

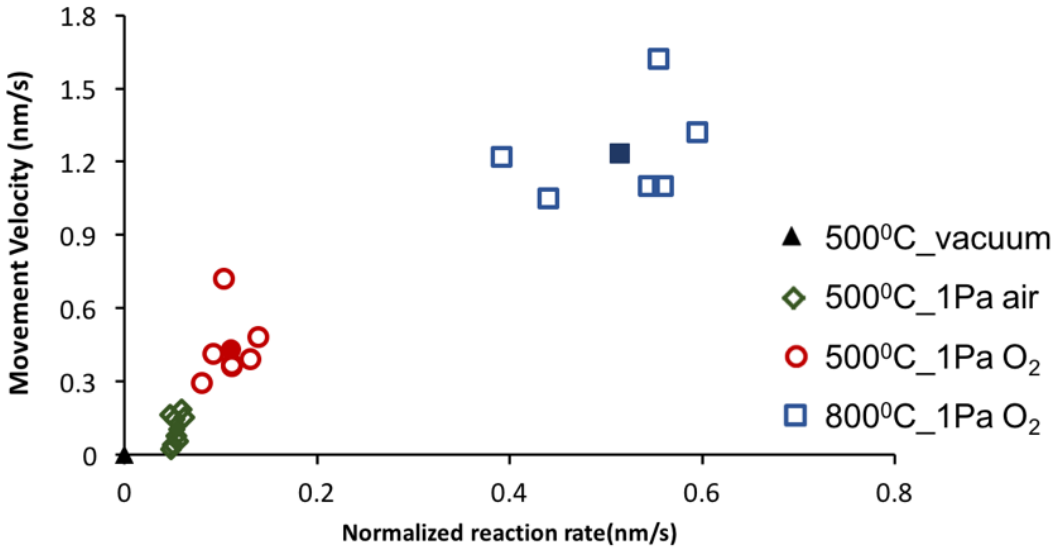

Figure 4.8. Correlation of the normalized reaction rate and the velocity of 10%Fe/CeO_2 catalyst. The symbols with solid fill represent the average values.

Table 4.1. Normalized reaction rate and corresponding movement velocity

	Normalized rate (nm/s)	Movement velocity (nm/s)
500°C, O_2	0.11 ± 0.02	0.43 ± 0.14
800°C, O_2	0.51 ± 0.08	1.24 ± 0.21
500°C, Air	0.05 ± 0.01	0.10 ± 0.06

In comparison of reaction with commercial CeO_2 catalyst (Appendix), where movement of catalyst was barely observed, our 10%Fe/CeO_2 catalyst showed significant movement during the reaction, regardless of temperature and oxygen partial pressure. During the reaction with commercial CeO_2 catalyst, the carbon particles showed movement towards the catalyst similar to a previous investigation [21]. However, only slight mobility of the catalyst was observed, emphasizing that only catalyst with certain properties can move during the reaction. Most importantly, this movement phenomenon could be attributed to the preferable normalized reaction rate of 10%Fe/CeO_2 catalyst for carbon oxidation (avg. 0.12nm/s), compared with normalized rate for CeO_2 (avg. 0.024nm/s). Since the mobility of catalyst results from rebuilding the carbon-catalyst interface in the process of carbon oxidation and is positively correlated with the normalized reaction rate, it is reasonable that the higher normalized reaction rate with 10%Fe/CeO_2 catalyst leads to faster catalyst movement. Moreover, the spongy morphology of 10%Fe/CeO_2 catalyst has a lower density or mass/size, which could have less friction with substrate and become easier to move. And this porous morphology could increase the contact points between carbon and catalyst and facilitate the oxygen diffusion to the catalyst/carbon interface, thus promoting reaction activity and catalyst movement [156]. Furthermore, adding Fe into ceria lattice could also enhance reaction rate due to good redox properties between Fe^{3+} and Fe^{2+} [29]. With Fe incorporated into ceria,

more oxygen vacancies on catalyst surface could be produced to keep the redox cycle continuing and provide more oxygen species for carbon oxidation. Figure 4.2 (A) shows that catalyst particles of different sizes exist, including dispersed catalyst particles under 10 nm. Such dispersed nanoparticles increase the specific contact surface area between the catalyst and carbon particles and possibly increase the overall reaction rate. Therefore, another possible reason for the higher reaction rate for the Fe/CeO_2 catalyst compared to that of the commercial CeO_2 catalyst could be the presence of finely dispersed catalyst particles.

b) Driving forces

The movement of the catalyst and carbon nanoparticles can be explained by these forces among the nanoparticles including liquid bridging, electrostatic forces, thermophoresis, van der Waal forces and chemical bonding [157-159]. Liquid bridging is not considered as a driving force in reactions at 500°C or 800°C, as the mobility occurs during the high temperature reaction, which drives off any potential liquids. As for electrostatic or Coulombic forces, there is a known charging resulting from the high energy electron beam used by the TEM. This electron charging results in a negative charge in all particles, however, and repels the particles apart. Likewise, thermophoresis would also drive the particles apart - due to the exothermic oxidation reaction releasing hot products around the reaction zone, compared to the cold oxygen atmosphere elsewhere.

Despite all these repulsive or neutral forces, the catalysts and carbon move towards each other during the reaction, and actively react. Another possible source of electrostatic force is the transient states of catalysts during the catalysis. There are formations of oxygen vacancies, transformation of Ce^{4+}/Ce^{3+} and Fe^{3+}/Fe^{2+}, and formation of O_2^{2-}/O^{2-} [103], probably resulting in local charge unbalance in the reaction interface of catalysts. But this electrostatic interaction was deemed too

minimal to be the driving force, as the locally charged area is too small, the particle itself remains electroneutral, and no charged species were detected on carbon during the reaction in a previous study [24]. This leaves the possible driving forces as Van der Waals forces and chemical bonding, as they are related to the chemical nature of materials and always exist [157].

c) DFT modeling on particle-particle interactions

Chemical bonding is also considered to drive the movement of catalyst towards carbon particles. Figure 4.9 show the DFT results (calculated by Dr. Jingde Li) from modeling the interactions between Fe/CeO_2 and carbon particles. For Ce_3FeO_8 on perfect (or defect-free) graphene, no apparent bonding between the Ce_3FeO_8 cluster and surface C atoms was observed (Figure 4.9 A). It has a cohesive energy E_{coh} of -0.97eV. However, when Ce_3FeO_8 interacts with the defect graphene edges, the O atoms in Ce_3FeO_8 forms covalent bonds with the defect C atoms (Figure 4.9 B and C). The cohesive energies E_{coh} are -12.08eV and -15.91eV for 6-C and 18-C defect graphene, respectively. These results suggest that the *in-situ* movement of the Fe/CeO_2 nanoparticles might have resulted from the strong O-C bonding between CeO_2 and the defective edge C in the carbon material during their continuous reaction.

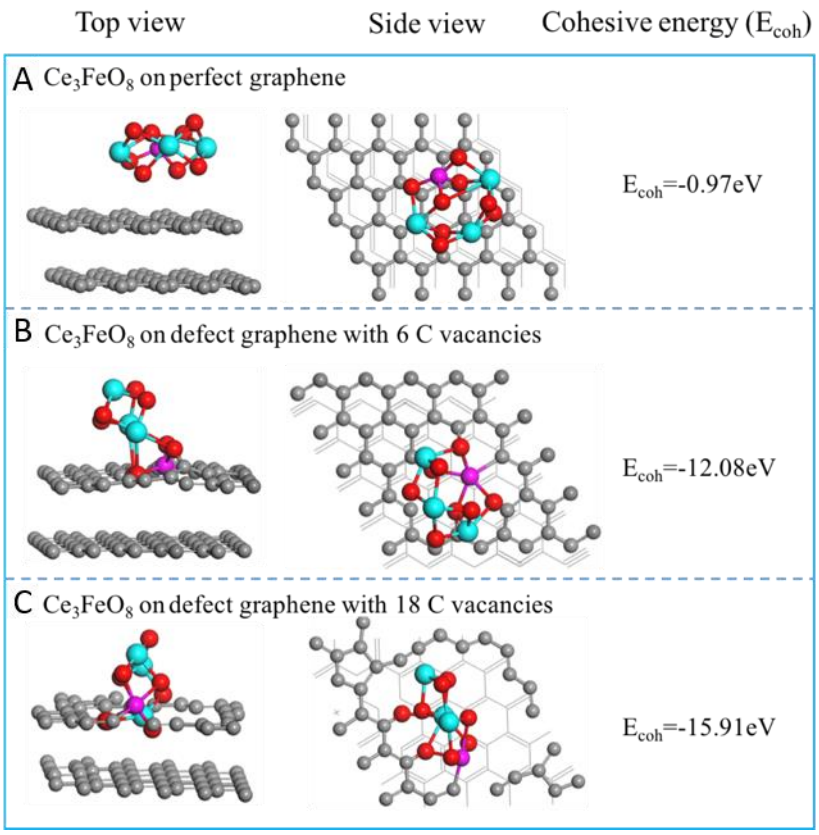

Figure 4.9. The most stable geometric structures (side and top views) of the adsorbed Ce_3FeO_8 cluster, and their corresponding cohesive energies (E_{coh}, eV) on: a) perfect; b) 6-C defects and c) 18-C defects graphene models. Cyan (Ce), red (O), gray (C).

4.5. Summary

In this work, the performance of a 10%Fe/CeO_2 catalyst towards carbon oxidation was investigated by observing in-situ the catalytic oxidation using ETEM. A semi-quantitative analysis was carried out to quantify the mobility of the particles and relate it to the catalyst activity. DFT calculations complemented this analysis to clarify the catalyst-carbon interactions. The main conclusions of this study are as follows:

- Both catalyst and carbon particles can be mobile. Typically, small catalyst agglomerates (50-100 nm) first move through nearly immobile carbon particles. As the amount of carbon decreases, these catalyst particles then slow down and eventually become immobile while mobile carbon particles move towards the catalyst. This relative mobility of the carbon and catalyst particles appears to be correlated to the size of those particles.

- Using 2D ETEM videos, reaction rates were calculated and found to be positively correlated to the contact length between carbon and catalyst particles, thus indicating that the catalytic carbon oxidation occurs at the carbon/catalyst interface.

- Normalized reaction rates (reaction rate divided by contact length) and corresponding movement velocities for reaction conditions of 500°C in O_2, 800°C in O_2, and 500°C in air were found to be 0.11 ± 0.02 and 0.43 ± 0.14, 0.51 ± 0.08 and 1.24 ± 0.21, 0.05 ± 0.01 and 0.10 ± 0.06 nm/s, respectively. These data show that larger normalized reaction rates lead to higher movement velocity, suggesting that the mobility is caused by carbon oxidation on the catalyst's surface. These data also show that both normalized rate and movement velocity increase when the temperature and the oxygen partial pressure increase.

- DFT analysis revealed that there is a strong O-C bonding (12-16 eV) during the catalytic carbon oxidation process. This O-C bonding is likely an important contributor to the strong interactions between the Fe/CeO_2 catalyst and carbon particles during the oxidation reactions, thereby driving the relative mobility of catalyst and carbon particles.

Chapter 5: Reactive Fe-O-Ce Sites in Ceria Catalysts for Soot Oxidation

5.1. Overview

In this chapter, a series of Fe doped ceria catalysts with various Fe doping ratio and different morphologies were prepared and investigated. The Fe content was varied between 0 and 30% for two catalyst preparation methods, co-precipitation (CP) and solution combustion synthesis (SCS). The role of oxygen vacancy on Fe-doped CeO_2 catalyst activity were investigated for soot oxidation. The oxygen vacancy was assessed through Ce^{3+} content. X-ray photoelectron spectroscopy indicates that ceria exists as both Ce^{4+} and Ce^{3+}, while iron is present only as Fe^{3+}. The catalyst's activity was evaluated by ignition (T10) and combustion (T50) temperatures using thermogravimetric analysis. Optimum Fe contents yielding the highest activity were found to be 10% and 5% for CP and SCS catalysts, respectively. The surface area and morphology have shown moderate effect on catalyst activity, because catalytic soot oxidation involves solid-solid contact. More importantly, regardless of the fabrication method, it was found that Ce^{3+} content, which is closely related to oxygen vacancies, plays the most important role in affecting the catalyst activity.

5.2. Introduction

PM (consisting primarily of soot) can cause serious environmental and health problems, such as lung cancer [4, 5, 103]. PM emission can be controlled through processing the exhaust gas through a diesel particulate filters (DPF). DPF with a monolithic geometry have been used to capture and oxidize fine carbon particles [8]. The desired temperature of soot combustion is above 600°C, but

the temperature of exhaust gas is around 200-500°C [9, 10, 13]. It is necessary to introduce catalysts to effectively decrease the soot oxidation temperature and improve the reactor efficiency. Usually, the catalyst is coated on the monolith wall of the DPF [7-14]. After a period of soot deposition, a pressure drop may occur through the DPF, making it necessary to regenerate the DPF periodically [14].

The desired catalysts for soot oxidation should have high activity and suitable stability but low cost, which makes ceria-based catalyst particularly attractive [22]. Ceria-based catalysts have been applied on DPF to study their catalytic activity for soot oxidation [22, 160, 161]. Ceria has been found to act as an active oxygen producer to promote the formation of reactive oxygen species and transfer them to soot-catalyst interface to oxidize soot, which is described in the active oxygen-assisted oxidation mechanism [22, 25]. The oxygen species can be transferred between the oxidized state Ce^{4+} and reduced state Ce^{3+} [4, 5, 29, 62, 63], thus forming oxygen vacancies through Ce^{4+} to Ce^{3+} reduction, and absorbing gaseous oxygen via Ce^{3+} to Ce^{4+}.

The activity of ceria-based catalysts can be further improved through doping other metal additives into the ceria lattice, in order to enhance the oxygen storage capability (OSC) and oxygen mobility [22, 63]. Transition metal doping has been reported to produce more active sites over the catalyst surface and promote catalytic soot oxidation [29-32]. Iron, in particular, is prominent because it can improve the catalyst activity due to its good redox ability - the oxygen species can alternate between Fe^{3+} and Fe^{2+} [5, 22, 33]. The mechanism of iron doped ceria catalysts has been investigated by Zhang et al. [29], indicating that the redox cycle of iron played an important role in this reaction. Fe^{3+} can provide its bonded active oxygen to oxidize soot, along with its reduction to Fe^{2+}. Fe^{2+} can then be re-oxidized to Fe^{3+} with the interaction of Ce [22, 29]. The number of

active Fe-O-Ce sites can vary due to different ratios of iron doping, as iron doping can distort the fluorite lattice and create oxygen vacancies to varying degrees. Thus, the ratio of iron doping in ceria affects the catalyst activity and need be optimized with reaction conditions.

As the catalytic soot oxidation is a surface sensitive reaction, the contact points between soot and catalyst particles have a great impact on activity [4]. Nano-sized materials result in a high surface-to-volume ratio and make their chemical and physical properties more size and shape dependent [100, 101, 162]. More specifically, the quantum size effects and higher surface areas make these nanostructured catalysts possess more potential contact points between soot and catalyst particles while their meso-scale pores (with diameters between 2 and 50 nm) can promote the oxygen diffusion through catalysts [100]. In order to enhance the interactions between soot and catalyst, different morphologies of ceria-based catalysts have been fabricated by a number of preparation methods [85, 86, 89, 90, 96, 163, 164]. It is found that different morphologies exhibit distinct catalytic activity, which is strongly dependent on their physical and chemical surface properties [22]. Among these preparation methods, co-precipitation (CP) method has been widely used for catalyst preparation due to the formation of higher surface area and smaller crystal size [29]. Alternatively, solution combustion synthesis (SCS) is a time effective and energy saving method to produce nano-sized porous catalysts [102]. Herein, these two preparation methods have been chosen in this study to investigate the morphologies influence on catalyst activity.

Different iron doping ratios and morphologies would change the surface properties and oxygen vacancies of catalysts, which has influence on catalyst activity [104]. Kattal et al. found that increasing oxygen vacancies induces more active oxygen for CeO_2–La_2O_3 catalyst [27]. Pr, La, Tb doped CeO_2 catalyst were studied for methane steam reforming, revealing that increased oxygen

storage capacity contributes to higher activity [105]. Oxygen vacancy of Ag-doped perovskite catalysts was found to be the primary intermediates for the NO oxidation reaction [106]. Zr doped CeO_2 catalyst showed positive relation between oxygen vacancy concentration and catalyst activity for dimethyl carbonate synthesis [107]. The above-mentioned studies showed a relation between oxygen vacancy and catalyst activity. However, the effect of oxygen vacancy on soot oxidation by altering the catalyst morphologies along with different Fe doping ratios is still poorly understood. Therefore, this study aims at investigating the role of oxygen vacancy on catalyst activity through varying the Fe doping ratio and tailored catalyst morphology.

5.3. Experimental Section

5.3.1 Preparation of the catalysts

Fe_xCe_{100-x}-CP (x = 5; 10; 20; and 30 in percent of molar ratio) catalysts were synthesized by co-precipitation (CP). A stoichiometric solution of iron nitrate nonahydrate (Sigma-Aldrich, CAS: 7782-61-8, 99.95% trace metals basis) and cerium nitrate hexahydrate (Sigma-Aldrich, CAS: 10294-41-4, 99.999% trace metals basis) were dissolved separately in deionized water, then mixed together with vigorous agitation. The aqueous ammonia (Sigma-Aldrich, CAS:1336-21-6, 28%-30% NH3 basis) was then gradually dropped into the above mentioned solution under stirring conditions until pH reached 8.5, after which the solution was aged in air for one day at room temperature with constant stirring. The resultant precipitates were separated by vacuum filtration with three washes with deionized water. The obtained precipitates were dried at 100°C for 12h and then calcined at 500°C for 5h in static air. For comparison, pure cerium oxide - CeO_2 was prepared using a similar procedure.

Fe_xCe_{100-x}-SCS (x = 5; 10; 20; and 30 in percent of molar ratio) catalysts were obtained by solution combustion synthesis (SCS). An aqueous solution of iron nitrate nonahydrate (Sigma-Aldrich, CAS: 7782-61-8, 99.95% trace metals basis), cerium nitrate hexahydrate (Sigma-Aldrich, CAS: 10294-41-4, 99.999% trace metals basis) and glycine (Sigma-Aldrich, CAS: 56-40-6) in a stoichiometric ratio was prepared under vigorous stirring at 90°C to form the gel. Then, the gel was combusted on a heating plate. The combustion procedure is very fast, producing fine powders. The resultant sample was then calcined at 500°C for 5 h. CeO_2-SCS catalyst was developed using a similar procedure.

5.3.2 Characterization of the catalysts

X-ray powder diffraction (XRD) analysis was performed on X-ray powder diffractometer (German Bruker D4 (40 kV, 30 mA), with position-sensitive detector and CuKα radiation). The XRD patterns were recorded in steps of 0.01° with a scanning rate of 5°/min from 5° to 85°. The diffraction peaks were indexed according to the Powder Data File database (PDF 2004, International Centre of Diffraction Data, Pennsylvania).

The surface area was measured by means of N_2 adsorption-desorption isotherms using Beishide 3H-2000PS2 static volumetric method analyzer. The surface area of catalysts were evaluated by Brunauer-Emmett-Teller (BET) method.

The morphologies, microstructures and elemental composition of the obtained catalysts were characterized by a Field-emission scanning electron microscope (FE-SEM, Zeiss MERLIN with Gemini-II column).

X-ray photoelectron spectroscopy (XPS) measurements were carried out on ESCALab220i-XL electron spectrometer (VG Scientific Ltd, UK) with 300 W AlKα X-ray source equipment to investigate the oxidation states of cerium and iron, and availability of oxygen on catalyst surface. The calibration of binding energies was conducted by using C1s peaks at 284.8eV. Spectra-fits were performed with Gaussian-Lorentzian functions by using CasaXPS software.

The Raman spectra of the catalysts were measured on a Renishaw InVia micro laser Raman spectrometer (Renishawplc, Wottonunder-Edge, UK) with a 4mW Ar+ laser source (λex = 532nm) with a cooled CCD detector at room temperature to differentiate chemical structures. The acquisition time was 60s and the scanning range was 100-2000cm^{-1}.

Temperature-programmed reduction with H_2 (H_2-TPR) experiments was carried out to study the reducibility of the catalyst by using a Micromeritics Autochem II 2920 analyzer with a thermal conductivity detector (TCD). 50mg catalyst was first pre-treated at 150°C for 1h under 40ml/min N_2 flow to remove water and other contaminants and then cooled down to room temperature. TPR analysis was conducted by heating up the sample to 700°C at 10°C /min in a flow of 40 ml/min 10% H_2/Ar.

5.3.3. Catalytic activity tests

Thermogravimetric analysis (TGA) of catalytic soot oxidation were conducted on a TA Instrument Q500 apparatus to investigate catalytic activity. Printex-U carbon black, with particulate size of 25 nm and 100 m^2g^{-1} surface area, was used as model of soot. Tight contact condition of mixed sample was obtained by grinding soot and catalyst with a weight ratio of 1:9 in an agate mortar for 10 minutes [29]. For each TGA test, a weighted amount of 10 mg sample was pre-treated at 150°C

under 60 ml/min Nitrogen for 30 min to remove water and other contaminants. Then, the sample was heated up to 800°C under 40 ml/min air with a heating rate of 10°C /min. The thermogravimetric curves were obtained by continuously recording the mass change, along with increased temperature. Each TGA test was repeated three times to ensure the repeatability of the results. The activity of catalyst was evaluated by T10 and T50. T10 is commonly used as the ignition temperature, which is the temperature at 10% conversion of soot [4, 29, 63, 150]. T50 is the combustion temperature, identified as the temperature when 50% of soot is oxidized [4, 5, 63, 150].

5.4. Results and Discussion

5.4.1. Characterization

The crystal structure of all catalysts was studied by XRD. The XRD patterns of iron doped cerium oxide catalysts prepared by SCS and CP methods are depicted in Figure 5.1. The main diffraction peaks could be attributed to (111) (200) (220) (311) (222) (400) (331) (420) planes, referring to a typical face-centered cubic fluorite structure matching the spectra for pure cerium oxide (JCPDS NO. 34-0394) [165]. The characteristic peaks shifted to higher 2θ diffraction angle with iron doping and no peaks of Fe_2O_3 was observed, suggesting the uniform incorporation of iron into cerium oxide lattice and the formation of solid solution, thus the catalyst could be represented by Fe_xCe_{100-x} [5, 27, 33, 166]. The absence of characteristic peaks of iron oxide could also result from the absence of iron oxide on the surface or from crystal being too small to be detected by XRD.

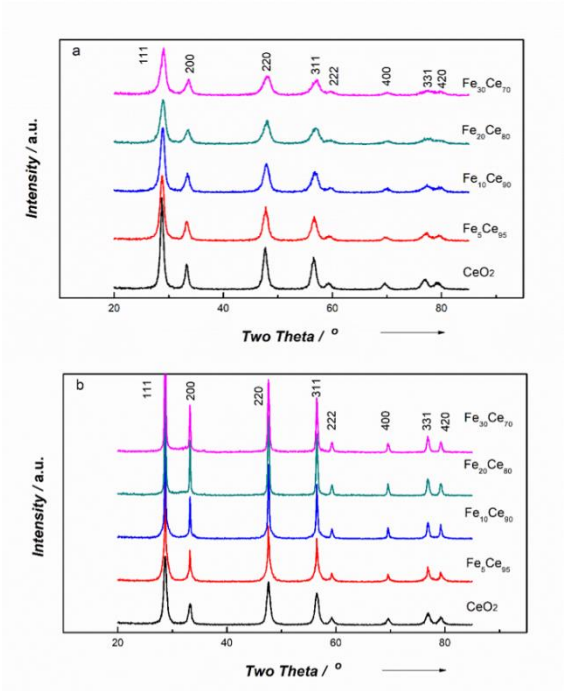

Figure 5.1. Powder X-ray diffraction patterns of (a) Co-precipitation method, (b) Solution combustion synthesis method

The textural properties of catalysts are listed in Table 5.1; the crystal size was calculated by using the Scherrer equation, while the unit lattice parameter was calculated by Bragg's law using the strongest peak (111). From Table 5.1, it is clear that CP catalysts lead to smaller crystal size than for SCS catalysts. In addition, compared to pure ceria, iron doping results in smaller crystal size for CP catalyst, but in much higher crystal size for SCS catalyst. Table 5.1 also shows that the lattice parameter slightly decreases with more iron doping. This is because of the smaller iron atoms (Fe^{3+}-0.64 Å, Fe^{2+}-0.74 Å) substituting larger ceria sites (0.97 Å) in the lattice to form Ce-Fe-O solid solution [33]. These results also indicated the incorporation of iron into ceria lattice.

Table 5.1 Textural properties of as-derived catalysts

Catalyst	Crystal size [nm]	Lattice parameter [Å]	S_{BET} [m^2g^{-1}]	Pore size [nm]
CeO_2-CP	11.71(±0.05)	5.38(±0.0009)	73(±1.41)	2.46(±0.13)
Fe_5Ce_{95}-CP	9.11(±0.08)	5.36(±0.0012)	87(±1.23)	3.48(±0.11)
$Fe_{10}Ce_{90}$-CP	8.63(±0.04)	5.34(±0.0011)	94(±0.97)	3.49(±0.19)
$Fe_{20}Ce_{80}$-CP	7.96(±0.11)	5.33(±0.0025)	87(±2.15)	5.60(±0.25)
$Fe_{30}Ce_{70}$-CP	7.89(±0.09)	5.32(±0.0017)	65(±1.72)	3.51(±0.21)
CeO_2-SCS	13.33(±0.06)	5.39(±0.0013)	38(±0.98)	3.63(±0.09)
Fe_5Ce_{95}-SCS	30.59(±0.05)	5.38(±0.0015)	39(±1.03)	4.61(±0.13)
$Fe_{10}Ce_{90}$-SCS	31.53(±0.13)	5.37(±0.0008)	20(±1.84)	3.66(±0.35)
$Fe_{20}Ce_{80}$-SCS	32.79(±0.07)	5.37(±0.0028)	3(±3.12)	4.56(±0.32)
$Fe_{30}Ce_{70}$-SCS	34.15(±0.06)	5.37(±0.0031)	2(±2.56)	3.82(±0.27)

As shown in Table 5.1, catalysts made by CP method reveal higher surface area than those made by SCS method. $Fe_{10}Ce_{90}$- CP and Fe_5Ce_{95}-SCS yielded the highest specific surface area within their preparation method, and $Fe_{10}Ce_{90}$-CP showed the largest surface area (94 m^2g^{-1}) among all. Accordingly, introduction of iron enlarged the surface area of CP catalyst. For SCS catalysts, only 5% iron doping showed slight increase of surface area compared to pure CeO_2, but other ratio doping led to a surface area decrease. It was also noticed that the surface area greatly dropped with more than 20% of iron doping, especially for SCS method. The pore diameters of both CP and SCS catalysts are around 3-5 nm.

SEM was performed to explore the surface morphologies of catalysts. In Figure 5.2, both pictures clearly show the nanoparticle morphologies: the CP method produced uniform spherical morphology with some agglomeration, while catalyst made by SCS method reported a spongy structure. The spherical morphology for CP method was a result of precipitants' nucleation, and

these small particles yielded higher surface area. The foamy and highly porous spongy structure is a more unpredictable structure made from SCS method, which was due to the combustion procedure- the reacting precursor releasing lots of gaseous products in a short time. Moreover, these bigger openings got from this morphology can be large enough (around 250 nm diameter) for soot particle (typical size around 25 nm) to penetrate, thus creating more contact points between soot and catalyst particles.

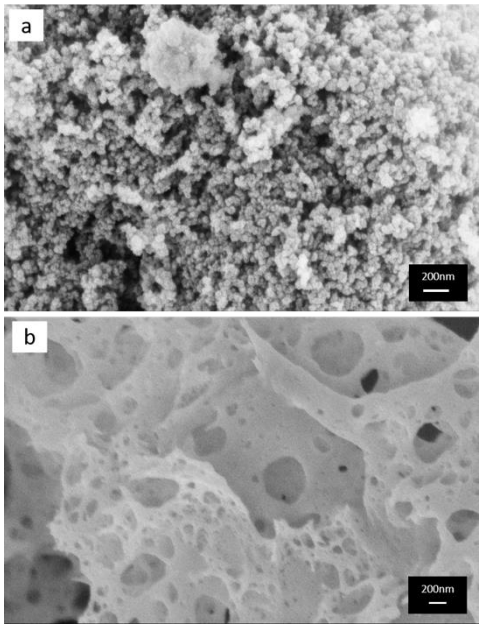

Figure 5.2. FE-SEM images of (a) Co-precipitation method, (b) Solution combustion synthesis method

XPS analysis was undertaken to study the surface properties of catalysts in terms of their oxidation state and surface oxygen vacancies. Figure 5.3 shows the Ce 3d spectra of all catalysts. The Ce 3d spectra could be curve fitted into eight peaks corresponding to the spin-orbit splitting of Ce $3d_{5/2}$ and Ce $3d_{3/2}$, which were labelled as "u" and "v" respectively [167]. The peaks labelled as v0, v2, v3, u0, u2, u3 with binding energy (BE) around 882, 888, 898, 900, 907, 916 eV correspond to the Ce^{4+} species and peaks labelled as v1, u1 with binding energy of 884 and 902 eV are ascribed to Ce^{3+} species. The analysis of XPS spectra suggested that Ceria existed as both Ce^{3+} and Ce^{4+}, but

primarily in Ce^{4+} state. When Ce^{4+} transferred to Ce^{3+}, an oxygen vacancies associated with Ce^{3+} could be generated to potentially absorb oxygen and provide it for soot oxidation. Therefore, the existence of Ce^{3+} becomes important to indicate the generation of oxygen vacancies [5, 33]. The calculations of integrated peak areas were used to get a quantitative analysis of a selected element. In this way, the ratio of Ce^{3+} area to total area including Ce^{3+} and Ce^{4+} was applied to estimate the ratio of Ce^{3+}; the result are given in Figure 5.3. From Table 5.2, all Ce^{3+} percentage are around 20%, CP catalysts are between 19% - 25%, and SCS catalysts are between 17% - 27%. Ce^{3+} content has the similar trend for both CP and SCS catalysts, which is Ce^{3+} goes up to a maximum value then goes down. The maximum Ce^{3+} value for CP catalysts is 24.9% with 10% iron doping, and is 27.1% with 5% iron doping for SCS catalysts. Among all catalysts, Fe_5Ce_{95}-SCS gives the highest Ce^{3+} percentage, higher than $Fe_{10}Ce_{90}$-CP. Therefore, it can be deducted that Fe_5Ce_{95}-SCS has the highest concentration of oxygen vacancies.

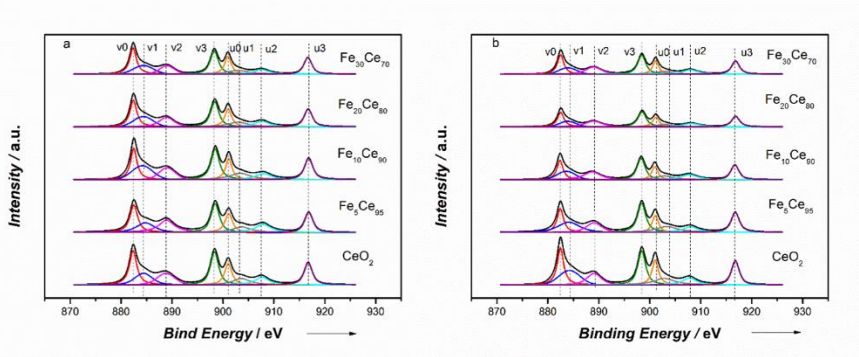

Figure 5.3. XPS spectra of Ce3d (a) Co-precipitation method, (b) Solution combustion synthesis method

The Fe 2p spectra in Figure 5.4 showed the characteristic Fe $2p_{3/2}$ and Fe $2p_{3/1}$ peaks at binding energy of 711 and 724 eV, respectively. Two satellites peaks at 718 and 733 eV were slightly distinguished. These peaks indicated the existence of Fe^{3+}. The binding energy of Fe 2p decreased

with more iron doping, further confirming that Fe^{3+} incorporated into CeO_2 lattice and formed a solid solution, as shown by XRD results.

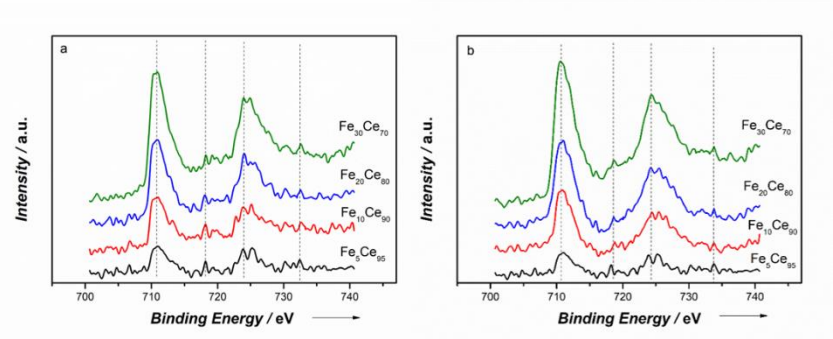

Figure 5.4. XPS spectra of Fe2p (a) Co-precipitation method, (b) Solution combustion synthesis method

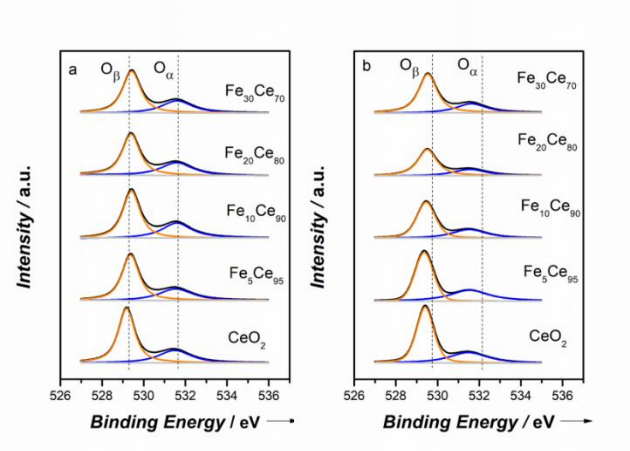

Figure 5.5. XPS spectra of O1s (a) Co-precipitation method, (b) Solution combustion synthesis method

The O1s spectra showed two distinct peaks in Figure 5.5. The peak at higher binding energy (~531.7 eV) referred to the surface oxygen species O_α, and the peak at lower binding energy (~529.5 eV) is attributed to the lattice oxygen O_β [89]. As Fe is added into CeO_2, the main peak O_β shifted to higher binding energy, suggesting the chemical environment of lattice oxygen changed due to incorporation of Fe [168]. The surface oxygen species O_α are critical for soot oxidation because they can become active and react with soot particles. The ratio of surface oxygen

concentration to lattice oxygen concentration can be estimated by the integrated peak areas of O_α and O_β, and the results are shown in Table 5.2. For CP method, O_α percentage - $O_\alpha/(O_\alpha+O_\beta)$ increased to a maximum point (60%) at 10% iron doping, and then decreased. SCS catalysts showed similar behavior, where it reached a maximum value (64%) at 5% iron doping ratio. Among all, Fe_5Ce_{95} –SCS led to the highest surface oxygen concentration. These results agree well with concentration percentage of Ce^{3+}.

Table 5.2. Curve fitting results of Ce3d and O1s on obtained catalysts

Catalyst	Preparation method	Ce^{3+} content [%]	O_α content [%]	I_{596}/I_{463}
CeO_2	CP	20.1	31.5	0.023
	SCS	24.5	33.3	0.028
Fe_5Ce_{95}	CP	19.7	32.8	0.037
	SCS	27.1	39.0	0.032
$Fe_{10}Ce_{90}$	CP	24.9	37.5	0.029
	SCS	20.4	33.8	0.029
$Fe_{20}Ce_{80}$	CP	21.4	35.5	0.028
	SCS	17.1	29.1	0.021
$Fe_{30}Ce_{70}$	CP	20.5	33.3	0.013
	SCS	16.9	28.1	0.011

The Raman spectroscopy was conducted to study the oxygen vacancies and active sites within the catalysts. Figure 5.6 shows the Raman spectra of Fe_xCe_{100-x} catalysts made by CP and SCS methods. The prominent band at ~463cm^{-1} could be assigned to the first order scattering F2g symmetric oxygen active mode around Ce^{4+} with a CeO_2 fluorite structure [54], which is in agreement with the XRD and XPS results. All catalysts spectra are identical to that of pure CeO_2, further indicating that iron has been incorporated into the CeO_2 lattice. Compared to the Raman spectra of pure CeO_2, the F2g band shifted to lower frequency and broadened with an increase in

iron doping, suggesting the lattice distortion due to the incorporation of iron into CeO_2 fluorite lattice [96]. The intensity (I) of Raman spectra decreased with increasing iron doping, indicating the structure change due to Fe incorporation and lower ceria content [33]. No peaks of Fe_2O_3 were observed, which is possible due to the much weaker bands of Fe_2O_3 than CeO_2 and the formation of solid solution. Two weak bands at ~261 and 596 cm^{-1} were characteristic bands of second order scattering, which can represent the oxygen vacancies in the lattice [29]. The low intensity of oxygen vacancies showed in Raman spectra was because the sample was not outgassed, the intensity would be higher if the sample was outgassed at high temperature [166].

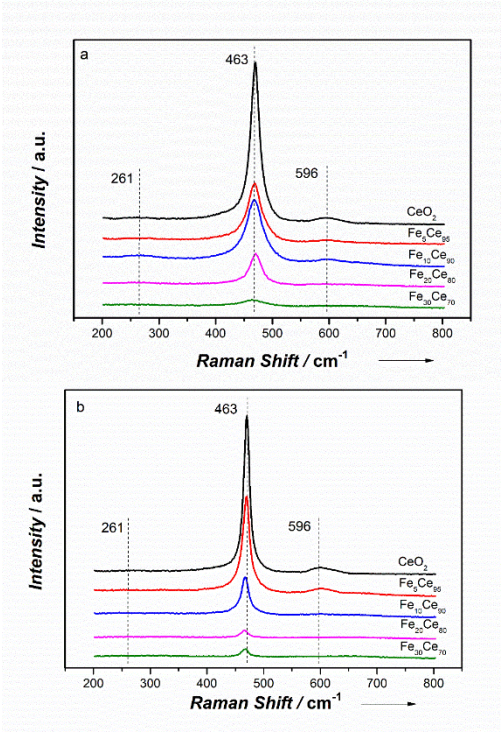

Figure 5.6. Raman spectra of (a) Co-precipitation method, (b) Solution combustion synthesis method

The 596 cm^{-1} band exhibits the oxygen vacancies caused by Ce^{3+}, thus the value of I_{596}/I_{463} (as shown in Table 5.2) becomes important to evaluate the oxygen vacancies or amount of defects in the catalysts. Catalysts made by the two methods (CP and SCS) showed similar trend of

I_{596}/I_{463} with increasing iron content, that is rise first to reach a maximum and then drop down. This is because Fe prefers to occupy Ce sites in CeO_2, thus the oxygen vacancy concentration increases with more Fe doping. But when the amount of Fe exceeded a critical value, Fe turned into interstitial in CeO_2 lattice, thus decreasing oxygen vacancy concentration [169]. The results showed that $Fe_{10}Ce_{90}$-CP and Fe_5Ce_{95}-SCS reached optimum I_{596}/I_{463} value within their preparation method. Fe_5Ce_{95}-SCS obtained the maximum I_{596}/I_{463} value, indicating highest oxygen vacancies.

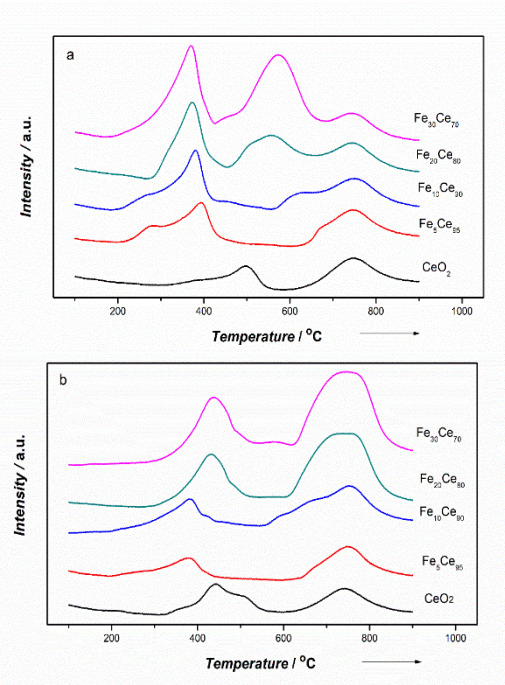

Figure 5.7. H_2-TPR results of (a) Co-precipitation method, (b) Solution combustion synthesis method

H_2-TPR was applied to investigate catalysts' reducibility. As shown in Figure 5.7, pure CeO_2 had two main H_2 consumption peaks. The peak at lower temperature (500°C for CP and 440°C for SCS) corresponded to reduction of surface oxygen of ceria, and the other peak at higher temperature (~750°C) is attributed to reduction of bulk oxygen of ceria. Pure CeO_2 made by SCS method had a better reducibility than that prepared by CP method. For Fe-doped ceria CP catalysts,

the reduction peak of surface oxygen shifted towards lower temperature with increase of Fe doping, indicating that the Ce-O bond weakened and the mobility of surface oxygen improved. For SCS catalysts, the peaks of surface oxygen reduction shifted to lower temperature with 5% and 10% Fe doping (378°C and 384°C, respectively). But when the doping ratio was higher than 20%, the peak shifted to higher temperature and remained similar to pure CeO_2, meaning that reducibility can only be improved by low Fe doping (<10%). Additionally, these peaks of surface oxygen reduction for both CP and SCS catalysts were broader and with higher intensity as more Fe is incorporated.

However, the temperature of bulk oxygen reduction remained almost unchanged for CP and SCS catalysts. This is because lattice oxygen needed to be transferred to the surface before being reduced, and adding Fe did not change the reducibility of bulk oxygen. . It is noticed that the peaks of SCS bulk oxygen reduction became higher and broader when increasing Fe doping, suggesting that more releasable lattice oxygen could be transferred to surface oxygen [22]. For $Fe_{20}Ce_{80}$-CP and $Fe_{30}Ce_{70}$-CP, an additional peak around 550°C was observed, which could be attributed to reduction of iron oxide species. According to the literature, Fe_2O_3 normally showed two steps reduction: Fe_2O_3 to Fe_3O_4 around 385-425°C and Fe_3O_4 to Fe at 590-745°C, respectively [29]. Hence, the additional peak shown on $Fe_{20}Ce_{80}$-CP and $Fe_{30}Ce_{70}$-CP catalyst could be assigned to the iron oxide reduction. This means that some isolated iron oxide species can exist when Fe doping ratio is above 20%. The reason for XRD not detecting single phase iron oxide was because of the very limited amount of these iron oxide and XRD only detect the surface properties, but iron oxide could be inside the crystal structure. Herein, for higher ratio of iron doping, the CP catalysts had co-existence of solid solution and some iron oxide phase. But for SCS method catalysts, no

reduction peak of iron oxide was observed, which might be due to the absence of iron oxide or not detecting the limited amount of iron oxide.

5.4.2. Activity study

TGA experiments were carried out to investigate the catalyst activity for soot oxidation. Tight contact condition was used to study the influence of iron doping ratio and morphology on catalyst activity. The result of soot conversion as a function of temperature is shown in Figure 5.8. Tight contact condition was used to explore the intrinsic activity of the catalysts because soot and catalysts were ground together to produce more contact points [63]. The activity of catalyst is evaluated by the ignition temperature (T10-the temperature at 10% conversion of soot) and combustion temperature (T50-the temperature at 50% conversion of soot). T10 and T50 for tight contact condition are summarized in Table 5.3. For comparison, non-catalytic soot oxidation was also conducted at the same reaction conditions.

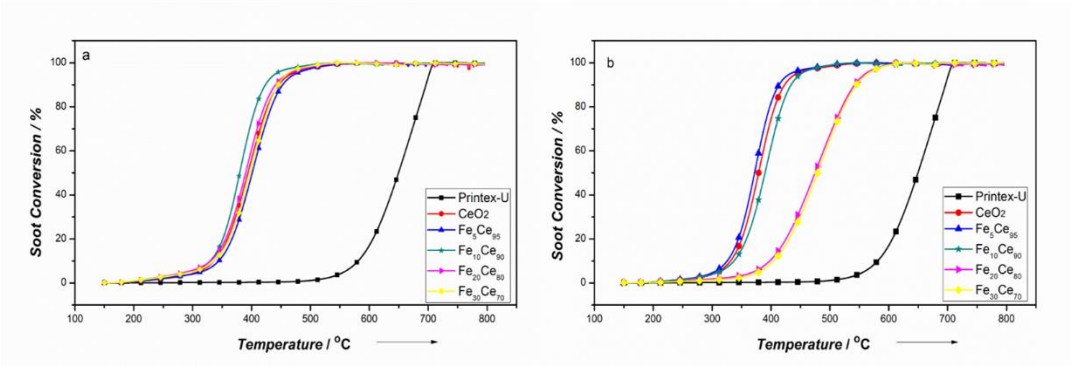

Figure 5.8. Soot conversion of tight contact condition: (a) Co-precipitation method, (b) Solution combustion synthesis method

From Figure 5.8, it is obvious that soot oxidation temperatures decreased significantly when adding catalyst compared to non-catalytic soot oxidation. Different iron doping ratios and morphologies have distinct effects on catalyst activity. CP and SCS catalysts showed similar trend

of T10 and T50 with different iron doping ratio, which decreased first to a threshold then began to increase. The minimum temperature in T10 and T50 for CP catalysts are T10~328°C and T50~378°C with 10% iron doping, and for SCS catalysts, they are T10~324°C and T50~372°C with 5% iron doping. It is noted that when doping ratio exceeded 20% for SCS catalysts, the catalyst activity greatly reduced (decreased by about 70°C). Comparing CP to SCS catalysts, it is interesting to find that SCS catalyst performed better than CP catalyst with low Fe doping (<5%) despite their lower surface area. However, this situation changed when Fe content increased from 10% to 30%, CP catalysts became better performing than SCS catalysts of the same composition. This makes the surface area not the determining factor for catalytic soot oxidation. Although this reaction is surface sensitive, what matters most is the contact between solid soot and catalyst particles, making the available surface for contact points become important. As seen from Table 5.1, the pore size of CP and SCS catalysts are around 3-5 nm, which is too small for soot particles (around 25 nm) to go through. Although SCS catalysts had a spongy structure with lower surface area, many openings (~250 nm) resulted from the combustion process could easily let soot particles penetrate in to increase the contact points and possibly provide more absorbed oxygen to the contact points and facilitate the oxygen diffusion through the catalyst [63]. But when the iron content exceeds 20%, the BET surface area for SCS catalysts degrade significantly (only 2-3 m^2g^{-1}). This makes the available contact points become very limited, resulting in a reduced activity performance.

Table 5.3. T10 and T50 for catalysts in tight contact condition

Tight	CeO_2	Fe_5Ce_{95}	$Fe_{10}Ce_{90}$	$Fe_{20}Ce_{80}$	$Fe_{30}Ce_{70}$	Printex-U
T10-CP(^{0}C)	335.8±1.2	342.4±2.8	328.1±1.9	329.3±1.6	333.1±3.5	581±2.3
T10-SCS(^{0}C)	328.7±2.5	323.6±1.7	336.0±1.2	396.8±2.4	400.9±3.7	581±2.3
T50-CP(^{0}C)	393.1±0.7	400.2±1.3	377.5±2.0	388.5±1.1	396.4±1.0	649±3.1
T50-SCS(^{0}C)	376.2±2.0	371.5±0.8	387.5±1.8	472.8±1.9	476.1±2.3	649±3.1

XRD results showed that Fe was successfully incorporated into CeO_2 lattice for both CP and SCS catalysts. For CP catalysts, the crystal size decreased with introduction of iron, implying that iron incorporation could inhibit crystal growth. In this way, the smaller crystal size and higher surface area can benefit oxygen diffusion and increase contact points. On the contrary, XRD pattern showed that crystal size grew with more Fe doping for SCS catalysts. Crystal growth can be an obstacle for good catalytic performance. The spherical structure of CP catalysts (shown in SEM image), resulting from the nucleation of the precipitates, can explain their higher surface area.

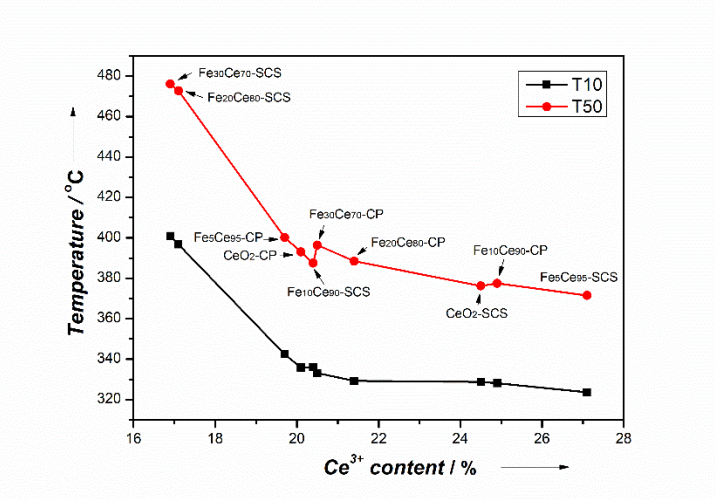

Figure 5.9. Relation between Ce^{3+} percentage and T10, T50

XPS results indicate that 10%-CP and 5%-SCS iron doping had the highest Ce^{3+} and O_α ratios on the surface among their own preparation method, which meant that the oxygen vacancies were maximized at these ratios. The trend of Ce^{3+} and O_α ratio follows the trend of T10 and T50, and hence follows the catalyst activity. Raman results and I_{596}/I_{463} values further confirmed oxygen vacancies, and $Fe_{10}Ce_{90}$-CP and Fe_5Ce_{95}-SCS showed highest oxygen vacancies within their own preparation method. Figure 5.9 shows the relation between Ce^{3+} percentage and T10, T50. It is noticed that the activity (trough T10 and T50) is really directly dependent on Ce^{3+}, irrespective of the preparation method. The ratio of Ce^{3+} can represent the availability of oxygen vacancies [54]

as it is reported that higher Ce^{3+} concentration indicates more oxygen vacancies on the catalyst surface [22, 85, 104]. Therefore, oxygen vacancies on the surface is found to be the determining factor for catalyst activity. With more Ce^{3+} or oxygen vacancy concentration, both T10 and T50 decreased in a similar fashion. Figure 5.9 shows that there is a threshold of around 20% Ce^{3+}, below which the catalyst activity rapidly deteriorates with further decreasing Ce^{3+} content, as indicated by the sharp drops in T10 and T50 at low Ce^{3+} content (T50: 476 to 393°C). The samples with low Ce^{3+} also correspond to the lowest BET surface area (2-3 m^2g^{-1}), which could also contribute to the lower activity. However, because the catalytic soot oxidation involves contact between two solids, the BET surface area is less likely to play the most important role. Thus, the lower activities associated with $Fe_{20}Ce_{80}$-SCS and $Fe_{30}Ce_{70}$-SCS are attributed more to the low Ce^{3+} content than the low BET surface area. Above 20% Ce^{3+}, T10 and T50 would still decrease with increasing Ce^{3+} content, but at a much reduced rate (T50: 393 to 372°C). This meant that Ce^{3+} content, and hence oxygen vacancy, has a great influence on catalyst activity. More oxygen vacancies facilitate adsorbing more oxygen species from gaseous oxygen, which then diffuse through the crystalline structure to the contact point between soot and catalyst and oxidize soot. Due to the existence of Ce^{3+} and Ce^{4+}, the reaction proceeds through redox mechanism. According to the mechanism study by Zhang et al. [29], redox cycle between Fe^{2+} and Fe^{3+} also participates in this soot oxidation and formed Fe-O-Ce bond, suggesting a synergetic effect of Fe and Ce interaction. When Fe^{3+} provided one O to oxidize soot, Fe^{3+} became Fe^{2+}. The Ce^{4+} on the neighboring site can supply one O to Fe^{2+}, changing it to Fe^{3+} through the reduction of Ce^{4+} to Ce^{3+}. Then absorbing one O from bulk could oxidize Ce^{3+} to Ce^{4+} again. The oxygen species are transferred within the catalyst lattice to reach the interface between soot and catalyst. The as-derived catalysts have different crystal structures due to various ratios of iron doping, which can

cause lattice distortion and surface defects, thus changing the bond between Ce and O and creating some oxygen vacancies on the catalyst surface. This is the reason why certain ratios of iron doping can improve the catalyst activity.

H_2-TPR results showed that 10%-CP and 5%-SCS led to the highest reducibility, and therefore, highest activity, which is in agreement with XPS and Raman results. For SCS catalysts with iron doping, more bulk oxygen becomes releasable and can be more easily transferred to surface oxygen and oxidize soot. This makes the diffusion of bulk oxygen very important for SCS catalysts. However, for CP catalysts, the bulk oxygen reduction peaks were almost unchanged, implying that the Fe doping does cannot influence the bulk oxygen reduction.

Herein, the different activities of the as-produced catalysts were due to their different morphologies, lattice distortion and changed surface properties based on various iron doping. When the Fe doping ratio was lower than 5%, SCS catalysts showed better activity towards soot oxidation regardless of their low BET surface area. This is due to their porous structure, high surface oxygen vacancy concentration and better reducibility of surface oxygen. However, when the Fe doping ratio exceeds 10%, CP catalyst performed better, which can be attributed to their relative higher surface oxygen vacancies.

The activation energy (Ea) of 10% Fe doped ceria catalyst made by SCS method was calculated based on ETEM and TGA results. It was found that the two activation energies were very different, 35 kJ/mol and 109 kJ/mol for ETEM and TGA, respectively. An important difference between ETEM and TGA analysis is that in the ETEM, the focus was on a few particles that were well contacted with clear observable movement (i.e. particles with high reaction rate). On the other

hand, for TGA, the results represent the oxidation of the entire particles bed where soot/catalyst particles were reacting at different rates.

5.5. Summary

Distinct morphologies of iron doped ceria catalyst with different Fe doping ratios were prepared by co-precipitation and solution combustion methods, for catalyzing soot oxidation. It was confirmed by XRD that iron was incorporated in the cerium oxide lattice, which formed a solid solution. The main conclusions of this study are:

- Irrespective of the fabrication method, the most important parameter that dictates the reaction activity (e.g. T50) is the Ce^{3+} content, which is closely related to the content of oxygen vacancies.

- The activity increases notably when Ce^{3+} content increases up to 20% (T50 from 476°C at 17% Ce^{3+} down to 393°C at 20% Ce^{3+}). Above 20% Ce^{3+} content, the activity increases moderately (T50 of 372°C at 27% Ce^{3+}).

- For both fabrication methods, there is an optimum Fe content that gives the highest activity. For SCS catalyst, the optimum Fe content is 5%, and for CP catalyst, it is 10%.

- The pore size is mostly about 3-5 nm (both CP and SCS), which is much smaller than the 25 nm soot particles used here. This is why, although the BET surface area is greater for CP than SCS, it has only moderate effect on the activity.

- The catalyst preparation method has a profound impact on the catalyst morphology. The CP catalyst shows dense spherical morphology, whereas the SCS catalyst has a spongy structure with large openings, around 250 nm, which can be large enough for soot particles to penetrate in and contact with the catalyst. Therefore, it can be anticipated that more soot particle can deposit on the SCS catalyst.

Chapter 6: Investigation of the Stability of Ceria-based Catalysts

6.1. Overview

As poor stability of CeO_2 catalysts has become the major obstacle on their wide application on DPF, it is necessary to develop stable catalysts towards soot oxidation. In this study, different ratios of Samarium (Sm) were doped into CeO_2 lattice to improve catalyst stability. The stability was investigated by recycling the catalyst, mixing it with soot again and repeating running TGA tests for seven times. It was found that doping 5%, 10% and 20% samarium into CeO_2 lattice can improve the catalyst stability, but at the price of losing some activity. With increase of Sm doping, the catalyst became more stable. Considering stability and activity together, 10% Sm-doped catalyst showed best compromise between stability and activity. Ce^{3+} and O_α played the most important role in controlling catalytic soot oxidation activity, because they are directly related to oxygen vacancies and oxygen storage capacity of the catalyst. Sm-doped catalysts showed minimum decrease in Ce^{3+} and O_α content between fresh and spent catalysts. In addition, crystal growth is not considered as the most important parameter for catalyst deactivation. Finally, although addition of Fe on 20% Sm-doped ceria catalyst did improve the activity in early cycles, it showed poor stability.

6.2. Introduction

Ceria has already been widely studied towards soot oxidation because of its excellent redox properties and oxygen storage capacity (OSC). Previous studies have shown that metal-doped ceria can further improve the activity of ceria-based catalysts [22]. In Chapter 5, the activities of iron doped ceria catalysts at different doping ratios were investigated. It was found that 5% iron doping

prepared with SCS performed best due to its highly reactive Fe-O-Ce sites. Chapter 5 reported on the reactivity of fresh catalysts, but not on catalyst stability, which is the focus of the present chapter.

It was reported that the active sites, crystal structures and surface properties of ceria-based catalysts could change during the reactions, resulting in poor stability of ceria-based catalysts [121]. All studies agreed that pure CeO_2 shows poor stability for soot oxidation, which has become a major obstacle for the wide application of ceria-based catalysts [34, 121-123]. Liang et al. [121] have studied the thermal stability of CeO_2 for soot oxidation by aging the catalyst at 800°C for 20 hours in air. They found that the temperature corresponding to the maximum rate for CO_2 production with aged catalyst increased by about 60°C compared to fresh catalyst, because of the highly reduced surface area and sintering. Aneggi et al. [34] observed that aging CeO_2 catalyst at 750°C for 12 hours in air decreased its activity for soot oxidation as it lost oxygen storage capacity. Liu et al. [122] investigated the deactivation of CeO_2 for soot oxidation through isothermal conditions at 300 and 350°C; they found that deactivation occurred at isothermal conditions and became more severe at higher temperature. The main reported reason for deactivation is inefficient O_2^- formation. Corro et al. [123] tested the stability of CeO_2 towards soot oxidation during 6 cycles and found a slow and continuous deactivation of CeO_2.

Therefore, the stability of CeO_2 based catalysts for soot oxidation needs to be improved. Many studies have looked at the incorporation of metal dopants into CeO_2 lattice to improve stability, as described next. Wu et al. [8, 41, 44, 102] added BaO or Al_2O_3 into transition metal (Mn, Cu) doped CeO_2 to improve its thermal stability. They found that these metals could improve the thermal stability after aging at 800°C for 24 hours in air because they hinder crystal growth. Aneggi [34]

and Liang et al. [121] incorporated ZrO_2 into Fe-Ce and Cu-Ce mixed oxides and found enhanced thermal stability due to the formation of stable solid solutions. Gao et al. [124] have aged Nd-Ag/CeO_2 catalyst at 700°C for 48 hours under 1%O_2/10%H_2O/N_2, revealing Nd could prevent crystal growth, thus improving thermal stability of Ag/CeO_2. Xiong et al. [125] have added Y and La into Zr/CeO_2 catalyst and aged it from 700 to 1000°C. The catalyst activity remained stable below 800°C but decreased significantly above 900°C. Zhang et al. [126, 127] investigated the influence of thermal stability by adding Y into MnO_x-CeO_2 and introducing Al, La, Y, or Zr into Pt/MnO_x-CeO_2 after aging at 800°C for 12 hours in air. They observed that incorporation of dopants can prevent the sintering and slow down crystal growth. Peralta et al. [79, 128] introduced Ba into alkali metals-modified ceria such as K/CeO_2 and obtained good thermal stability as no deactivation was observed after aging at 800°C. Noble metals, such as Ru, have also been investigated as dopant to successfully improve ceria-based catalyst stability after aging at 800°C in O_2 [129]. Although all the studies described previously investigated stability through accelerated thermal aging, only a few studies investigated stability through more realistic, albeit more cumbersome, soot oxidation cycles [92, 130-132]. La loaded on CeO_2-ZnO (5 cycles) [132], K added into CeO_2 (3 cycles) [130], co-doping of Ag and Mn into CeO_2 (3 cycles) [131] and Au doped $Ce_{0.8}Zr_{0.2}O_2$ (3 cycles) [92] all showed enhanced stability of ceria-based catalysts for soot oxidation. These studies identified that resistance of sintering and crystal growth, ability of CO_2 desorption, and oxygen species replenishment are important roles for catalyst stability on soot oxidation.

Stability of ceria-based catalysts have also been investigated for applications other than soot oxidations [133, 134]. One family of applications relates to catalytic combustion of different gases.

Dai et al. [135] investigated the stability and deactivation of CeO_2 catalyst and found that T50 increased from 165°C to 325°C after nine cycles of trichloroethylene combustion. Zhang et al. [136] studied Al, Zr, La, or Y doped Pt/MnO_x-CeO_2 stability toward NO oxidation after aging, and observed that modified ceria catalyst showed better activity. Han et al. [134] investigated the stability of ZrO_2-doped CeO_2-based catalyst for toluene combustion, revealing that ZrO_2 can stabilize the surface active structure, thus improving stability. Polychronopoulou et al. [137] investigated Sm_2O_3/CeO_2 catalysts for CO oxidation, finding that adding Sm can significantly improve the thermal stability of conventional CeO_2 catalyst. Mandal et al. [138] have demonstrated enhanced stability of Gd-Sm-CeO_2 for benzyl alcohol oxidation. Another important family of applications using ceria-based catalysts is solid oxide fuel cell (SOFC) (and its reverse operation solid oxide electrolysis, SOEC) for intermediate temperature (650-750°C). The main ceria-based material investigated for SOFC and SOEC are samarium doped ceria (SDC) [139, 140] and Gadolinium doped ceria (GDC) [133, 141]. Sm and Gd were added essentially to stabilize ceria during operation at high temperature, while achieving good oxygen ion conductivity, as they can inhibit crystal growth and prevent sintering [147].

From the above literature review on stability of ceria-based catalyst, it is somewhat surprising to see almost no studies on samarium doped ceria despite proven long-term stability at high temperatures (750-850°C) in SOFC/SOEC. Granted, SDC in SOFC/SOEC has a different purpose (electrolyte to transport oxygen ion) than it would have in soot oxidations. Yet, SDC should be a promising stable catalyst for soot oxidation because of its thermal stability at high temperature. Very few papers studied Sm as dopant to ceria for soot oxidation. Liu et al. [93], using loose contact condition, studied activity and thermal stability (calcination at 800°C for 20 hours) of a 20% Sm-doped ceria catalyst prepared through microwave assisted heating decomposition.

Sudarsanam et al. [142] carried out a similar study, except under tight contact condition and with co-precipitation catalyst preparation method. Both reported increase in combustion temperatures after aging, but are not conclusive regarding actual catalyst stability. Anantharaman et al. [143] did not investigate catalyst stability, but studied the effect of Sm content on soot oxidation reactivity for Sm-doped ceria catalyst prepared by EDTA-citrate method; they found that 10% Sm doping performed best on a fresh catalyst calcined at 600°C for 5 hours.

The present study aims at developing an optimum ratio of Sm doping into CeO_2 catalyst to improve catalyst stability for soot oxidation. Therefore, in this chapter, different ratios of Sm doping were investigated, along with its influence on catalyst surface properties and activity. Characterizations were performed to understand surface and crystal properties of catalyst. Seven repeating reaction cycles were used to study the activity and stability of Sm-doped CeO_2 catalyst.

6.3. Experimental procedures

6.3.1 Preparation of the catalysts

Sm_x/Ce_{1-x} (x = 0.05, 0.10 and 0.20 in percent molar ratio) catalysts were obtained by SCS preparation method. An aqueous solution of Samarium nitrate nonahydrate (Sigma-Aldrich, CAS: 13759-83-6, 99.999% trace metals basis), cerium nitrate hexahydrate (Sigma-Aldrich, CAS: 10294-41-4, 99.999% trace metals basis) and glycine (Sigma-Aldrich, CAS: 56-40-6) in a stoichiometric ratio was prepared under vigorous stirring at 90°C to form a gel. Then, the gel was combusted on a heating plate. The combustion procedure was fast, producing nano powders (around 20 nm). The resulting samples were then calcined at 500°C for 5 hours. CeO_2-SCS catalyst was developed using a similar procedure.

6.3.2 Catalysts' activity and stability tests

TGA was used to test the catalyst's activity for soot oxidation through a TA Instrument Q500 apparatus. Printex-U carbon black was used as model of soot. Catalyst and soot particles were weighted at a ratio of 9:1 and then mixed by grinding them for 10 minutes in order to obtain tight contact condition [29]. For the first cycle of TGA test, a weighted amount of 40 mg sample was pre-treated at 150°C under 60 mL/min nitrogen for 30 min to remove water. Then, the sample was heated up to 600°C under 40 mL/min air with a heating rate of 10°C/min. The thermogravimetric curves were obtained by continuously recording the mass change, along with increased temperature. The catalyst's activity was evaluated by T50. T50 is the combustion temperature, identified as the temperature when 50% of soot is oxidized [4, 5, 63, 150].

The stability tests were performed through several soot oxidation cycles using the same catalyst. One cycle is defined by a step of mixing soot and catalyst particles, followed by a step of soot oxidation in the TGA. Once the first cycle soot oxidation reaction was completed, the remaining catalyst was collected and re-mixed with soot particles again under tight contact condition with the same weighting ratio of 9:1. TGA test was run again with the newly mixed sample. This procedure was repeated for several cycles. Note that after each cycle, it was inevitable that some amount of catalyst is lost (mostly during the mixing step where several particles stick to the mortar and pestle). This means that for a given amount of fresh catalyst there will be a maximum number of cycles that can be investigated; for example, with our typical 36 mg of fresh catalyst (with 4 mg of carbon), it was hardly possible to go beyond 7 cycles.

6.3.3 Characterization of the catalysts

X-ray powder diffraction (XRD) analysis was performed on X-ray powder diffractometer (German Bruker D4 (40 kV, 30 mA), with position-sensitive detector and CuKα radiation). The XRD patterns were recorded in steps of 0.01° with a scanning rate of 5°/min from 5° to 85°. The diffraction peaks were indexed according to the Powder Data File database (PDF 2004, International Centre of Diffraction Data, Pennsylvania). Specific surface areas were measured by means of N_2 adsorption-desorption isotherms using a Beishide 3H-2000PS2 static volumetric method analyzer. Catalysts' surface areas were evaluated by the Brunauer-Emmett-Teller (BET) method.

The morphologies, microstructures and elemental compositions of the obtained catalysts were characterized by a Field-emission scanning electron microscope (FE-SEM, Zeiss MERLIN with Gemini-II column).

X-ray photoelectron spectroscopy (XPS) measurements were carried out on ESCALab220i-XL electron spectrometer (VG Scientific Ltd, UK) with 300 W AlKα X-ray source equipment to investigate the oxidation states of cerium and iron, and availability of oxygen on catalyst surface. The calibration of binding energy was conducted by using C1s peaks at 284.8eV. Spectra-fits were performed with Gaussian-Lorentzian functions by using CasaXPS software.

The Raman spectra of the catalysts were measured on a Renishaw InVia micro laser Raman spectrometer (Renishawplc, Wottonunder-Edge, UK) with a 4mW Ar+ laser source (λex = 532nm) with a cooled CCD detector at room temperature to differentiate chemical structures. The acquisition time was 60s and the scanning range was 200-800cm^{-1}.

6.4. Results and discussion

6.4.1 Fresh and spent catalysts characterizations

The crystalline structures of catalysts were studied by XRD. Figure 6.1 presents the XRD pattern of fresh and spent Sm-doped CeO_2 catalysts, as well as pure CeO_2 for comparison. All XRD patterns show similar main diffractions peaks, which can be attributed to (111) (200) (220) (311) (222) (400) (331) (420) planes. These peaks refer to typical cubic fluorite structures of pure CeO_2 [165]. No peaks referring to Sm_2O_3 were found, even for 20% SDC, meaning that no individual Sm_2O_3 crystal structure was detected, indicating that the Sm forms a solid solution in ceria lattice. For fresh catalysts, when increasing the Sm doping ratio, the characteristic peaks shifted to lower 2θ diffraction angles, further suggesting that Sm was incorporated into CeO_2 lattice and formed solid solution. The unit lattice parameters were calculated by Bragg's law using the strongest peak (111), and the crystal size was calculated by Scherrer equation. With an increase in Sm doping, the lattice parameter (as shown in Table 6.1) tends to increase, because of the larger Sm atoms (1.07 Å) substituting smaller ceria atoms (0.97 Å) in the lattice, thus resulting in lattice expansion [170].

As seen in Table 6.1, comparison of fresh and spent catalysts shows that the lattice parameters of spent catalysts slightly increased compared to fresh catalysts with the same doping ratio. Although those increases are very small, the trend is clear that the change in lattice parameters decreases as the amount of Sm increases: for pure ceria, 5%, 10%, and 20% Sm, the differences in lattice parameters between fresh and spent catalysts are 0.013, 0.006, 0.004 and 0.003 Å. Although for fresh catalyst, the crystal size clearly increases as the amount of Sm increases (from 12.3 nm for pure ceria to 13.6 nm for $Sm_{0.2}Ce_{0.8}$), such clear trend is not observed for the spent catalysts where

the crystal size seems to converge for a size range between 13.5 and 14.5 nm. The spent catalysts always showed higher crystal size than the fresh one, indicating that there is an increase in crystallinity after several cycles of reactions on the catalyst. For all spent catalysts, $Sm_{0.1}Ce_{0.9}$ showed a notably lowest crystal size.

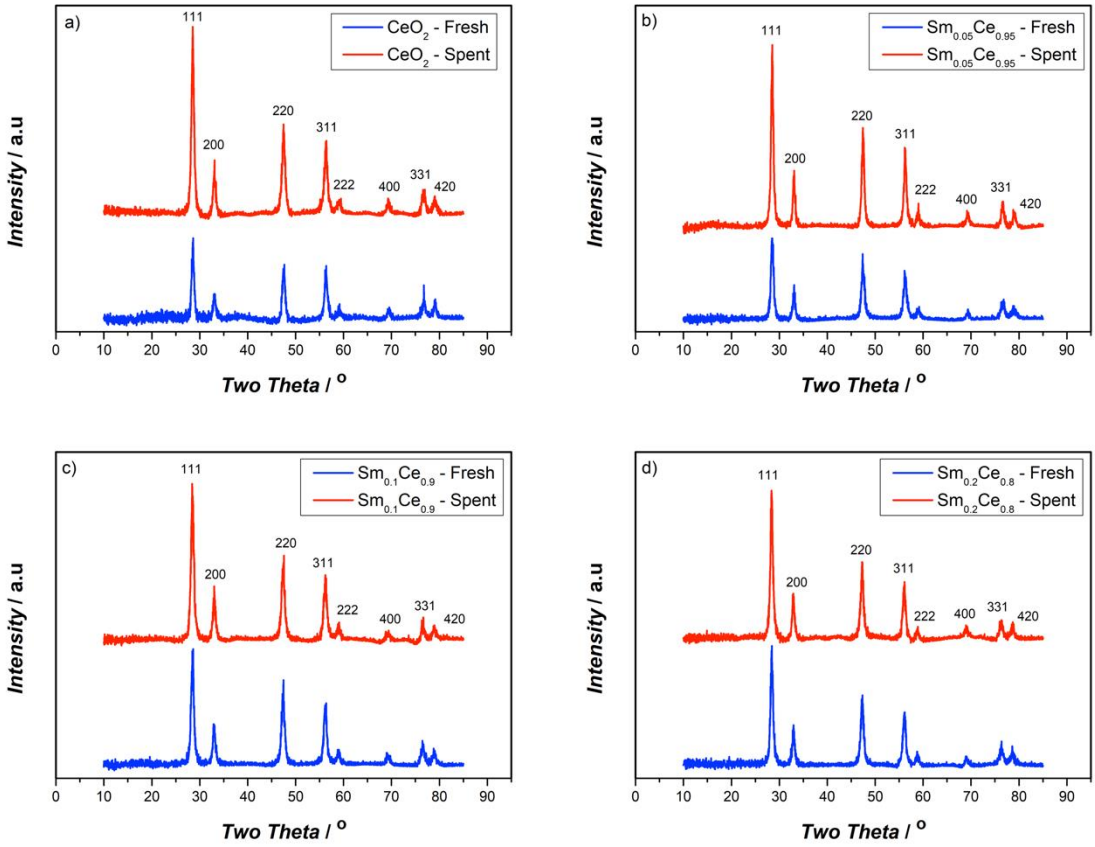

Figure 6.1. XRD results of fresh and spent catalysts after 5 cycles of reactions a) CeO_2, b) $Sm_{0.05}Ce_{0.95}$, c) $Sm_{0.1}Ce_{0.9}$, d) $Sm_{0.2}Ce_{0.8}$

The BET surface areas for Sm-doped ceria catalysts are listed in Table 6.1. For the fresh Sm-doped catalysts, except $Sm_{0.1}Ce_{0.9}$, they all have a surface area of 41- 42 m^2g^{-1}, which is lower than that for fresh pure ceria (45.5 m^2g^{-1}). Fresh $Sm_{0.1}Ce_{0.9}$ obtained the highest BET surface area of 48 m^2g^{-1}.

When comparing fresh and spent catalysts, the BET surface area of pure CeO_2 decreased the most (from 45.5 to 40.9 m^2g^{-1}). Sm-doped CeO_2 catalysts also showed a slight decline in BET surface area (2-4% loss) regardless of the doping ratio. Interestingly, with the exception of $Sm_{0.1}Ce_{0.9}$ all other spent catalysts, including pure ceria, have similar surface area, around 40-41 m^2g^{-1}. There seems to be something particular for $Sm_{0.1}Ce_{0.9}$, which had the highest surface area for both fresh and spent catalysts. Note that this catalyst also stood out, having the lowest crystal size after several cycles. Since the catalysts for XRD and for BET characterization were made from different batches, it indicates that $Sm_{0.1}Ce_{0.9}$ presents interesting properties, which cannot be attributed to experimental error.

Table 6.1. Texture results of Sm-doped ceria fresh and spent catalysts (after 5 cycles). Percentages for spent catalysts indicate relative change compared to fresh catalysts.

Catalyst	Crystal size [nm]	Lattice parameter [Å]	S_{BET} [m^2g^{-1}]
CeO_2-fresh	12.33 (±0.09)	5.405 (±0.0018)	45.5 (±1.57)
$Sm_{0.05}Ce_{0.95}$-fresh	12.43 (±0.19)	5.424 (±0.0075)	42.2 (±0.99)
$Sm_{0.1}Ce_{0.9}$-fresh	11.89 (±0.17)	5.432 (±0.0028)	48.3 (±0.78)
$Sm_{0.2}Ce_{0.8}$-fresh	13.61 (±0.06)	5.442 (±0.0014)	40.9 (±1.94)
CeO_2-spent	14.52 (±0.13)/ +17.8%	5.418 (±0.0015)	40.9 (±1.43)/ -10.1%
$Sm_{0.05}Ce_{0.95}$-spent	14.71 (±0.07) / +18.3%	5.430 (±0.0015)	40.5 (±0.75)/ -4.0%
$Sm_{0.1}Ce_{0.9}$-spent	13.33 (±0.11)/ +12.1%	5.436 (±0.0032)	46.2 (±2.36)/ -4.3%
$Sm_{0.2}Ce_{0.8}$-spent	14.26 (±0.12)/ +4.8%	5.445 (±0.0087)	40.2 (±1.52)/ -1.7%

SEM was used to study surface morphologies of the produced catalysts. Figure 6.2 shows the SEM images of all fresh and spent catalysts. All fresh catalysts have spongy structures with large openings, which are due to their fast combustion reaction during SCS. The main effect of Sm doping on the catalyst morphology is to increase those openings. However, all spent catalysts lost the spongy structure and tend to agglomerate, to have in the end very similar morphologies.

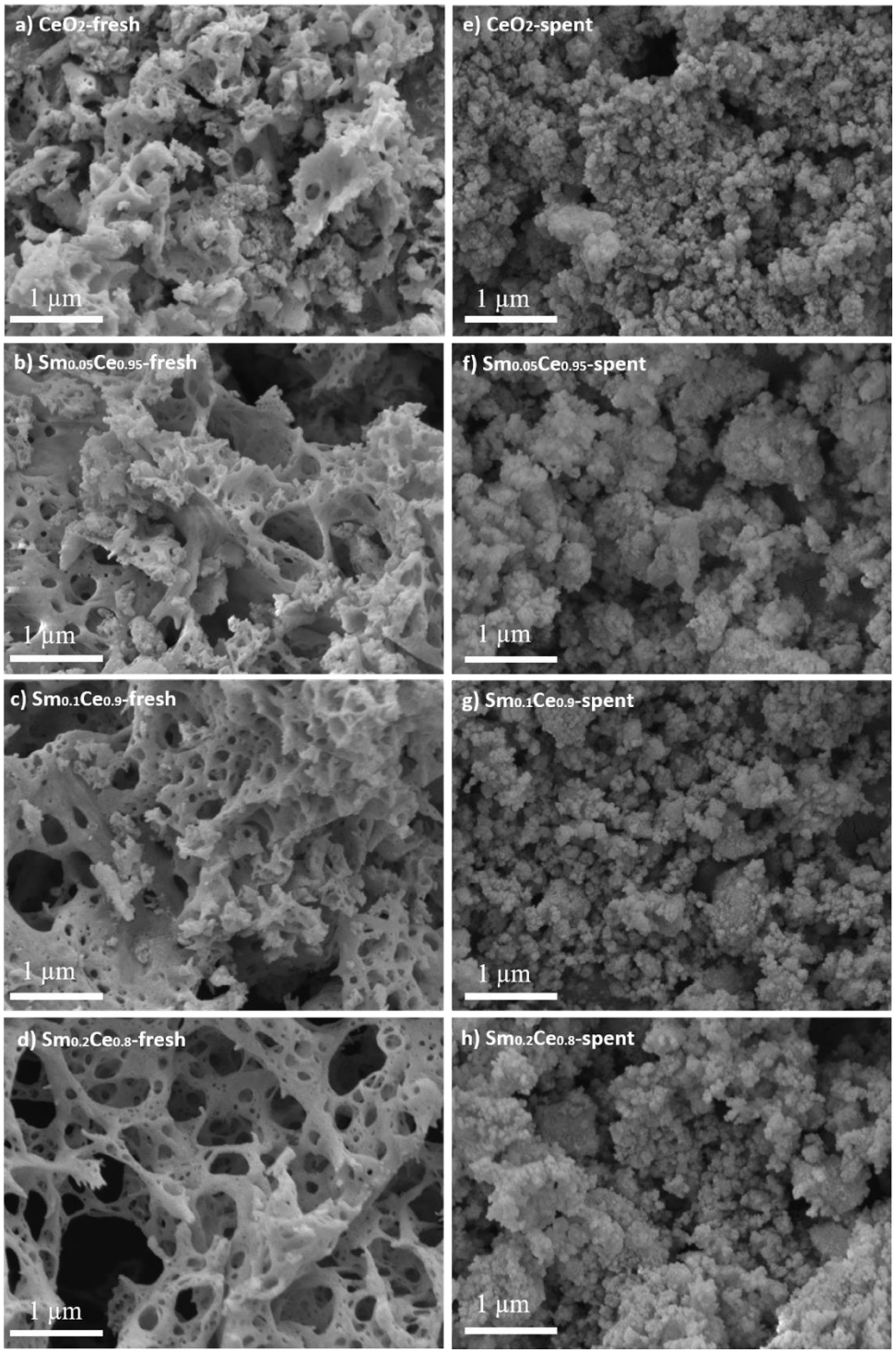

Figure 6.2. SEM images of all fresh and spent catalysts after 5 cycles. a) CeO_2-fresh; b) $Sm_{0.05}Ce_{0.95}$-fresh; c) $Sm_{0.1}Ce_{0.9}$-fresh; d) $Sm_{0.2}Ce_{0.8}$-fresh; e) CeO_2-spent; f) $Sm_{0.05}Ce_{0.95}$-spent; g) $Sm_{0.1}Ce_{0.9}$-spent; h) $Sm_{0.2}Ce_{0.8}$-spent.

XPS was used to detect different oxidation states of each element. Figure 6.3 is the XPS spectra of all catalysts regarding their Ce3d and O1s spectra. Ce3d spectra can be split into 8 peaks for detailed analysis. The peaks labeled with "u" and "v" correspond to the spin-orbit splitting of Ce 3d5/2 and Ce 3d3/2, respectively. The peaks v0, v2, v3, u0, u2, u3 are the characteristic peaks for Ce^{4+} species and peaks noted with v1, u1 correspond to Ce^{3+} species [29]. It is clear that ceria exists primary as Ce^{4+} for each catalyst, with the coexistence of some Ce^{3+}. Since oxygen vacancy is generated when Ce^{4+} is reduced to Ce^{3+}, it is crucial to calculate the Ce^{3+} percentage in order to evaluate the generation of oxygen vacancy on the catalyst surface [5, 33]. The calculations of integrated peak areas can be used to quantitively analyze XPS results. The ratio of Ce^{3+} was calculated by dividing the peak areas of Ce^{3+} by the total peak area. Table 6.2 shows the results of Ce^{3+} percentage for fresh and spent catalysts. For fresh catalysts, it is found that adding Sm into CeO_2 lattice decreases the Ce^{3+} percentage (about 15-17%) from that in pure ceria (24%). 5% and 10% Sm doping possesses similar Ce^{3+} percentage (~17.3%) and 20% Sm-doped catalyst has the lowest Ce^{3+} percentage (15.3%).

Table 6.2 indicates that Ce^{3+} percentage of spent catalysts decreases when compared to fresh catalysts. Pure CeO_2, in particular, showed a significant Ce^{3+} percentage decrease, from 23.8 % to 13.8%, that is, it changed from the highest percentage to the lowest one. However, Sm-doped catalysts showed lower decrease (1% for 5% doping and 0.7% for 10% doping). The Ce^{3+} percentage for the $Sm_{0.2}Ce_{0.8}$ catalysts only decreased by about 0.4%. Those results suggest that Sm help establishing a more stable catalysts' surface, at least in term of Ce^{3+} content.

The O1s spectra were curve fitted into two peaks, including lattice oxygen O_β at a lower binding energy of 529.5 eV and surface oxygen species O_α at a higher binding energy of 531.7 eV [89].

The concentration of O_α is critical to evaluate oxygen storage capacity (OSC) and potential active oxygen for soot oxidation. The ratio O_α / (O_α+ O_β) was calculated by dividing the peak areas of O_α by the total peak areas, whose results are shown in Table 6.2. This table shows that, for fresh catalysts, Sm doping up to 10% marginally decreases the O_α ratio (from 39.5 down to 39.1%). However, the decrease in O_α ratio is more pronounced for 20% Sm doping (O_α ratio of 34.2%). The results regarding O_α ratio are in agreement with that of Ce^{3+} percentage.

Regarding spent catalysts, the O_α ratio of pure CeO_2 dropped significantly compared to that of fresh CeO_2 catalyst (from 39.6% to 29.5%) and became the lowest among all spent catalysts. On the other hand, the O_α percentage for 5% and 10% Sm-doped ceria catalysts decreased by less than 2% point. Finally, the 20% Sm-doped catalysts did not show decrease in O_α content, although its final value is still lower than for the other two Sm-doped ceria catalysts. Those results suggest that Sm doping, reduces considerably the loss in surface oxygen after several cycles.

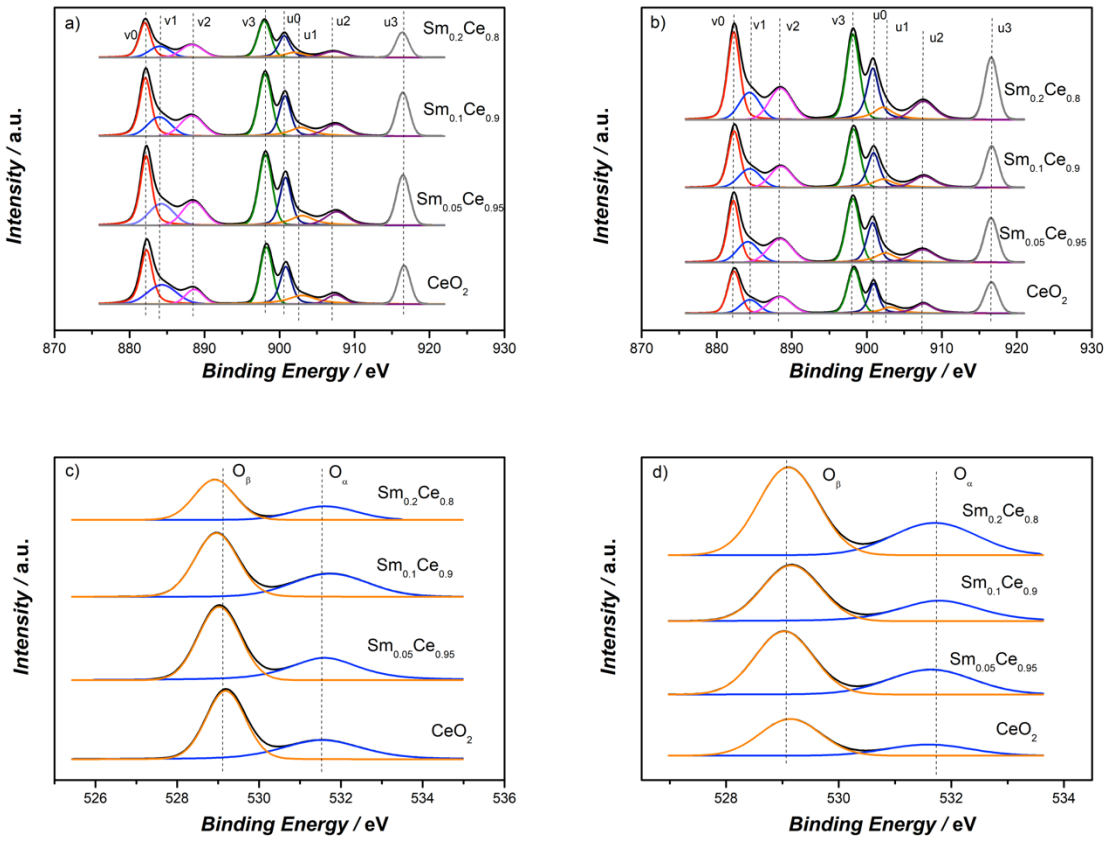

Figure 6.3. XPS results of a) Ce3d of fresh catalysts, b) Ce3d of spent catalysts, c) O1s of fresh catalysts, d) O1s of spent catalysts

Table 6.2. Ce^{3+} percentage and O_α percentage

Catalyst	CeO_2	$Sm_{0.05}Ce_{0.95}$	$Sm_{0.1}Ce_{0.9}$	$Sm_{0.2}Ce_{0.8}$
Ce^{3+} (%)-fresh	23.8	17.2	17.3	15.4
Ce^{3+} (%)-spent	13.8	16.2	16.6	15.0
O_α(%)-fresh	39.6	39.1	39.2	34.2
O_α(%)-spent	29.5	37.4	37.6	34.2

Raman spectra of Sm-doped CeO_2 catalysts are depicted in Figure 6.4. The dominant band around 463 cm^{-1} correspond to the F2g symmetric oxygen mode within a CeO_2 cubic fluorite structure, which is in agreement with XRD results [142]. With the increase of Sm doping ratio, the F2g band

shifted to lower frequency due to the cell expansion in the catalysts. No peaks of Sm_2O_3 (~375 cm^{-1}) were found, reinforcing that Sm-Ce forms a solid solution [138]. The weak peak around 596 cm^{-1} represents the surface defects including intrinsic oxygen vacancies cause by Ce^{3+} in the lattice [29]. The peak around 554 cm^{-1} refers to the extrinsic oxygen vacancy created by Sm^{3+} substituting Ce^{4+}, in order to maintain charge neutrality [171]. With an increase in Sm doping, the peak intensity at 554 cm^{-1} becomes stronger, indicating that more Sm^{3+} associated oxygen vacancies are created. The ratio I_{554}/I_{596} represents, therefore, the ratio of oxygen vacancies originating from Sm^{3+} over that from Ce^{3+}. Results pertaining to the I_{554}/I_{596} ratio are shown in Table 6.3. For fresh catalysts, as expected, incorporation of Sm increases the I_{554}/I_{596} ratio. Note that for spent $Sm_{0.2}Ce_{0.8}$, this ratio is above 1, indicating more oxygen vacancies from Sm^{3+} than from Ce^{3+}, whereas it is the opposite for Sm content below 10% (values of the I_{554}/I_{596} ratios below 1).

After five cycles of reactions, the I_{554}/I_{596} ratio for all catalysts further increased (by about 0.1). This indicates that after several cycles, the relative amount of oxygen vacancy correlated to Sm^{3+} increases (and its corollaire, that the relative amount of oxygen vacancy correlated to Ce^{3+} decreases). The peak intensity of the Raman spectra increases, in all cases, after 5 cycles, possibly due to the increase in crystal growth, which is in agreement with XRD results. Another reason could be lattice distortion of spent catalysts leading to resonance with inlet Ar^+ laser source.

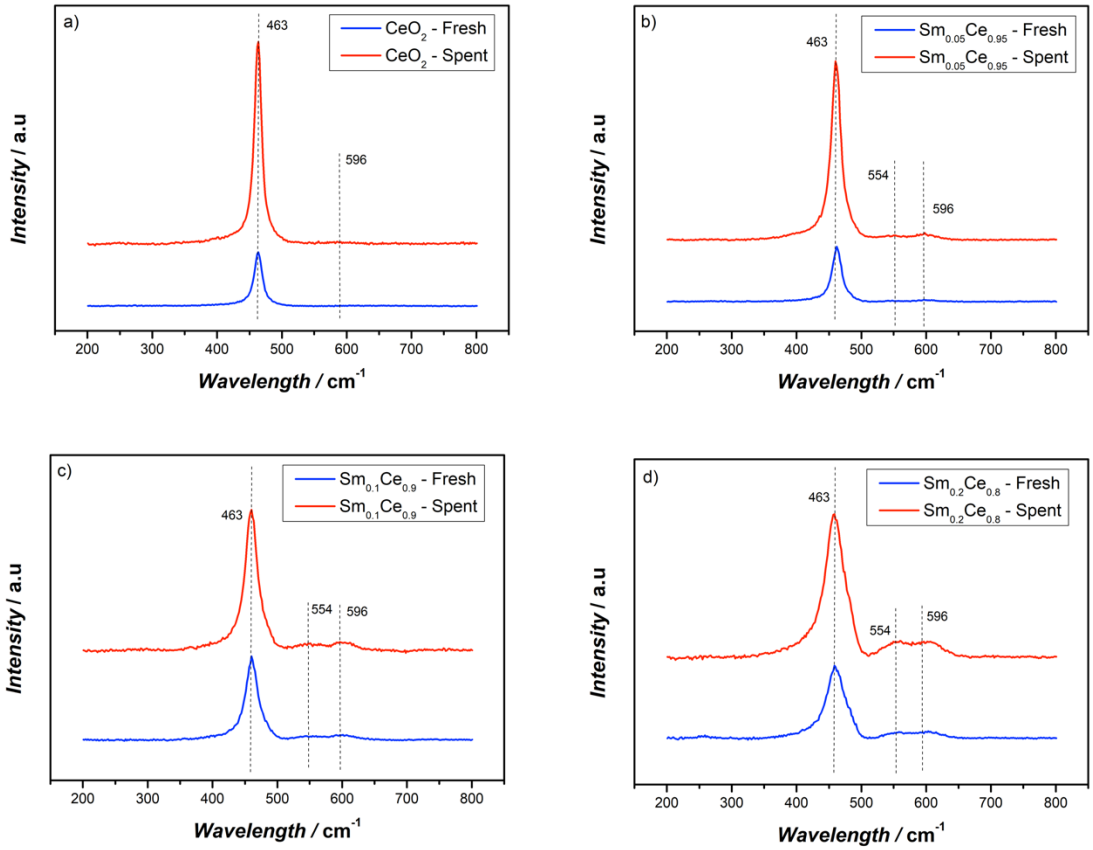

Figure 6.4. Raman results of fresh and spent catalysts after 5 cycles of reactions a) CeO_2 b) $Sm_{0.05}Ce_{0.95}$, c) $Sm_{0.1}Ce_{0.9}$, d) $Sm_{0.2}Ce_{0.8}$

Table 6.3. I_{554}/I_{596} of Raman results.

	$Sm_{0.05}Ce_{0.95}$	$Sm_{0.1}Ce_{0.9}$	$Sm_{0.2}Ce_{0.8}$
I_{554}/I_{596}-fresh	0.52	0.63	0.97
I_{554}/I_{596}-spent	0.69	0.73	1.06

6.4.2 Activity

TGA experiments were performed to study the activity of fresh Sm-doped CeO_2 catalyst for soot oxidation. Figure 6.5 depicts soot conversion as a function of temperature. Fresh pure CeO_2 catalyst achieves the highest activity, as indicated by the lowest T50. Increasing Sm content in

fresh catalysts tends to increase T50, revealing a loss in activity. In fact, 5% and 10% Sm doping ratio for fresh catalyst show similar effects on catalyst activity, whereas the 20% Sm doping sample led to the worst activity.

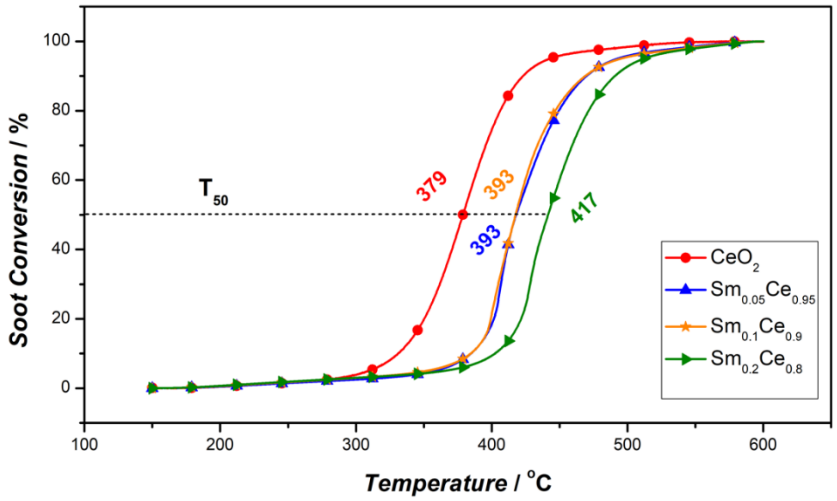

Figure 6.5. Soot conversion activity test of fresh Sm-doped ceria catalysts

Since catalytic soot oxidation is a surface sensitive reaction, i.e. reaction only happens at the contact point of soot and catalyst, crystal size, specific surface area and morphology can all play an important role on the catalyst activity. From Figure 6.2, the morphology does not change significantly between pure ceria and Sm-doped catalysts, and thus cannot explain the difference in reactivity. Table 6.1 indicates that BET surface area increase slightly when increasing Sm content, but this would lead to higher activity at higher Sm content, which is the opposite of what was observed; BET surface area can, thus, not explain here the trend in activity. Finally, Table 6.1 shows modest change in crystal size when increasing Sm content, and without a clear trend. Crystal size can, therefore, also be dismissed to explain the activity trend for the fresh catalysts.

Soot oxidation on ceria-based catalysts occurs via the so-called Mars-Van-Krevelen mechanism

[22], where the active surface oxygen reacts with soot through catalyst-soot contact point. Once the active oxygen is consumed, an oxygen vacancy is generated at the surface, and bulk O_2 fills this vacancy and create another active oxygen. Therefore, factors affecting the amount of active surface oxygen and oxygen vacancies can also play an important role in determining catalyst activity. Ce^{3+} content is a good representation of oxygen vacancy generation which, in turn, can be potential site for creating active surface oxygen. Here, surface oxygen and oxygen vacancies are related to Ce^{3+} content, O_α percentage and I_{554}/I_{596} ratio. Those are discussed next.

Figure 6.6a shows the relation between T50 and Ce^{3+} percentage, which indicates that the higher the Ce^{3+} content, the lower the T50 (and thus the higher the activity). The highest Ce^{3+} ratio (23.8%) corresponds to fresh pure CeO_2 catalyst, which can be a reason for the highest activity of pure ceria. The activity results reported in Figure 6.5 for Sm-doped catalysts correlates very well with the Ce^{3+} content shown in Table 6.2: 5% and 10% doped CeO_2 have identical Ce^{3+} content, and also very similar activity (e.g. same T50), whereas $Sm_{0.2}Ce_{0.8}$ has much lower Ce^{3+} content, as well as much lower activity (i.e. higher T50).

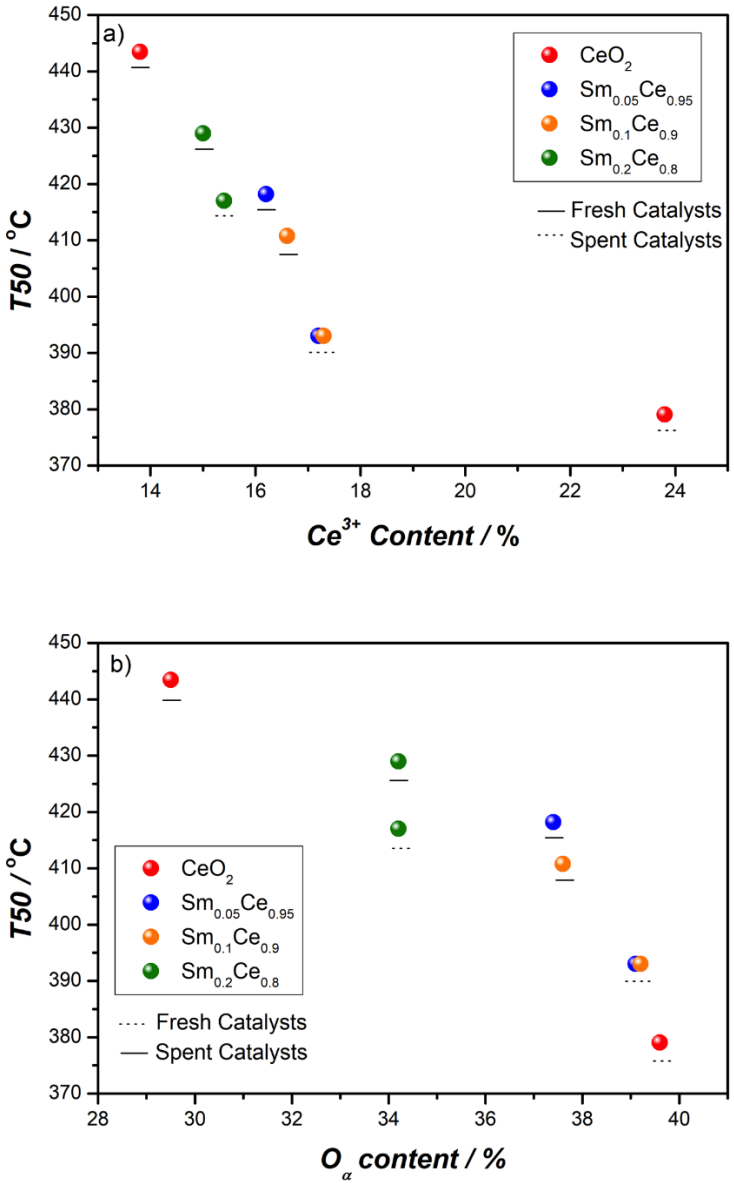

Figure 6.6. Effect of Ce^{3+} percentage and O_α percentage on activity for all catalysts. a) T50 vs. Ce^{3+} percentage, b) T50 vs. O_α percentage

Figure 6.6b shows the relation between T50 and O_α percentage, which follows the trend of Ce^{3+} content, indicating that surface oxygen species are also vital for catalyst activity. It has been reported that higher O_α concentration could result in superior catalyst activity, as it can evaluate the oxygen storage capacity and potential active oxygen for reaction. From Table 6.2, O_α

percentage slightly decreased for 5% and 10% Sm-doped catalysts, but it considerably decreased for 20% Sm doping, when comparing with pure CeO_2; the data about O_α percentage also correlates very well with activity results.

The relation between T50 and I_{554}/I_{596} ratio is illustrated in Figure 6.7, which shows that T50 increased when increasing the I_{554}/I_{596} ratio. This implies that Sm^{3+} associated oxygen vacancy decreases the catalyst activity. From XPS results, it is already known that higher Ce^{3+} associated oxygen vacancy plays a key role in improving catalyst activity. Therefore, both the increase in oxygen vacancy around Sm^{3+} and decrease of oxygen vacancy adjacent to Ce^{3+} lead to activity decline.

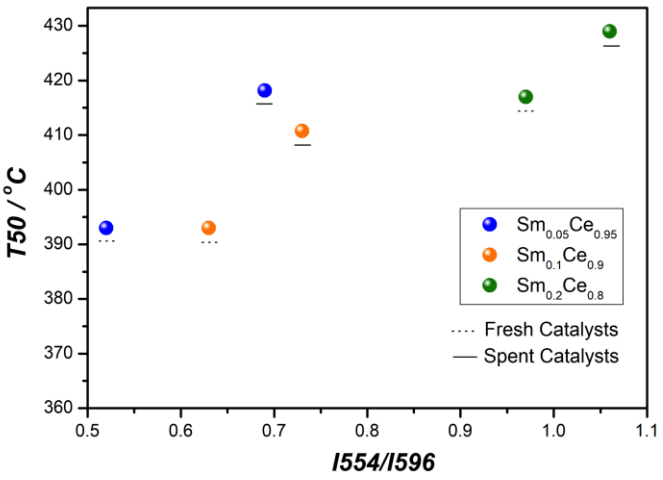

Figure 6.7. The relation between T50 and I_{554}/I_{596}

6.4.3 Stability tests for Sm-doped CeO_2 catalysts

Figure 6.8 presents the results of stability on Sm-doped CeO_2 for soot oxidation through 7 cycles. This figure shows that T50 for pure CeO_2 catalyst increased after each cycle, going from the lowest

value (379°C) with fresh catalyst to the highest one (462°C) after 7 cycles. The $Sm_{0.05}Ce_{0.95}$ catalyst also shows a continuous increase in T50 after each cycle, but at a much lower rate than pure ceria. The samples with 10% and 20% Sm doping follow very similar trends (as seen in Figure 6.8, they are almost parallel): first a moderate increase in T50 after 3 or 4 cycles, followed by a near plateauing of T50. The differences in T50 between initial and plateau values are 17°C for 10% Sm and 8°C for 20% Sm. Those results indicate good stability performance for Sm doping above 10%. Considering activity and stability together, 10% Sm-doped catalyst performed better among all catalysts, with comparable stability as for 20% Sm, but with the lowest T50 after 7 cycles (412°C).

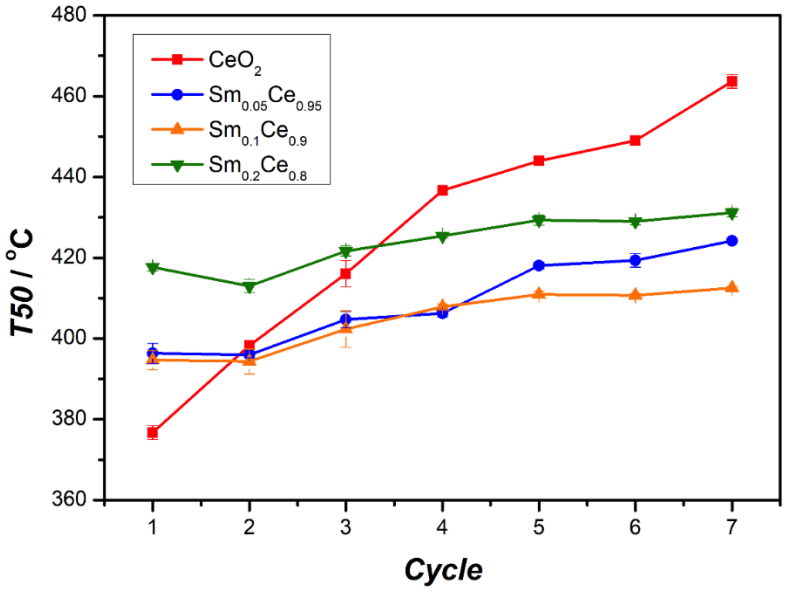

Figure 6.8. Stability of Sm-doped CeO_2 for soot oxidation

Figure 6.9 shows the relation between change of T50 (between first and 7th cycle) and Sm doping ratio. Spent CeO_2 catalyst led to 64°C change in T50, compared to fresh one. T50 of 5% and 10% Sm-doped catalysts show smaller differences, which are about 31°C and 19°C, respectively. T50

for 20% Sm-doped catalyst showed the lowest difference (13°C). It is clear that T50 difference reduces with higher Sm doping, indicating that richer Sm contributes to a more stable catalyst, albeit with lower activity.

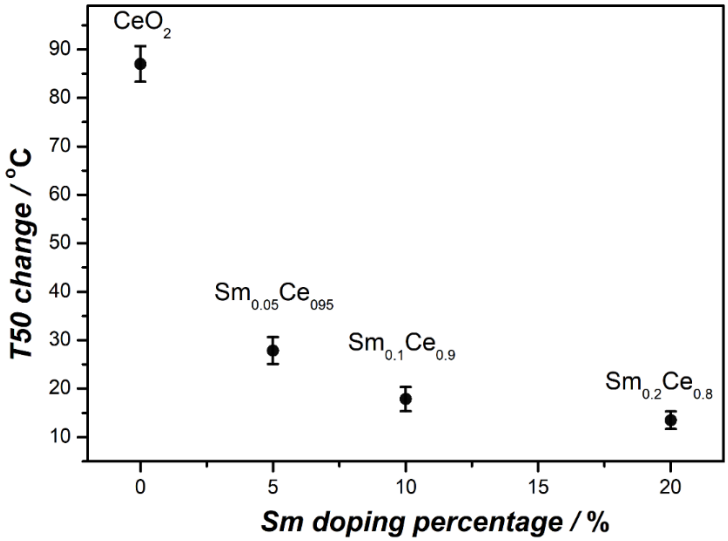

Figure 6.9. Relation ΔT50 and Sm doping ratio

As discussed previously, Ce^{3+} content plays an important role for catalyst activity towards soot oxidation. Figure 6.10 illustrates the relation between Ce^{3+} content change (between first and 5th cycle) and Sm doping ratio. This figure indicates that addition of Sm (even at 5%) results in a significant decrease in the change of Ce^{3+} between fresh and spent catalysts. Ce^{3+} content for pure ceria decreases from 23.8% to 13.8%, indicative of poor stability performance. In contrast, Sm-doped ceria catalysts exhibit change in Ce^{3+} content below 1%, with 20% Sm doping only 0.4% change. This is why Sm-doped catalysts show higher activity after 5 cycles (or more) than pure ceria.

Figure 6.10 shows the relation between change of O_α percentage (between first and 5^{th} cycle) and Sm doping ratio. It is observed that with increasing the doping ratio, the decrease of O_α percentage became smaller. The 5% and 10% Sm-doped catalysts decreased by about 2%, whereas the 20% Sm catalyst did not show any change. This suggests that higher Sm doping makes a more stable catalyst and prevent the decline of O_α percentage. The O_α percentage of fresh CeO_2 catalyst is 39.6% and yields to 29.5% after 5 cycles. This indicates that the OSC of CeO_2 catalysts is not stable, and the significant decline of OSC after reacting with soot demonstrates a poor stability of pure ceria catalysts.

XRD results have shown that Sm is incorporated into CeO_2 lattice and causes lattice expansion. The increased crystal size of the spent catalyst compared with the fresh one indicates that re-crystallization occurred. However, the larger crystal size does not benefit the catalyst activity towards soot oxidation, as smaller crystal size could favor oxygen diffusion and provide more contact points. Sm-doped catalyst showed smaller change in crystal size after reactions, and such difference become lesser with higher amounts of Sm doping, indicating that adding Sm can inhibit this re-crystallization process. Therefore, adding Sm can stabilize the catalyst crystal structure and maintain surface properties such as Ce^{3+} and O_α percentage.

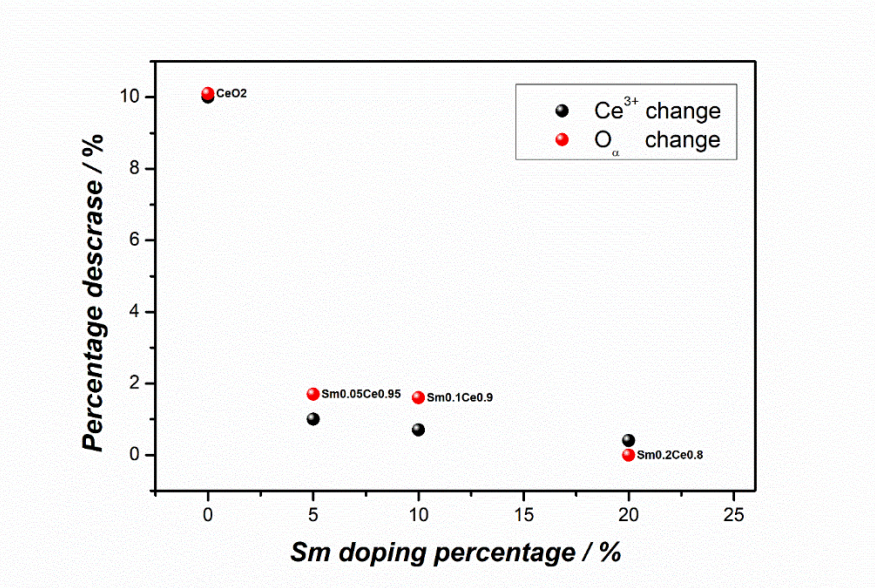

Figure 6.10. Relation between Ce^{3+}/O_{α} change and Sm doping ratio

6.4.4 Stability tests for Fe and Sm co-doped CeO_2 catalysts

So far in Chapter 6, the addition of Sm (at least 10% Sm) into ceria leads to more stable catalysts, but at the expense of lowering the activity. In Chapter 5, it was found that for fresh catalyst, 5% Fe-doped ceria made by SCS method performed better than pure CeO_2. It is, therefore, a logical step to consider co-doping of Fe and Sm on CeO_2. The $Sm_{0.2}Ce_{0.8}$ catalyst was chosen because it showed best stability. Herein, 20% Sm was introduced into 5% Fe doped CeO_2 catalysts to increase its stability, and TGA tests were performed for five cycles. Figure 6.11 shows the stability results of Fe-Sm-doped CeO_2 for soot oxidation. For comparison, Fe-CeO_2 and $Sm_{0.2}Ce_{0.8}$ are also shown in this Figure. During the 5 cycles, T50 still showed the trend of direct increase with number of recycles. It was found that although $Sm_{0.2}Ce_{0.8}$ is stable, it loses its stability by adding 5% Fe and becomes similar to the performance of Fe-CeO_2.

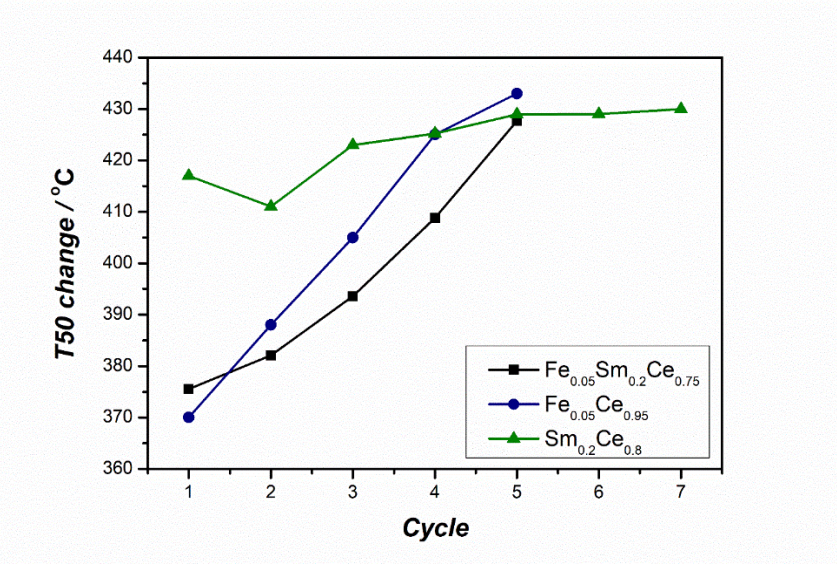

Figure 6.11. Stability of Fe and Sm-doped CeO_2 for soot oxidation

6.5. Summary

- Doping 5%, 10% and 20% samarium into CeO_2 lattice improve the stability of ceria-based catalyst for soot oxidation. In particular, at higher Sm content (10% and 20%), the reactivity (represented by T50) nearly plateaus after 5 cycles. However, increasing Sm content decreases activity for soot oxidation (after 7 cycles, T50 is 413°C for 10% Sm and 431°C for 20% Sm).

- Considering stability and activity together, 10% Sm-doped catalyst showed the best compromise between stability and activity.

- Ce^{3+} and O_α played the most important role in controlling catalytic soot oxidation activity, because they are directly related to oxygen vacancies and oxygen storage capacity of the catalyst. Sm-doping catalysts, especially at 10% and 20% Sm, show minimum decrease in

Ce^{3+} content (4.0 and 2.6% for 10% and 20% Sm, respectively) and O_α percentage (4.1 and 0% for 10% and 20% Sm, respectively) between fresh and spent catalysts after 5 cycles.

- Higher stability in crystal size between fresh and spent catalysts can also explain the greater stability for Sm doped ceria catalysts. However, from activity of the fresh catalyst, the results did not indicate a clear correlation between crystal size and activity for both fresh and spent catalysts. Therefore, crystal size growth is not considered here as the most important parameter for catalyst deactivation, unlike in most studies that looked at catalyst activity from accelerated thermal aging point of view.

- Finally, although addition of Fe on 20% Sm doped ceria catalyst did improve the activity in early cycles, it shows poor stability.

Chapter 7: Conclusions and Recommendations

7.1. Conclusions

The focus of this thesis is to improve catalytic activity and stability of ceria-based catalysts for soot oxidation. The main objective was to develop an inexpensive, active and stable catalyst through iron and samarium doping. The role of iron and samarium doping towards improving catalytic activity and stability was elucidated through nano (in-situ ETEM) and bulk (TGA) scales investigations, along with a suite of characterization techniques. The main conclusions drawn from this work are as follows:

- The ETEM study showed that both catalyst and carbon particles can be mobile. The relative mobility of these particles appears to be correlated to the size of particles. It was found that reaction rates were positively correlated to the contact length between carbon and catalyst particles, thus indicating that catalytic carbon oxidation occurs at the carbon/catalyst interface. Larger normalized reaction rates lead to higher movement velocity, suggesting that the mobility is caused by carbon oxidation on the catalyst's surface. These data also showed that both normalized rate and movement velocity increase when the temperature and the oxygen partial pressure increase. DFT calculations indicate that O-C bonding is likely an important contributor to the strong interactions between the Fe/CeO_2 catalyst and carbon particles during the oxidation reactions, thereby driving the relative mobility of catalyst and carbon particles.

- For the two fabrication methods investigated, co-precipitation (CP) and solution combustion synthesis (SCS), there is an optimum Fe content that gives the highest activity. For SCS catalyst, the optimum Fe content is 5%, and for CP catalyst, it is 10%. Irrespective of the

fabrication method, the most important parameter that dictates the reaction activity (e.g. T50) is the Ce^{3+} content, which is closely related to the content of oxygen vacancies. The activity increases notably when Ce^{3+} content increases up to 20%. Above 20% Ce^{3+} content, the activity increases moderately. The pore size is mostly about 3-5 nm (both CP and SCS), which is much smaller than the 25 nm soot particles used here. This is why, although the BET surface area is greater for CP than SCS, it has only moderate effect on the activity.

- It is well known that pure ceria possesses poor stability performance and thus, inspired by the work on SOFC, samarium doped ceria was considered as a promising candidate for stable ceria-based catalysts for soot oxidation because Sm can help form stable fluorite crystal structure. It was found that samarium doping indeed improves the stability of ceria-based catalyst for soot oxidation. In particular, at higher Sm content (10% and 20%), the reactivity (represented by T50) nearly plateaus after 5 cycles. However, increasing Sm content decreases activity for soot oxidation. The 10% Sm-doped catalyst showed the best compromise between stability and activity. It was found that Ce^{3+} and O_α played the most important role in controlling catalytic soot oxidation activity, because they are directly related to oxygen vacancies and oxygen storage capacity of the catalyst. Sm-doping catalysts, especially at 10% and 20% Sm, show minimum decrease in Ce^{3+} content and O_α percentage between fresh and spent catalysts after 5 cycles. Crystal size growth over several cycles was not found as the most important parameter for catalyst deactivation, unlike in most studies that looked at catalyst activity from accelerated thermal aging point of view. Finally, although addition of Fe on 20% Sm doped ceria catalyst did improve the activity in early cycles, it showed poor stability, which was unexpected.

7.2. Recommendations

This research presents a promising step to improving the activity and stability of catalyst for soot oxidation. It also provides an understanding of the influence of different metal doping ratio and preparation methods towards catalytic soot oxidation. Nevertheless, there are still many challenges for the development of ceria-based catalyst with good activity and stability.

- The first challenge is to increase the activity of the stable 10-20% Sm-doped ceria catalyst. Our first attempt by adding 5% Fe failed in term of stability; further work is needed to understand the deactivation mechanism and to possibly alternative doping solutions.
- The second challenge is to consider more realistic conditions with the presence of SO_x and NO_x on catalyst activity and stability.
- Finally, activity and stability experiments must be carried out under real DPF coated with newly developed catalyst for soot oxidation.

References

[1] S. Menon, J. Hansen, L. Nazarenko, Y. Luo, Climate effects of black carbon aerosols in China and India, Science, 297 (2002) 2250-2253.

[2] M.C. Turner, D. Krewski, C.A. Pope, 3rd, Y. Chen, S.M. Gapstur, M.J. Thun, Long-term ambient fine particulate matter air pollution and lung cancer in a large cohort of never-smokers, Am J Respir Crit Care Med, 184 (2011) 1374-1381.

[3] T.C. Bond, S.J. Doherty, D.W. Fahey, P.M. Forster, T. Berntsen, B.J. DeAngelo, M.G. Flanner, S. Ghan, B. Kärcher, D. Koch, Bounding the role of black carbon in the climate system: A scientific assessment, Journal of Geophysical Research: Atmospheres, 118 (2013) 5380-5552.

[4] T. Andana, M. Piumetti, S. Bensaid, N. Russo, D. Fino, R. Pirone, Nanostructured ceria-praseodymia catalysts for diesel soot combustion, Applied Catalysis B: Environmental, 197 (2016) 125-137.

[5] P. Venkataswamy, D. Jampaiah, K.N. Rao, B.M. Reddy, Nanostructured $Ce_{0.7}Mn_{0.3}O_{2-\delta}$ and $Ce_{0.7}Fe_{0.3}O_{2-\delta}$ solid solutions for diesel soot oxidation, Applied Catalysis A: General, 488 (2014) 1-10.

[6] https://atct.anl.gov/Thermochemical Data/version 1.118/species/?species_number=19.

[7] J.P.A. Neeft, M. Makkee, J.A. Moulijn, Diesel particulate emission control, Fuel Processing Technology, 47 (1996) 1-69.

[8] A. Bueno-López, Diesel soot combustion ceria catalysts, Applied Catalysis B: Environmental, 146 (2014) 1-11.

[9] J. Oi-Uchisawa, A. Obuchi, S. Wang, T. Nanba, A. Ohi, Catalytic performance of Pt/MOx loaded over SiC-DPF for soot oxidation, Applied Catalysis B: Environmental, 43 (2003) 117-129.

[10] C.A. Neyertz, E.D. Banús, E.E. Miró, C.A. Querini, Potassium-promoted $Ce_{0.65}Zr_{0.35}O_2$ monolithic catalysts for diesel soot combustion, Chemical Engineering Journal, 248 (2014) 394-405.

[11] R. Burch, Knowledge and Know-How in Emission Control for Mobile Applications, Catalysis Reviews, 46 (2004) 271-334.

[12] A. Russell, W.S. Epling, Diesel Oxidation Catalysts, Catalysis Reviews, 53 (2011) 337-423.

[13] D. Fino, S. Bensaid, M. Piumetti, N. Russo, A review on the catalytic combustion of soot in Diesel particulate filters for automotive applications: From powder catalysts to structured reactors,

Applied Catalysis A: General, 509 (2016) 75-96.
[14] P. Eastwood, Critical topics in exhaust gas aftertreatment, 2000.
[15] Diesel Particulate Filter (DPF) technology, channels are sealed at the inlet in a chessboard manner (Johnson Matthey).
[16] S.M. Platt, I. El Haddad, S.M. Pieber, A.A. Zardini, R. Suarez-Bertoa, M. Clairotte, K.R. Daellenbach, R.J. Huang, J.G. Slowik, S. Hellebust, B. Temime-Roussel, N. Marchand, J. de Gouw, J.L. Jimenez, P.L. Hayes, A.L. Robinson, U. Baltensperger, C. Astorga, A.S.H. Prévôt, Gasoline cars produce more carbonaceous particulate matter than modern filter-equipped diesel cars, Scientific Reports, 7 (2017) 4926.
[17] K. Mori, K. Watanabe, T. Sato, H. Yamashita, Environmental Transmission Electron Microscopy Study of Diesel Carbon Soot Combustion under Simulated Catalytic-Reaction Conditions, Chemphyschem : a European journal of chemical physics and physical chemistry, 16 (2015) 1347-1351.
[18] M.K. Khair, A Review of Diesel Particulate Filter Technologies, Society of Automotive Engineering, Inc.2003.
[19] B.M. Reddy, K.N. Rao, Copper promoted ceria–zirconia based bimetallic catalysts for low temperature soot oxidation, Catalysis Communications, 10 (2009) 1350-1353.
[20] S.B. Simonsen, S. Dahl, E. Johnson, S. Helveg, Ceria-catalyzed soot oxidation studied by environmental transmission electron microscopy, Journal of Catalysis, 255 (2008) 1-5.
[21] S.B. Simonsen, In situ studies of CeO_2-catalyzed soot oxidation by means of Environmental Transmission Electron Microscopy, University of Copenhagen, 2008.
[22] S. Liu, X. Wu, D. Weng, R. Ran, Ceria-based catalysts for soot oxidation: a review, Journal of Rare Earths, 33 (2015) 567-590.
[23] D.J. Perala Venkataswamy, Komateedi N. Rao, Benjaram M. Reddy, Nanostructured $Ce_{0.7}Mn_{0.3}O_{2-\delta}$ and $Ce_{0.7}Fe_{0.3}O_{2-\delta}$ solid solutions for diesel soot oxidation, Applied Catalysis A: General, 488 (2014) 1-10.
[24] Y. Wei, Z. Zhao, J. Liu, C. Xu, G. Jiang, A. Duan, Design and Synthesis of 3D Ordered Macroporous CeO_2-Supported Pt@ $CeO_{2-\delta}$ Core–Shell Nanoparticle Materials for Enhanced Catalytic Activity of Soot Oxidation, Small, 9 (2013) 3957-3963.
[25] A. Bueno-López, K. Krishna, B. van der Linden, G. Mul, J.A. Moulijn, M. Makkee, On the mechanism of model diesel soot-O_2 reaction catalysed by Pt-containing La^{3+}-doped CeO_2: A TAP

study with isotopic O_2, Catalysis Today, 121 (2007) 237-245.
[26] P.W. Dunne, A.M. Carnerup, A. Węgrzyn, S. Witkowski, R.I. Walton, Hierarchically Structured Ceria-Silica: Synthesis and Thermal Properties, The Journal of Physical Chemistry C, 116 (2012) 13435-13445.
[27] L. Katta, P. Sudarsanam, G. Thrimurthulu, B.M. Reddy, Doped nanosized ceria solid solutions for low temperature soot oxidation: Zirconium versus lanthanum promoters, Applied Catalysis B: Environmental, 101 (2010) 101-108.
[28] J. Liu, Z. Zhao, J. Wang, C. Xu, A. Duan, G. Jiang, Q. Yang, The highly active catalysts of nanometric CeO_2-supported cobalt oxides for soot combustion, Applied Catalysis B: Environmental, 84 (2008) 185-195.
[29] Z. Zhang, D. Han, S. Wei, Y. Zhang, Determination of active site densities and mechanisms for soot combustion with O2 on Fe-doped CeO2 mixed oxides, Journal of Catalysis, 276 (2010) 16-23.
[30] J. Liu, Z. Zhao, J. Wang, C. Xu, A. Duan, G. Jiang, Q. Yang, The highly active catalysts of nanometric CeO_2-supported cobalt oxides for soot combustion, Applied Catalysis B: Environmental, 84 (2008) 185-195.
[31] H. Muroyama, S. Hano, T. Matsui, K. Eguchi, Catalytic soot combustion over CeO_2-based oxides, Catalysis Today, 153 (2010) 133-135.
[32] X. Li, S. Wei, Z. Zhang, Y. Zhang, Z. Wang, Q. Su, X. Gao, Quantification of the active site density and turnover frequency for soot combustion with O_2 on Cr doped CeO_2, Catalysis Today, 175 (2011) 112-116.
[33] H. Li, K. Li, H. Wang, X. Zhu, Y. Wei, D. Yan, X. Cheng, K. Zhai, Soot combustion over $Ce_{1-x}Fe_xO_{2-\delta}$ and CeO_2/Fe_2O_3 catalysts: Roles of solid solution and interfacial interactions in the mixed oxides, Applied Surface Science, 390 (2016) 513-525.
[34] E. Aneggi, C. de Leitenburg, G. Dolcetti, A. Trovarelli, Promotional effect of rare earths and transition metals in the combustion of diesel soot over CeO_2 and CeO_2–ZrO_2, Catalysis Today, 114 (2006) 40-47.
[35] S. Wagloehner, S. Kureti, Study on the mechanism of the oxidation of soot on Fe_2O_3 catalyst, Applied Catalysis B: Environmental, 125 (2012) 158-165.
[36] I. Atribak, F.E. López-Suárez, A. Bueno-López, A. García-García, New insights into the performance of ceria–zirconia mixed oxides as soot combustion catalysts. Identification of the role

of “active oxygen” production, Catalysis today, 176 (2011) 404-408.
[37] L. Sui, Y. Wang, H. Kang, H. Dong, L. Dong, L. Yu, Effect of Cs–Ce–Zr Catalysts/Soot Contact Conditions on Diesel Soot Oxidation, ACS Omega, 2 (2017) 6984-6990.
[38] J.P.A. Neeft, M. Makkee, J.A. Moulijn, Catalysts for the oxidation of soot from diesel exhaust gases. I. An exploratory study, Applied Catalysis B: Environmental, 8 (1996) 57-78.
[39] D. Terribile, A. Trovarelli, C. de Leitenburg, A. Primavera, G. Dolcetti, Catalytic combustion of hydrocarbons with Mn and Cu-doped ceria–zirconia solid solutions, Catalysis Today, 47 (1999) 133-140.
[40] G. Zhou, P.R. Shah, R.J. Gorte, A study of cerium–manganese mixed oxides for oxidation catalysis, Catalysis Letters, 120 (2008) 191-197.
[41] W. Liu, M. Flytzanistephanopoulos, Total oxidation of carbon monoxide and methane over transition metal fluorite oxide composite catalysts: I. Catalyst composition and activity, Journal of Catalysis, 153 (1995) 304-316.
[42] F. Lin, X. Wu, S. Liu, D. Weng, Y. Huang, Preparation of MnO_x–CeO_2–Al_2O_3 mixed oxides for NO_x-assisted soot oxidation: Activity, structure and thermal stability, Chemical Engineering Journal, 226 (2013) 105-112.
[43] K. Krishna, A. Bueno-López, M. Makkee, J. Moulijn, Potential rare earth modified CeO_2 catalysts for soot oxidation: I. Characterisation and catalytic activity with O_2, Applied Catalysis B: Environmental, 75 (2007) 189-200.
[44] M.A. Małecka, L. Kępiński, W. Miśta, Structure evolution of nanocrystalline CeO_2 and CeLnOx mixed oxides (Ln= Pr, Tb, Lu) in O_2 and H_2 atmosphere and their catalytic activity in soot combustion, Applied Catalysis B: Environmental, 74 (2007) 290-298.
[45] I. Atribak, A.n. Bueno-López, A. García-García, Thermally stable ceria–zirconia catalysts for soot oxidation by O_2, Catalysis Communications, 9 (2008) 250-255.
[46] I. Atribak, A. Bueno-López, A. García-García, Role of yttrium loading in the physico-chemical properties and soot combustion activity of ceria and ceria–zirconia catalysts, Journal of Molecular Catalysis A: Chemical, 300 (2009) 103-110.
[47] D. Fino, Diesel emission control: Catalytic filters for particulate removal, Science and Technology of Advanced Materials, 8 (2007) 93-100.
[48] H. Lüders, P. Stommel, R. Backes, Applications for the regeneration of diesel particulate traps by combining different regeneration systems, SAE Technical Paper, 1997.

[49] A.G. Konstandopoulos, M. Kostoglou, S. Lorentzou, N. Vlachos, Aspects of multifunctional diesel particulate filters and their efficient simulation, Catalysis Today, 188 (2012) 2-13.
[50] G. Blanchard, C. Colignon, C. Griard, C. Rigaudeau, O. Salvat, T. Seguelong, Passenger car series application of a new diesel particulate filter system using a new ceria-based fuel-borne catalyst from the engine test bench to European vehicle certification, SAE TECHNICAL PAPER SERIES, No. 2002-01-2781 (2002).
[51] A.G. Volkswagen, The diesel particulate filter system with additive: design and function, Self-Study Programme 330.
[52] A.G. Konstandopoulos, S. Lorentzou, C. Pagkoura, K. Ohno, K. Ogyu, T.Oya, Sustained soot oxidation in catalytically coated filters, SAE TECHNICAL PAPER SERIES, 2007.
[53] Y.M. Masato Machida, Kouji Kishikawa, Dongjie Zhang, and Keita Ikeue, On the reasons for high activity of CeO2 catalyst for soot oxidation, Chemistry of Materials, 20 (2008) 4489-4494.
[54] D. Jampaiah, K.M. Tur, S.J. Ippolito, Y.M. Sabri, J. Tardio, S.K. Bhargava, B.M. Reddy, Structural characterization and catalytic evaluation of transition and rare earth metal doped ceria-based solid solutions for elemental mercury oxidation, RSC Advances, 3 (2013) 12963-12974.
[55] W. Zhang, X. Niu, L. Chen, F. Yuan, Y. Zhu, Soot Combustion over Nanostructured Ceria with Different Morphologies, Scientific Reports, 6 (2016) 29062.
[56] M.K. Khair, A review of diesel particulate filter technologies, SAE Technical Paper, 2003.
[57] D. Fino, P. Fino, G. Saracco, V. Specchia, Innovative means for the catalytic regeneration of particulate traps for diesel exhaust cleaning, Chemical Engineering Science, 58 (2003) 951-958.
[58] C.G. ïrsmann, Catalytic Coatings for Active and Passive Diesel Particulate Filter Regeneration, Monatshefte für Chemie/Chemical Monthly, 136 (2005) 91-105.
[59] V. Palma, P. Ciambelli, E. Meloni, A. Sin, Catalytic DPF microwave assisted active regeneration, Fuel, 140 (2015) 50-61.
[60] N. Labhsetwar, R. Biniwale, R. Kumar, S. Rayalu, S. Devotta, Application of supported perovskite-type catalysts for vehicular emission control, Catalysis Surveys from Asia, 10 (2006) 55-64.
[61] K. Hinot, Catalytic Soot Oxidation by Platinum on sintered metal filters: Influence of the platinum quantity, particle size and location, and investigation of the platinum-soot contact, Universität Karlsruhe, 2007.
[62] A. Setiabudi, J. Chen, G. Mul, M. Makkee, J.A. Moulijn, CeO_2 catalysed soot oxidation: The

role of active oxygen to accelerate the oxidation conversion, Applied Catalysis B: Environmental, 51 (2004) 9-19.
[63] P. Miceli, S. Bensaid, N. Russo, D. Fino, Effect of the morphological and surface properties of CeO_2-based catalysts on the soot oxidation activity, Chemical Engineering Journal, 278 (2015) 190-198.
[64] E. Aneggi, C. de Leitenburg, A. Trovarelli, Ceria-based formulations for catalysts for diesel soot combustion, Catalysis by Ceria and Related Materials, World Scientific 2013, pp. 565-621.
[65] R.M. Heck, R.J. Farrauto, S.T. Gulati, Catalytic air pollution control: commercial technology, John Wiley & Sons 2009.
[66] H. Gasteiger, J.G. In, Handbook of Heterogeneous Catalysis; ; G. Ertl, H. Knözinger, F. Schüth, J. Weitkamp, Eds, Wiley-VCH Verlag GmbH, 2008.
[67] P. Doggali, H. Kusaba, S. Rayalu, Y. Teraoka, N. Labhsetwar, Bench scale experiments of diesel soot oxidation using $Pr_{0.7}Sr_{0.2}K_{0.1}MnO_3$ perovskite type catalyst coated on ceramic foam filters, Topics in Catalysis, 56 (2013) 457-461.
[68] J. Zhu, A. Thomas, Perovskite-type mixed oxides as catalytic material for NO removal, Applied Catalysis B: Environmental, 92 (2009) 225-233.
[69] C.H. Kim, G. Qi, K. Dahlberg, W. Li, Strontium-doped perovskites rival platinum catalysts for treating NOx in simulated diesel exhaust, Science, 327 (2010) 1624-1627.
[70] Q. Li, M. Meng, N. Tsubaki, X. Li, Z. Li, Y. Xie, T. Hu, J. Zhang, Performance of K-promoted hydrotalcite-derived CoMgAlO catalysts used for soot combustion, NOx storage and simultaneous soot–NOx removal, Applied Catalysis B: Environmental, 91 (2009) 406-415.
[71] B. Sánchez, C. Querini, E. Miró, NOx adsorption and diesel soot combustion over La_2O_3 supported catalysts containing K, Rh and Pt, Applied Catalysis A: General, 366 (2009) 166-175.
[72] N.E. Olong, K. Stöwe, W.F. Maier, HT-search for alkaline-and noble-metal-free mixed oxide catalysts for soot oxidation, Catalysis Today, 137 (2008) 110-118.
[73] X. Zhou, H. Chen, G. Zhang, J. Wang, Z. Xie, Z. Hua, L. Zhang, J. Shi, Cu/Mn co-loaded hierarchically porous zeolite beta: a highly efficient synergetic catalyst for soot oxidation, Journal of Materials Chemistry A, 3 (2015) 9745-9753.
[74] L. Castoldi, R. Matarrese, L. Lietti, P. Forzatti, Intrinsic reactivity of alkaline and alkaline-earth metal oxide catalysts for oxidation of soot, Applied Catalysis B: Environmental, 90 (2009) 278-285.

[75] Y. Nagai, T. Hirabayashi, K. Dohmae, N. Takagi, T. Minami, H. Shinjoh, S.i. Matsumoto, Sintering inhibition mechanism of platinum supported on ceria-based oxide and Pt-oxide–support interaction, Journal of Catalysis, 242 (2006) 103-109.
[76] N. Takagi, T. Minami, T. Hirabayashi, S.i. Matsumoto, K. Dohmae, Y. Nagai, H. Shinjoh, Sintering Mechanism of Platinum Supported on Ceria-Based Oxide for Automotive Catalysts, SAE Technical Paper, 2006.
[77] E. Aneggi, C. de Leitenburg, G. Dolcetti, A. Trovarelli, Diesel soot combustion activity of ceria promoted with alkali metals, Catalysis Today, 136 (2008) 3-10.
[78] X. Wu, D. Liu, K. Li, J. Li, D. Weng, Role of CeO_2–ZrO_2 in diesel soot oxidation and thermal stability of potassium catalyst, Catalysis Communications, 8 (2007) 1274-1278.
[79] M. Peralta, V. Milt, L. Cornaglia, C. Querini, Stability of Ba, K/CeO_2 catalyst during diesel soot combustion: Effect of temperature, water, and sulfur dioxide, Journal of Catalysis, 242 (2006) 118-130.
[80] E. Aneggi, D. Wiater, C. de Leitenburg, J. Llorca, A. Trovarelli, Shape-dependent activity of ceria in soot combustion, Acs Catalysis, 4 (2013) 172-181.
[81] T. Kayama, K. Yamazaki, H. Shinjoh, Nanostructured ceria− silver synthesized in a one-pot redox reaction catalyzes carbon oxidation, Journal of the American Chemical Society, 132 (2010) 13154-13155.
[82] Y. Wei, J. Liu, Z. Zhao, C. Xu, A. Duan, G. Jiang, Structural and synergistic effects of three-dimensionally ordered macroporous $Ce_{0.8}Zr_{0.2}O_2$-supported Pt nanoparticles on the catalytic performance for soot combustion, Applied Catalysis A: General, 453 (2013) 250-261.
[83] P.A. Kumar, M.D. Tanwar, N. Russo, R. Pirone, D. Fino, Synthesis and catalytic properties of CeO_2 and Co/CeO_2 nanofibres for diesel soot combustion, Catalysis Today, 184 (2012) 279-287.
[84] E. Aneggi, C. de Leitenburg, J. Llorca, A. Trovarelli, Higher activity of diesel soot oxidation over polycrystalline ceria and ceria–zirconia solid solutions from more reactive surface planes, Catalysis today, 197 (2012) 119-126.
[85] M. Piumetti, S. Bensaid, N. Russo, D. Fino, Nanostructured ceria-based catalysts for soot combustion: Investigations on the surface sensitivity, Applied Catalysis B: Environmental, 165 (2015) 742-751.
[86] Y. Wei, Z. Zhao, X. Yu, B. Jin, J. Liu, C. Xu, A. Duan, G. Jiang, S. Ma, One-pot synthesis of

core-shell Au@$CeO_{2-\delta}$ nanoparticles supported on three-dimensionally ordered macroporous ZrO_2 with enhanced catalytic activity and stability for soot combustion, Catalysis Science & Technology, 3 (2013) 2958-2970.

[87] Y. Wei, Z. Zhao, J. Liu, S. Liu, C. Xu, A. Duan, G. Jiang, Multifunctional catalysts of three-dimensionally ordered macroporous oxide-supported Au@ Pt core–shell nanoparticles with high catalytic activity and stability for soot oxidation, Journal of Catalysis, 317 (2014) 62-74.

[88] K. Yamazaki, T. Kayama, F. Dong, H. Shinjoh, A mechanistic study on soot oxidation over CeO_2–Ag catalyst with 'rice-ball'morphology, Journal of catalysis, 282 (2011) 289-298.

[89] Y. Wei, J. Liu, Z. Zhao, A. Duan, G. Jiang, The catalysts of three-dimensionally ordered macroporous $Ce_{1-x}Zr_xO_2$-supported gold nanoparticles for soot combustion: The metal–support interaction, Journal of Catalysis, 287 (2012) 13-29.

[90] G. Zhang, Z. Zhao, J. Liu, G. Jiang, A. Duan, J. Zheng, S. Chen, R. Zhou, Three dimensionally ordered macroporous $Ce_{1-x}Zr_xO_2$ solid solutions for diesel soot combustion, Chemical Communications, 46 (2010) 457-459.

[91] G. Zhang, Z. Zhao, J. Xu, J. Zheng, J. Liu, G. Jiang, A. Duan, H. He, Comparative study on the preparation, characterization and catalytic performances of 3DOM Ce-based materials for the combustion of diesel soot, Applied Catalysis B: Environmental, 107 (2011) 302-315.

[92] Y. Wei, Z. Zhao, T. Li, J. Liu, A. Duan, G. Jiang, The novel catalysts of truncated polyhedron Pt nanoparticles supported on three-dimensionally ordered macroporous oxides (Mn, Fe, Co, Ni, Cu) with nanoporous walls for soot combustion, Applied Catalysis B: Environmental, 146 (2014) 57-70.

[93] J. Liu, Z. Zhao, Y. Chen, C. Xu, A. Duan, G. Jiang, Different valent ions-doped cerium oxides and their catalytic performances for soot oxidation, Catalysis today, 175 (2011) 117-123.

[94] W. Yuechang, Z. Zhen, J. Jinqing, L. Jian, D. Aijun, G. JIANG, Preparation of ultrafine Ce-based oxide nanoparticles and their catalytic performances for diesel soot combustion, Journal of Rare Earths, 32 (2014) 124-130.

[95] J. Liu, Z. Zhao, C. Xu, A. Duan, L. Wang, S. Zhang, Synthesis of nanopowder Ce–Zr–Pr oxide solid solutions and their catalytic performances for soot combustion, Catalysis Communications, 8 (2007) 220-224.

[96] S. Bensaid, N. Russo, D. Fino, CeO_2 catalysts with fibrous morphology for soot oxidation: The importance of the soot–catalyst contact conditions, Catalysis Today, 216 (2013) 57-63.

[97] P.A. Kumar, M. Tanwar, S. Bensaid, N. Russo, D. Fino, Soot combustion improvement in diesel particulate filters catalyzed with ceria nanofibers, Chemical engineering journal, 207 (2012) 258-266.
[98] E. Bruneel, J. Van Brabant, M. Le, I. Van Driessche, Deposition of a Cu/Mo/Ce catalyst for diesel soot oxidation on a sintered metal fiber filter with a CeO_2 anti corrosion coating, Catalysis Communications, 25 (2012) 111-117.
[99] F. Tuler, E. Banús, M. Zanuttini, E. Miró, V. Milt, Ceramic papers as flexible structures for the development of novel diesel soot combustion catalysts, Chemical Engineering Journal, 246 (2014) 287-298.
[100] J.M. Thomas, R. Raja, Mono-, Bi- and Multifunctional Single-Sites: Exploring the Interface Between Heterogeneous and Homogeneous Catalysis, Topics in Catalysis, 53 (2010) 848-858.
[101] K. An, G.A. Somorjai, Nanocatalysis I: Synthesis of Metal and Bimetallic Nanoparticles and Porous Oxides and Their Catalytic Reaction Studies, Catalysis Letters, 145 (2015) 233-248.
[102] P. Palmisano, N. Russo, P. Fino, D. Fino, C. Badini, High catalytic activity of SCS-synthesized ceria towards diesel soot combustion, Applied Catalysis B: Environmental, 69 (2006) 85-92.
[103] A.C. Lluís Soler, Carlos Escudero, Virginia PØrez-Dieste, Eleonora Aneggi, Alessandro Trovarelli, and Jordi Llorca, Ambient pressure photoemission spectroscopy reveals the mechanism of carbon soot oxidation in ceria-based catalysts, ChemCatChem, 8 (2016) 2748 – 2751.
[104] H. Wang, S. Luo, M. Zhang, W. Liu, X. Wu, S. Liu, Roles of oxygen vacancy and O_x^- in oxidation reactions over CeO_2 and Ag/CeO_2 nanorod model catalysts, Journal of catalysis, 368 (2018) 365-378.
[105] D. Harshini, D.H. Lee, J. Jeong, Y. Kim, S.W. Nam, H.C. Ham, J.H. Han, T.-H. Lim, C.W. Yoon, Enhanced oxygen storage capacity of $Ce_{0.65}Hf_{0.25}M_{0.1}O_{2-\delta}$ (M= rare earth elements): Applications to methane steam reforming with high coking resistance, Applied Catalysis B: Environmental, 148 (2014) 415-423.
[106] E. Lim, Y.J. Kim, J.H. Kim, T. Ryu, S. Lee, B.K. Cho, I.-S. Nam, J.W. Choung, S. Yoo, NO oxidation activity of Ag-doped perovskite catalysts, Journal of catalysis, 319 (2014) 182-193.
[107] B. Liu, C. Li, G. Zhang, X. Yao, S.S. Chuang, Z. Li, Oxygen vacancy promoting dimethyl carbonate synthesis from CO_2 and methanol over Zr-doped CeO_2 nanorods, ACS Catalysis, 8 (2018) 10446-10456.

[108] M. Dhakad, T. Mitshuhashi, S. Rayalu, P. Doggali, S. Bakardjiva, J. Subrt, D. Fino, H. Haneda, N. Labhsetwar, Co_3O_4–CeO_2 mixed oxide-based catalytic materials for diesel soot oxidation, Catalysis today, 132 (2008) 188-193.
[109] K.-i. Shimizu, H. Kawachi, A. Satsuma, Study of active sites and mechanism for soot oxidation by silver-loaded ceria catalyst, Applied Catalysis B: Environmental, 96 (2010) 169-175.
[110] A. Soldati, M. Campolo, F. Sbrizzai, Modeling nano-particle deposition in diesel engine filters, Chemical Engineering Science, 65 (2010) 6443-6451.
[111] S. Bensaid, D. Marchisio, D. Fino, G. Saracco, V. Specchia, Modelling of diesel particulate filtration in wall-flow traps, Chemical Engineering Journal, 154 (2009) 211-218.
[112] V. Di Sarli, A. Di Benedetto, Modeling and simulation of soot combustion dynamics in a catalytic diesel particulate filter, Chemical Engineering Science, 137 (2015) 69-78.
[113] S. Bensaid, D.L. Marchisio, D. Fino, Numerical simulation of soot filtration and combustion within diesel particulate filters, Chemical Engineering Science, 65 (2010) 357-363.
[114] S.B. Simonsen, K. Agersted, K.V. Hansen, T. Jacobsen, J.B. Wagner, T.W. Hansen, L.T. Kuhn, Environmental TEM study of the dynamic nanoscaled morphology of NiO/YSZ during reduction, Applied Catalysis A: General, 489 (2015) 147-154.
[115] A.D. Sediako, C. Soong, J.Y. Howe, M.R. Kholghy, M.J. Thomson, Real-time observation of soot aggregate oxidation in an Environmental Transmission Electron Microscope, Proceedings of the Combustion Institute, (2016).
[116] K. Kamatani, K. Higuchi, Y. Yamamoto, S. Arai, N. Tanaka, M. Ogura, Direct observation of catalytic oxidation of particulate matter using in situ TEM, Scientific Reports, 5 (2015) 10161.
[117] Y. Gao, X. Wu, S. Liu, M. Ogura, M. Liu, D. Weng, Aggregation and redispersion of silver species on alumina and sulphated alumina supports for soot oxidation, Catalysis Science & Technology, 7 (2017) 3524-3530.
[118] R.T.K. Baker, In Situ Electron Microscopy Studies of Catalyst Particle Behavior, Catalysis Reviews, 19 (1979) 161-209.
[119] R.T.K. Baker, J.A. France, L. Rouse, R.J. Waite, Catalytic oxidation of graphite by platinum and palladium, Journal of Catalysis, 41 (1976) 22-29.
[120] A. Serve, T. Epicier, M. Aouine, F.J. Cadete Santos Aires, E. Obeid, M. Tsampas, K. Pajot, P. Vernoux, Investigations of soot combustion on yttria-stabilized zirconia by environmental transmission electron microscopy (ETEM), Applied Catalysis A: General, 504 (2015) 74-80.

[121] Q. Liang, X. Wu, D. Weng, Z. Lu, Selective oxidation of soot over Cu doped ceria/ceria–zirconia catalysts, catalysis communications, 9 (2008) 202-206.

[122] S. Liu, X. Wu, W. Liu, W. Chen, R. Ran, M. Li, D. Weng, Soot oxidation over CeO_2 and Ag/CeO_2: Factors determining the catalyst activity and stability during reaction, Journal of catalysis, 337 (2016) 188-198.

[123] G. Corro, A. Flores, F. Pacheco-Aguirre, U. Pal, F. Bañuelos, A. Ramirez, A. Zehe, Biodiesel and fossil-fuel diesel soot oxidation activities of Ag/CeO_2 catalyst, Fuel, 250 (2019) 17-26.

[124] Y. Gao, A. Duan, S. Liu, X. Wu, W. Liu, M. Li, S. Chen, X. Wang, D. Weng, Study of $Ag/Ce_xNd_{1-x}O_2$ nanocubes as soot oxidation catalysts for gasoline particulate filters: Balancing catalyst activity and stability by Nd doping, Applied Catalysis B: Environmental, 203 (2017) 116-126.

[125] L. Xiong, P. Yao, S. Liu, S. Li, J. Deng, Y. Jiao, Y. Chen, J. Wang, Soot oxidation over CeO_2-ZrO_2 based catalysts: The influence of external surface and low-temperature reducibility, Molecular Catalysis, 467 (2019) 16-23.

[126] H. Zhang, J. Wang, Y. Cao, Y. Wang, M. Gong, Y. Chen, Effect of Y on improving the thermal stability of MnO_x-CeO_2 catalysts for diesel soot oxidation, Chinese Journal of Catalysis, 36 (2015) 1333-1341.

[127] H. Zhang, S. Yuan, J. Wang, M. Gong, Y. Chen, Effects of contact model and NO_x on soot oxidation activity over Pt/MnO_x-CeO_2 and the reaction mechanisms, Chemical Engineering Journal, 327 (2017) 1066-1076.

[128] M.A. Peralta, M.S. Zanuttini, C.A. Querini, Activity and stability of $BaKCo/CeO_2$ catalysts for diesel soot oxidation, Applied Catalysis B: Environmental, 110 (2011) 90-98.

[129] M. Kurnatowska, W. Mista, P. Mazur, L. Kepinski, Nanocrystalline $Ce_{1-x}Ru_xO_2$ Microstructure, stability and activity in CO and soot oxidation, Applied Catalysis B: Environmental, 148 (2014) 123-135.

[130] S. Wenjuan, Y. Lihua, M. Na, Y. Jiali, Catalytic activity and stability of K/CeO_2 catalysts for diesel soot oxidation, Chinese Journal of Catalysis, 33 (2012) 970-976.

[131] S. Li, S. Yan, Y. Xia, B. Cui, Y. Pu, Y. Ye, D. Wang, Y.-Q. Liu, B. Chen, Oxidative reactivity enhancement for soot combustion catalysts by co-doping silver and manganese in ceria, Applied Catalysis A: General, 570 (2019) 299-307.

[132] L.F. Nascimento, J.F. Lima, P.C. de Sousa Filho, O.A. Serra, Effect of lanthanum loading

on nanosized CeO_2-ZnO solid catalysts supported on cordierite for diesel soot oxidation, Journal of Environmental Sciences, 73 (2018) 58-68.
[133] S.J. Kim, S.W. Kim, Y.M. Park, K.J. Kim, G.M. Choi, Effect of Gd-doped ceria interlayer on the stability of solid oxide electrolysis cell, Solid State Ionics, 295 (2016) 25-31.
[134] H.-F. Lu, Y. Zhou, W.-F. Han, H.-F. Huang, Y.-F. Chen, High thermal stability of ceria-based mixed oxide catalysts supported on ZrO_2 for toluene combustion, Catalysis Science & Technology, 3 (2013) 1480-1484.
[135] Q. Dai, X. Wang, G. Lu, Low-temperature catalytic combustion of trichloroethylene over cerium oxide and catalyst deactivation, Applied Catalysis B: Environmental, 81 (2008) 192-202.
[136] H.-L. Zhang, Y. Zhu, S.-D. Wang, M. Zhao, M.-C. Gong, Y.-Q. Chen, Activity and thermal stability of $Pt/Ce_{0.64}Mn_{0.16}R_{0.2}O_x$ (R= Al, Zr, La, or Y) for soot and NO oxidation, Fuel processing technology, 137 (2015) 38-47.
[137] K. Polychronopoulou, A.F. Zedan, M. Katsiotis, M. Baker, A. AlKhoori, S.Y. AlQaradawi, S. Hinder, S. AlHassan, Rapid microwave assisted sol-gel synthesis of CeO_2 and $Ce_xSm_{1-x}O_2$ nanoparticle catalysts for CO oxidation, Molecular Catalysis, 428 (2017) 41-55.
[138] S. Mandal, K.K. Bando, C. Santra, S. Maity, O.O. James, D. Mehta, B. Chowdhury, Sm-CeO_2 supported gold nanoparticle catalyst for benzyl alcohol oxidation using molecular O_2, Applied Catalysis A: General, 452 (2013) 94-104.
[139] W. Wattanathana, C. Veranitisagul, S. Wannapaiboon, W. Klysubun, N. Koonsaeng, A. Laobuthee, Samarium doped ceria (SDC) synthesized by a metal triethanolamine complex decomposition method: characterization and an ionic conductivity study, Ceramics International, 43 (2017) 9823-9830.
[140] A.B. Stambouli, E. Traversa, Solid oxide fuel cells (SOFCs): a review of an environmentally clean and efficient source of energy, Renewable and sustainable energy reviews, 6 (2002) 433-455.
[141] A. Nechache, M. Cassir, A. Ringuedé, Solid oxide electrolysis cell analysis by means of electrochemical impedance spectroscopy: A review, Journal of Power Sources, 258 (2014) 164-181.
[142] P. Sudarsanam, K. Kuntaiah, B.M. Reddy, Promising ceria–samaria-based nano-oxides for low temperature soot oxidation: a combined study of structure–activity properties, New Journal of Chemistry, 38 (2014) 5991-6001.

[143] A.P. Anantharaman, J. Geethu, H.P. Dasari, J.-H. Lee, H. Dasari, G.U.B. Babu, Ceria-samarium binary metal oxides: A comparative approach towards structural properties and soot oxidation activity, Molecular Catalysis, 451 (2018) 247-254.
[144]http://www.markwellmarine.com.au/products/electron-ion-and-probe microscopy/transmission-electron-microscopes/hf-3300-300-kv-.
[145] Q. Li, X. Wang, Y. Xin, Z. Zhang, Y. Zhang, C. Hao, M. Meng, L. Zheng, L. Zheng, A unified intermediate and mechanism for soot combustion on potassium-supported oxides, Scientific Reports, 4 (2014) 4725.
[146] B.L.J.W.A.R.E. Croiset, Iron Doping in Nanostructured Ceria Catalysts with Different Morphologies for Soot Oxidation, Submitted to Appplied Catalyst B: Environment, (2017).
[147] D. Gardini, J.M. Christensen, C.D. Damsgaard, A.D. Jensen, J.B. Wagner, Visualizing the mobility of silver during catalytic soot oxidation, Applied Catalysis B: Environmental, 183 (2016) 28-36.
[148] H. Wang, C. Chen, Y. Zhang, L. Peng, S. Ma, T. Yang, H. Guo, Z. Zhang, D.S. Su, J. Zhang, In situ oxidation of carbon-encapsulated cobalt nanocapsules creates highly active cobalt oxide catalysts for hydrocarbon combustion, Nature Communications, 6 (2015) 7181.
[149] T. Epicier, Nanoparticles in The ETEM: From Gas-Surface Interactions of Single Objects to Collective Behavior of Nanocatalysts, Microscopy and Microanalysis, 23 (2017) 1850-1851.
[150] M. Piumetti, S. Bensaid, N. Russo, D. Fino, Investigations into nanostructured ceria–zirconia catalysts for soot combustion, Applied Catalysis B: Environmental, 180 (2016) 271-282.
[151] T. Andana, M. Piumetti, S. Bensaid, L. Veyre, C. Thieuleux, N. Russo, D. Fino, E.A. Quadrelli, R. Pirone, CuO nanoparticles supported by ceria for NOx-assisted soot oxidation: insight into catalytic activity and sintering, Applied Catalysis B: Environmental, 216 (2017) 41-58.
[152] G. Kresse, J. Furthmüller, Efficient iterative schemes for ab initio total-energy calculations using a plane-wave basis set, Physical review B, 54 (1996) 11169.
[153] G. Kresse, J. Furthmüller, Efficiency of ab-initio total energy calculations for metals and semiconductors using a plane-wave basis set, Computational materials science, 6 (1996) 15-50.
[154] X. Wang, S. Li, A. Adeosun, Y. Li, M. Vujanović, H. Tan, N. Duić, Effect of potassium-doping and oxygen concentration on soot oxidation in O_2/CO_2 atmosphere: A kinetics study by thermogravimetric analysis, Energy Conversion and Management, 149 (2017) 686-697.

[155] M. Sirignano, H. Ghiassi, A. D'Anna, J.S. Lighty, Temperature and oxygen effects on oxidation-induced fragmentation of soot particles, Combustion and Flame, 171 (2016) 15-26.
[156] H. Ranji-Burachaloo, S. Masoomi-Godarzi, A.A. Khodadadi, Y. Mortazavi, Synergetic effects of plasma and metal oxide catalysts on diesel soot oxidation, Applied Catalysis B: Environmental, 182 (2016) 74-84.
[157] L.F. Hakim, J.H. Blackson, A.W. Weimer, Modification of interparticle forces for nanoparticles using atomic layer deposition, Chemical Engineering Science, 62 (2007) 6199-6211.
[158] M.A. Younjin Min, Kai Kristiansen, Yuval Golan, Jacob Israelachvili, The role of interparticle and external forces in nanoparticle assembly, Nature materials 7, 7 (2008) 527-538.
[159] E.E. Michaelides, Brownian movement and thermophoresis of nanoparticles in liquids, International Journal of Heat and Mass Transfer, 81 (2015) 179-187.
[160] M. Shelef, R.W. McCabe, Twenty-five years after introduction of automotive catalysts: what next?, Catalysis Today, 62 (2000) 35-50.
[161] R.M. Heck, R.J. Farrauto, Automobile exhaust catalysts, Applied Catalysis A: General, 221 (2001) 443-457.
[162] S. Agarwal, L. Lefferts, B.L. Mojet, Ceria nanocatalysts: shape dependent reactivity and formation of OH, ChemCatChem, 5 (2013) 479-489.
[163] Q. Yuan, H.-H. Duan, L.-L. Li, L.-D. Sun, Y.-W. Zhang, C.-H. Yan, Controlled synthesis and assembly of ceria-based nanomaterials, Journal of Colloid and Interface Science, 335 (2009) 151-167.
[164] Y. Wei, Z. Zhao, J. Liu, C. Xu, G. Jiang, A. Duan, Design and Synthesis of 3D Ordered Macroporous CeO_2-Supported Pt@$CeO_{2-\delta}$ Core-Shell Nanoparticle Materials for Enhanced Catalytic Activity of Soot Oxidation, 2013.
[165] Y. Tang, H. Qiao, H. Wang, P. Tao, Nanoparticulate $Mn_{0.3}Ce_{0.7}O_2$: a novel electrocatalyst with improved power performance for metal/air batteries, Journal of Materials Chemistry A, 1 (2013) 12512-12518.
[166] T.R. Sahoo, M. Armandi, R. Arletti, M. Piumetti, S. Bensaid, M. Manzoli, S.R. Panda, B. Bonelli, Pure and Fe-doped CeO_2 nanoparticles obtained by microwave assisted combustion synthesis: Physico-chemical properties ruling their catalytic activity towards CO oxidation and soot combustion, Applied Catalysis B: Environmental, 211 (2017) 31-45.
[167] N. Radutoiu, C. Teodorescu, Satellites in Ce 3d X-Ray Photoelectron Spectroscopy of ceria,

Digest Journal of Nanomaterials & Biostructures (DJNB), 8 (2013).
[168]P. Sudarsanam, B. Mallesham, D.N. Durgasri, B.M. Reddy, Physicochemical characterization and catalytic CO oxidation performance of nanocrystalline Ce–Fe mixed oxides, RSC Advances, 4 (2014) 11322-11330.
[169] W. Wang, Q. Zhu, F. Qin, Q. Dai, X. Wang, Fe doped CeO_2 nanosheets as Fenton-like heterogeneous catalysts for degradation of salicylic acid, Chemical Engineering Journal, 333 (2018) 226-239.
[170] D. Ghosh, R. Biswas, Theoretical calculation of absolute radii of atoms and ions. Part 2. The ionic radii, International Journal of Molecular Sciences, 4 (2003) 379-407.
[171] A. Filtschew, K. Hofmann, C. Hess, Ceria and its defect structure: new insights from a combined spectroscopic approach, The Journal of Physical Chemistry C, 120 (2016) 6694-6703.

Appendix

1. TGA experiments

For comparison with the ETEM experiments, thermogravimetric analysis (TGA) experiments were conducted with a TA Instrument Q500 to study the reaction rate of the catalytic soot oxidation. Every TGA test follows the procedure below: 1) pre-treat 10 mg mixture at 150 ^{0}C under inert gas for 30 min to remove water and other contaminants; 2) heat up the sample to the desired temperature (500, 800°C); 3) isothermal at the specific temperature for 20 min with air.

Reaction rate is calculated based on the equation below:

$$r = -\frac{dm}{dt}$$

Where r is reaction rate, m is the remaining mass of the carbon black (mg) at time t (min).

The calculated reaction rate by using TGA at 500°C and 80°C were 0.0856 mg/min and 0.4438 mg/min. The ratio of rate at 80°C to rate at 500°C is 5.185. While the normalized reaction rate from ETEM at 500°C and 800°C were 0.12nm/s and 0.62nm/s, respectively, making the ratio become 5.167 (0.62/0.12). As 5.167 is similar to 5.185, the in-situ ETEM experiments are validated by the ex-situ TGA experiment.

2. Catalytic oxidation in 1 Pa O_2 at 500°C with commercial CeO_2 catalyst

A similar ETEM experiment was done with mixture of commercial CeO_2 catalyst and carbon in 1 Pa O_2 at 500°C, as shown in Figure A1. The movement of catalyst can be barely observed, which is different from the scenario with our 10%Fe/CeO_2 catalyst. The contact length between carbon and catalyst ranged from 629-822 nm, and the measured normalized reaction rate is in a range of

0.015-0.03 nm/s with an average of 0.024 nm/s, suggesting a lower reaction rate than the 10%Fe/CeO_2 catalyst at the same reaction conditions. This low oxidation rate could be the reason that catalyst movement is not observed.

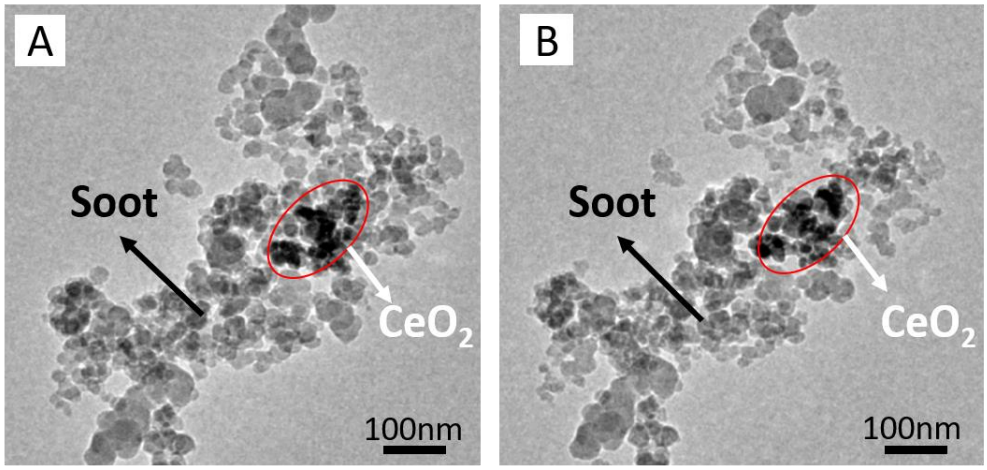

Figure A1. ETEM of carbon and commercial CeO_2 during the reaction at 500°C in 1Pa O_2; A: 0min; B: 24min. The CeO_2 catalyst clusters are circled in red lines.

For image processing, the carbon oxidation rate (r) was estimated by measuring the decrease of the area (A) representing carbon particles at a given time. The methodology to determine the area (A) is described next. As mentioned previously, the contour of the catalyst particles was drawn manually using Photoshop. In an ETEM micrograph, the black particles usually represent the catalyst, but not always, as several carbon particles existing on top of each other and would look dark grey or black. In order to avoid misrepresenting carbon particles as catalyst particles, those dark particles were monitored closely and carefully (if they shrunk or disappeared then it meant that they are carbon particles, otherwise they are considered as catalyst particles. Once all catalyst particles have been identified, they are artificially removed from the ETEM micrograph. The area (A) considered for calculating the reaction rate was the entire surface area left on the ETEM

micrograph (i.e. surface area representing carbon particles). The value of the area, A, was calculated using ImageJ. So, for each time interval, an oxidation rate was obtained. The contact length where carbon and catalyst particles are connected were measured by ImageJ, as well. Because the catalytic reaction occurs at the interface and the reaction rate depends on the contact points between the carbon and catalyst particles, the reaction rates were normalized by being divided by the contact length, in order to obtain normalized reaction rate (r′).

The analysis of the movement of the catalyst and carbon particles was carried out as follows: first the video was divided into several images at different times; at 500°C images were analyzed every minutes, whereas at 800°C images were analyzed every 30 seconds due to faster reaction. Each image was pixelated using ImageJ software who could assign coordinates to all pixels using a common reference origin (red point) as shown in Figure 4.4 (B). For Figure 4.4, the pixel size is 0.83 nm by 0.83 nm. Once the boundary of the particles was determined (manually using Photoshop), the coordinate of its centroid was calculated using ImageJ. The movement velocity can then be calculated based on the distance between two consecutive centroid dividing by the time interval.

3. The normalized reaction rate as a function of time

The appropriateness of the normalized rate calculation as a function of time is shown in Figure A2, showing that the normalized rate remains reasonably constant during the initial period of the reaction. This Figure also helped identifying a few outliers that were removed for subsequent calculations.

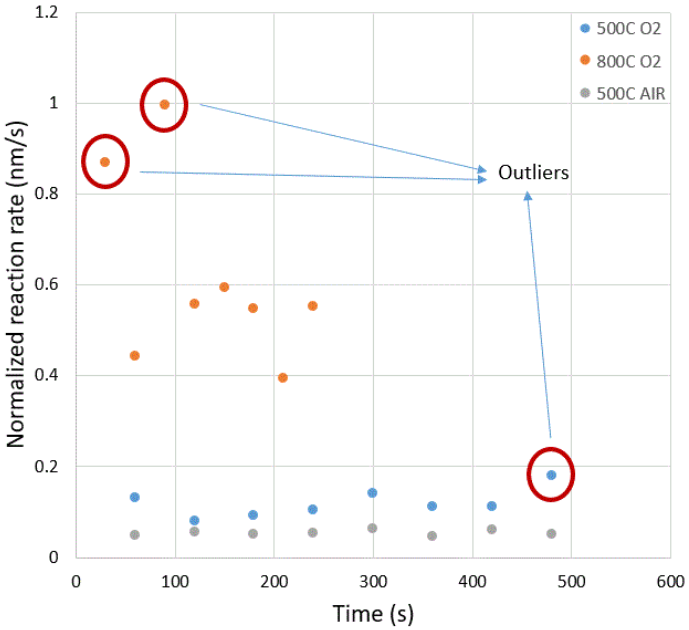

Figure A2. The normalized reaction as a function of time

4. Sensitivity analysis

Due to the sensitive nature of nanoparticles, where conventionally negligible forces can play an enormous role, a sensitivity analysis must be done for such work to establish that the effects observed are not due to the effect of the electron beam or gas flows.

4.1. Beam Effects

Although the electron beam within ETEM would effect the carbon oxidation, but in order to establish that the observed movement is not the result of beam charging, a sample of carbon and catalyst nanoparticle mixture was heated up to 500°C in high vacuum. Images were taken, the beam was turned off, and oxygen injection started. Figure A3(A) was recorded just before turning off the beam. After 40 minutes reaction, the beam was turned on again and image was recorded as shown Figure A3 (C). Since Figure A3 (A) and (C) were not able to clearly show the catalyst

configuration, Figure A3 (B) and (D) - the dark field image corresponding to Figure A3 (A) and (C) respectively, were used to exhibit the movement of catalyst. It can be observed that carbon originally in contact with the catalyst was consumed by the time Figure A3 (C) was taken, and the catalyst circled in red has obviously moved significantly and assembled into a larger aggregate. This demonstrated that the movement of the catalyst is not the result of beam energy, but rather by the reactions between the catalyst and carbon nanoparticles.

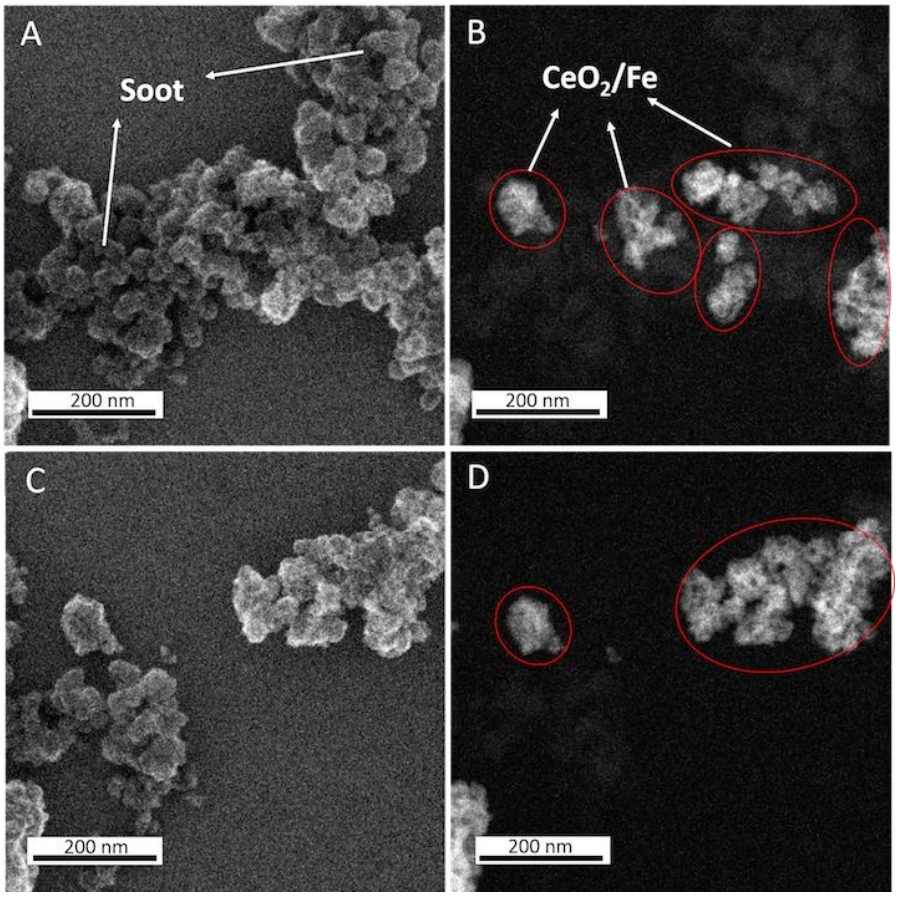

Figure A3. ETEM images for carbon and 10%Fe/CeO_2 catalyst nanoparticles recorded at 500°C in 1 Pa O_2, A and B: Secondary electron image and corresponding dark field image before turning off beam, respectively; C and D: Secondary electron image and corresponding dark field image after 40 min

4.2. Gas Flow and Substrate Effects

As the sample is in a constant cloud of replenishing reactant gas, it is necessary to demonstrate that the mobility of catalyst was not caused by gas flow. Initial calculations and experiments have established that the sample is well clear of the mean free path of the gas, and can be considered to sit in a quiescent atmosphere of gas. These trials were repeated with a catalyst/carbon sample at 500°C and 1 Pa of N_2 flow, as shown in Figure A4. There was no obvious change or movement of catalyst and carbon, which meant that no carbon oxidation or catalyst movement happened in the N_2 atmosphere. It confirmed that the carbon oxidation and movement of catalyst were not caused by gas flow, nor any potential reactions with the substrate.

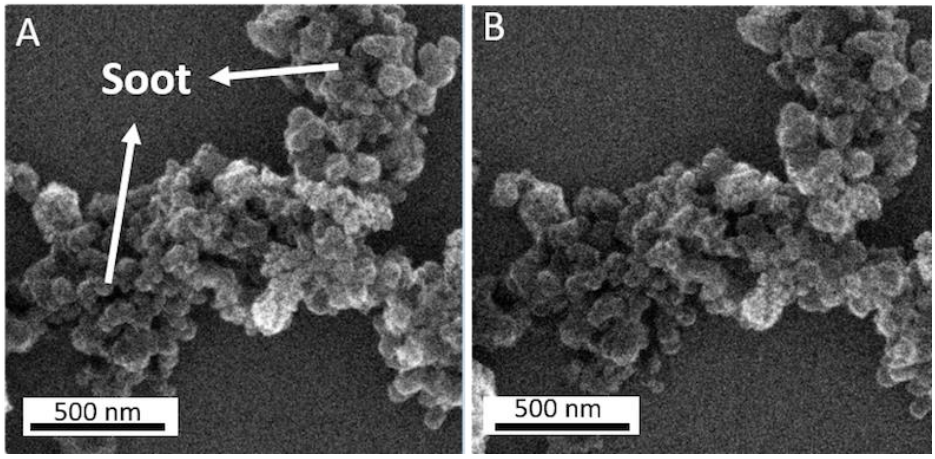

Figure A4. ETEM images for carbon and 10%Fe/CeO_2 catalyst nanoparticles recorded at 500°C in 1 Pa N_2, A: 0 min, B: 60 min

4.3. Secondary Reactions and Movement

In order to further understand catalyst mobility, it was necessary to justify if the movement of the catalyst was caused by the reaction between the particles themselves. To check this influence, tests

were run with a sample of the catalyst and carbon nanoparticles separately at 500℃ in 1 Pa oxygen atmosphere. As shown in Figure A5, for catalyst only, no obvious change of the catalyst was observed after 25 minutes. In Figure A6, non-catalytic carbon oxidation only happened from the outer surface of carbon nanoparticles and no movement was observed during 40 minutes reaction. This shows that only with catalytic carbon oxidation, both carbon and catalyst nanoparticles would show mobility.

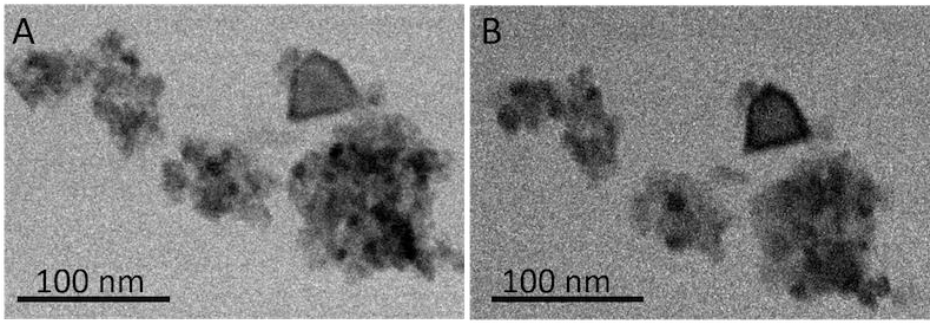

Figure A5. ETEM images for 10%Fe/CeO_2 catalyst only recorded at 500℃ in 1 Pa O_2, A: 0 min, B: 25 min

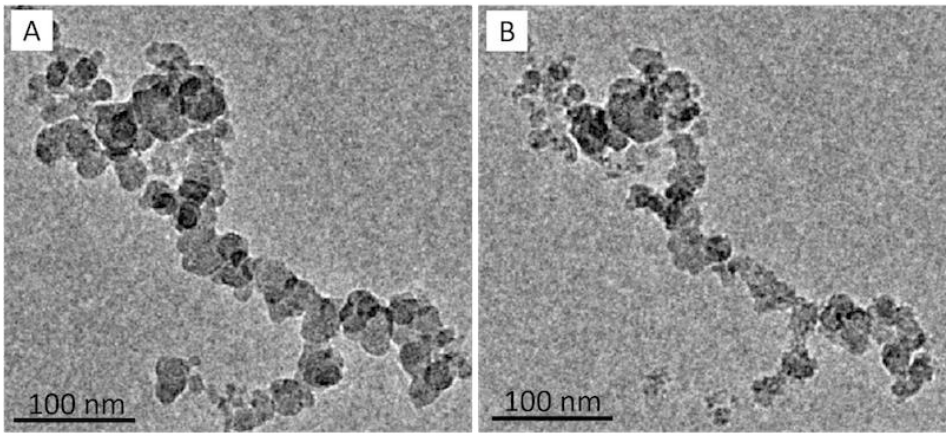

Figure A6. ETEM images for non-catalytic carbon oxidation recorded at 500℃ in 1Pa O_2, A: 0 min, B: 40 min

4.4. In high vacuum

Finally, a study was done to establish the reactivity of the catalyst with no oxygen injection. For the reactions in vacuum, as recorded in Figure A7, the carbon-catalyst mixture was heated up to 500°C and maintained at this temperature for 10 minutes at high vacuum. Without oxygenated atmosphere, extremely slow oxidation of carbon, as well as the movement of carbon and catalyst nanoparticles, could be observed because the catalyst itself can provide oxygen to carbon.

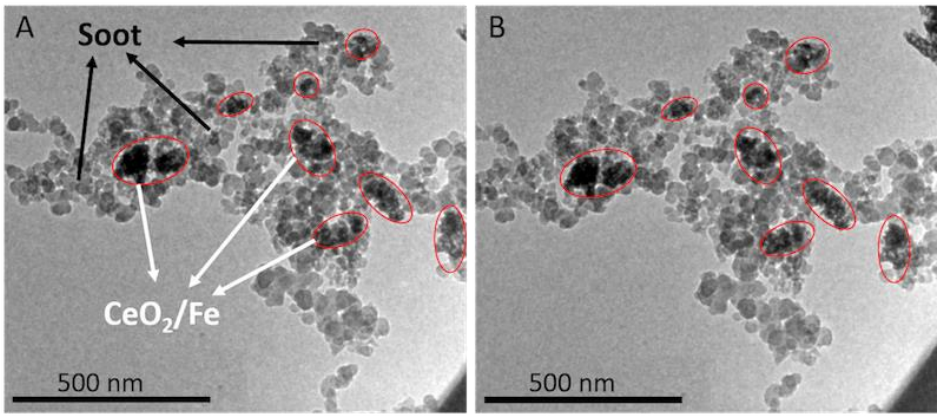

Figure A7: ETEM images for carbon and 10%Fe/CeO_2 catalyst nanoparticle mixture recorded at 500°C in vacuum: A: 0 min, B: 10 min

5. Uncertainty analysis:

1) Distinguishing background and carbon particles are somewhat difficult because they are all in grey color.

2) Distinguishing boundary of catalyst may induce error since the boundary are determined by human eyes.

3) Since 3D image was converted to 2D image, we assume there are only one layer of carbon, but in some area there are possibly not only one layer of carbon.

4) When calculating the reaction rate at the interface, the contact length may change during a time period. But the contact length we used to calculate the reaction rater is the length at the beginning or end of that time period.